Coupled flux qubits and double bifurcation readout

Coupled flux qubits and double bifurcation readout

Proefschrift

ter verkrijging van de graad van doctor
aan de Technische Universiteit Delft,
op gezag van de Rector Magnificus prof. ir. K.C.A.M. Luyben,
voorzitter van het College voor Promoties,
in het openbaar te verdedigen op donderdag 8 juli 2010 om 15:00 uur

door

Pieter Cristiaan de GROOT

natuurkundig ingenieur
geboren te Marken.

Dit proefschrift is goedgekeurd door de promotor:
Prof. dr. ir. J. E. Mooij

Copromotor:
Dr. C. J. P. M. Harmans

Samenstelling van de promotiecommissie:

Rector Magnificus	voorzitter
Prof. dr. ir. J. E. Mooij	Technische Universiteit Delft, promotor
Dr. C. J. P. M. Harmans	Technische Universiteit Delft, copromotor
Y. Nakamura	NEC Green Innovations Research Laboratories, Tsukuba
Prof. dr. G. Wendin	Chalmers Tekniska Högskola, Göteborg
Prof. dr. F. W. J. Hekking	Université Joseph Fourier, Grenoble
Prof. dr. ir. J. W. M. Hilgenkamp	Universiteit Twente, Enschede
Prof. dr. Y. V. Nazarov	Technische Universiteit Delft
Prof. dr. ir. T. M. Klapwijk	Technische Universiteit Delft, reservelid

Published by: Pieter de Groot
Coverdesign: Dirk Smallenbroek
Coverimage: Transition strength modulation of a two-fold degenerate transition
Printed by: Gildeprint Drukkerijen, Enschede

ISBN: 978-90-8593-080-8
Casimir PhD Series, Delft-Leiden 2010-17
Copyright © 2010 by Pieter de Groot
An electronic version of this thesis is available at www.library.tudelft.nl/dissertations

Preface

Physics and mathematics have interested me for as long as I can remember. They provided an abundant supply of fun and challenging puzzles. At some point however, my perception of what it means to study physics changed significantly. I was a master student at the faculty of applied physics in Delft, and was looking for a graduation project. After visiting several potential projects, I came to talk to Alexander ter Haar, a PhD student in the Quantum Transport (QT) group, who had advertised a project on superconducting quantum bits. The project immediately excited me, but I decided to give it one night of thought. I called him first thing in the morning, worried that somebody else would take the project if I waited too long. Alexander laughed wholeheartedly at the naïve enthusiasm, and I started soon after. We were to make a device of two coupled flux qubits, and perform coherent operations on them.

The change came during the following months. Rather than merely solving a series of nice puzzles, we were actually *making* something, something *real*. Of course you know that what's in your quantum mechanics book is supposed to describe reality, but when we did our first experiments, I felt like it all came to life. This aspect made it so much more than just puzzles. We were exploring!

This excitement is also what made me feel at home in QT, as I found out that it is a common property of the people in the group. I truly think that passion is the binding factor that lets so many different people work together as they do. For this I would like to thank Hans Mooij, for being one of the most passionate physicists I know. It was eleven o'clock in the evening when I called you at home (at your request), to tell you that I had just succeeded to perform two consecutive operations on the system of two coupled qubits. You rushed to the university on your bike to see the results, and we discussed for at least an hour. I would also like to thank you for all the freedom I had during my PhD research, both in what to do, and how to do it, even if you didn't fully agree with my approach. This was very scary at first, but now I realise how exceptional this is, and I don't think I could have learned more anywhere else. Kees Harmans, thank you for all your advice, and great discussions on physics and more important parts of life.

I really enjoyed how you could listen, ask a few simple yet sharp questions, and make me realise that I was completely wrong about something. And thank you for caring so much as you did for the wellbeing of all "your" PhD's.

I would like to thank Alexander ter Haar, who introduced me to the world of flux qubits, but also to many bars in The Hague that I would never want my children to visit. You were a great mentor. Thank you Jelle Plantenberg, for always being such a cheerful person in the group. I am very happy that we could collaborate on such a great project, and even more happy that we could collaborate during the group parties, taking turns to stimulate people to take *just* one more. I would also like to thank Adrian Lupaşcu for all the help, the advice and the great discussions we had. My trips to visit you in Paris and Waterloo were extremely fruitful, and I hope we can turn it into a real tradition. Floor Paauw, thank you for always being friendly and thoughtful for everybody around you during your whole PhD. It is a great example to many of us. And thank you for all the fun we had. Thank you Pol Forn Diaz and Thomas Picot for the nice discussions we had about physics and books, and for sharing the burdens of doing a PhD. Also thanks to Ad Verbruggen, Arkady Fedorov, Tomoko Fuse, Jürgen Lisenfeld, Lyosha Feovanov, Shiro Saito, Marco van der Krogt, Jonathan Eroms and Patrice Bertet for the help, discussions and nice atmosphere in the flux qubit team. Jürgen, I hope you enjoyed our collaboration as much as I did. And thanks to Sahel Ashhab for our great discussions about physics and religion and for inviting me to Japan. It was a great time. During my PhD, I supervised two master students, Arjan van Loo and Marcel Manheller, and one bachelor student, Wout Kremers. I have learned a lot from each of you, and I hope this is mutual. Arjan, I enjoyed your enthusiasm a lot.

I thank Raymond Schouten for all his contributions to the experiments, and for learning me about electronics, noise, and the importance of Friday-afternoon projects. My experiments demanded so much new electronics, that I often wondered how you managed to have any time left for the other 50 people in the group. I enjoyed all the interactions we had. None of the experiments would have worked without your contributions. Also many thanks to to people of the Instrumenten Dienst, especially Piet Mulder and Rogier van den Berg, for building all these devices for us.

I would like to thank Bram van der Enden, Remco Roeleveld, Peter and Mascha van Oossanen, Willen den Braver, Wim Schot and Leo Lander for their technical support and continuous supply of helium. Bram, if everybody's "yes" would be as productive as your "no", we would have at least double the scientific output. And thank your for your stories, humor and cheerful whistling in the corridors. Remco, I'm sure we will meet someday on a bike somewhere in France, and if we do, you will have to drink a beer with me. Thank you Yuki Nakagawa, Angèle Fonteijn and Ria van Heeren for the administrative support. In the jungle

of TU paperwork, you are truly lifesavers. Yuki, thanks for treating us to a fantastic Japanese dinner. It will be impossible to repay this in 'dutch-style' dinners, but I'll try. Angèle, you have made it into the hall of fame, by knowing where to park your bike for a typical QT-party.

I have shared an office with Ivo Vink, Laurens Willems van Beveren, Gary Steele, Umberto Perinetti and Maarten van Weert. I am glad that you all enjoyed Snoop as much as I did! Ivo, thanks for all your help and advice. It was great fun sharing an office, and even more fun being neighbours at the Hopstraat. I enjoyed very much the zoo that you and Sietske gathered around you. Gary thanks for always being available for advice, for your enthusiasm, and preparing great diners.

There are many people that make QT a great place to work. For good discussions and fun QT parties, I would like to thank all the QT-members, with a special thanks to "old" members: Floris Zwanenburg, Jorden van Dam and Hubert Heersche, and the "new" members: Katja Nowack, Reinier Heeres, Toeno van der Sar, Gijs de Lange, Maarten van Kouwen, Juriaan van Tilburg, Stevan Nadj-Perge and Gilles Buchs, and of course all the people mentioned earlier. Floris, your bluntness is impressive, even by Delft standards. It makes you a great discussion partner. Katja, you are capable of cheering up a whole group. I am glad that you will also stay a bit longer, so we can have some post-thesis parties. Reinier, thanks for joining me with writing the measurement program QTLab, it was a vital part of all my experiments, and you made it much more fun. For this I would also like to thank Martijn Schaafsma, who built most of the instrument drivers. Toeno and Gijs, I was sad to miss the opportunity to collaborate more closely with both of you, but very happy that you found a new home in the diamond lab. I hope we can enjoy a few more (QT) parties together. During my PhD, two close friends did their master project in QT: Karin Huizinga and Freek Kelkensberg. It was great to be colleagues for a while. Ronald Hanson and Lieven Vandersypen, it was great to be able to discuss with such talented physicists. And thank you Leo Kouwenhoven for making QT the group it is today.

I would also like to thank the Nanofacility team for the great facilities and support, specifically Marco van der Krogt, Arnold van Run, Anja van Langen, Roel Mattern, Patrick Lew, Mark Zuiddam and Emile van der Drift.

I have spent three months on an internship in ETH Zurich in the group of Atac Imamoglu. I would like to thank Atac for this opportunity. I had a great time, and for this I would also like to thank Val Zwiller, Magnus Borgström, Jeroen Elzerman and Christian Latta.

I would like to thank my paranimfen Stijn van Dorp and Dirk Smallenbroek for accompanying me on the defense day. And I would like to thank Sahel Ashhab, Adrian Lupaşcu, Stijn van Dorp, Dirk Smallenbroek, Lars Hörchens, Ivo Vink,

and Pol Forn-Diaz for their help and comments when writing this thesis.

Outside the scientific community I have had much support from my family and friends. I haven't been visiting as much as I would have liked, and am looking forward to changing that soon. I would specifically like to thank my parents for all their love and support. It is great to have such a solid base. And last, but not least, I would like to thank Margreet for her continuous love, support, and kind patience throughout the past years. You are the best thing that ever happened to me, and I am looking forward to our future together.

Pieter de Groot
Delft, July 2010

Contents

1 Introduction **1**
- 1.1 Quantum mechanics . . . 1
- 1.2 Quantum computation . . . 2
- 1.3 Josephson circuits . . . 3
- 1.4 Thesis overview . . . 6
- 1.5 Acknowledgements . . . 6
- Bibliography . . . 7

2 The flux qubit **9**
- 2.1 Theoretical description of the flux qubit . . . 10
  - 2.1.1 Full quantum-mechanical model . . . 10
  - 2.1.2 Simplified two-level model . . . 14
  - 2.1.3 Large loops and additional junctions . . . 16
- 2.2 Operation . . . 18
  - 2.2.1 Larmor precession . . . 19
  - 2.2.2 Rabi oscillations . . . 19
  - 2.2.3 AC Stark effect . . . 20
- 2.3 Decoherence . . . 21
  - 2.3.1 General Framework for quantifying decoherence rates . . . 21
  - 2.3.2 Johnson-Nyquist noise in the electrical circuits . . . 23
  - 2.3.3 Microscopic noise sources . . . 24
- 2.4 Qubit state detection with a DC-SQUID . . . 25
- Bibliography . . . 29

3 Coupled flux qubits **31**
- 3.1 Coupling mechanisms . . . 32
- 3.2 Energy spectrum of two coupled flux qubits . . . 35
  - 3.2.1 Theoretical model . . . 35
  - 3.2.2 Spectroscopy measurements . . . 37

3.3 Requirements for performing a quantum-algorithm . . . 40
3.3.1 Single- and two-qubit gates based on resonant driving: a universal set . . . 40
3.3.2 Phase requirements when employing multiple driving frequencies . . . 43
3.3.3 Hardware for phase and timing control . . . 45
Bibliography . . . 50

4 Controlled-NOT gates on coupled flux qubits 51
4.1 Introduction . . . 52
4.2 Experimental Setup . . . 52
4.3 Controlled-NOT gate by resonant driving . . . 54
4.4 Conditional spectroscopy for detector visibility calibration . . . 60
4.5 Quantum phase induced by the CNOT gate . . . 63
4.6 Conclusions . . . 63
Bibliography . . . 64

5 Selective darkening of degenerate transitions 67
5.1 Introduction . . . 68
5.2 Method . . . 68
5.3 Conditions for darkened transition . . . 71
5.4 Experimental Setup . . . 73
5.5 Experiment 1: Double Rabi-frequency for driving a degenerate transition . . . 74
5.6 Extracting level occupations from detector switching-probabilities . . . 74
5.7 Experiment 2: Transition strength tuning . . . 77
5.8 Experiment 3: Darkened transitions . . . 79
5.9 Conclusions . . . 79
Bibliography . . . 80

6 Decoherence in a two-qubit system 83
6.1 Location of a noise source . . . 84
6.1.1 Relaxation . . . 85
6.1.2 Dephasing . . . 89
6.2 Relaxation to an intermediate state . . . 90
Bibliography . . . 98

7 Qubit state detection with an AC-driven SQUID **99**
7.1 Non-linear dynamics of an AC-driven SQUID . . . 100
7.2 Qubit state detection scheme . . . 103
7.3 Experimental Setup . . . 105
7.3.1 Single Detector . . . 105
7.3.2 Two Detectors . . . 109
Bibliography . . . 112

8 Low-crosstalk bifurcation detectors for coupled flux qubits **113**
8.1 Introduction . . . 114
8.2 Experimental Setup . . . 114
8.3 Experiment 1: The effect of an oscillating field on the detectors . . . 116
8.4 Experiment 2: Phase-independent crosstalk . . . 118
8.5 Experiment 3: Phase-dependent crosstalk . . . 118
8.6 Conclusions . . . 120
Bibliography . . . 121

9 Discussion of current status and future directions **123**
9.1 Current status . . . 123
9.2 Discussion and suggestions for improvement . . . 125
9.2.1 Coupling and operation . . . 125
9.2.2 Decoherence . . . 127
9.2.3 Readout . . . 129
9.3 Future directions . . . 130
9.4 Conclusion . . . 131
Bibliography . . . 132

Summary **133**

Samenvatting **135**

Curriculum Vitae **137**

List of Publications **139**

Chapter 1

Introduction

1.1 Quantum mechanics

Quantum mechanics is a set of principles that describes the behaviour of the microscopic world. For example, the behaviour of atoms, electrons, photons and similar microscopic entities. Ever since it emerged, approximately 100 years ago, quantum mechanics has been remarkably successful in describing a wide range of phenomena, and has led to applications that are now indispensable in our daily lives. Nevertheless, many fundamental aspects of quantum mechanics are still considered counter-intuitive by most physicists. This is nicely illustrated by the reluctance of some physicists that pioneered this field of physics. In what he later called "an act of desperation", Max Planck proposed in 1900 the quantisation of energy to explain the observed spectrum of thermal radiation that is emitted from the surface of an object [1]. This step is now considered as the birth of quantum mechanics. In 1935, Albert Einstein, Boris Podolsky and Nathan Rosen introduced a "gedanken Experiment", that was designed to prove that quantum mechanics could never be a complete theory [2]. They argued that a measurement of one part of a system cannot have a non-local effect on a distant part of that system. In quantum mechanics this is possible and referred to as entanglement. Einstein called it "spooky action at a distance". This thought experiment has been performed in a real experiment, and, ironically, has become one of the most convincing demonstrations of the validity of quantum mechanics.

In view of the work presented in this thesis, we summarise the basic characteristics of quantum mechanics as follows.
(i) In classical mechanics, the state of a physical system, for example a particle in a potential, is defined by its precise position and velocity coordinates. In quantum mechanics the same particle can be spread over these coordinates. This spread

means that, in a sense, the particle can exist in multiple locations simultaneously. This spread is represented by a complex distribution function, or *wavefunction*, $\Psi(x,t)$.
(ii) If the state of the system is measured by an ideal measurement instrument, the system is forced into one particular state that corresponds to the measurement outcome. The wavefunction is said to "collapse" into a single spiked distribution function. The outcome of the measurement is determined by an apparently non-deterministic process; the outcome of a single measurement is random, only the probability of each measurement outcome can be determined. The probability distribution of the possible measurement results is determined by $|\Psi|^2$. Because the first measurement changed the wavefuntion to a single sharp-spiked distribution, a second measurement of the system will have unity probability of finding the same state as the first measurement.
(iii) The evolution of the system is determined by a first-order differential equation for the wavefunction Ψ - the Schrödinger equation. The wavefunction exhibits typical wavelike phenomena, such as interference and standing wave-like behaviour. The latter is manifest when the system contains a confining potential, and limits the "permitted" states of the system to a discrete set of energy states.

These remarkable properties are the basis for a promising application that gave direction to most of the work presented in this thesis: the quantum computer.

1.2 Quantum computation

As it turns out, it is problematic to efficiently calculate the properties of a quantum system with a computer that is based on classical physics. This issue was noted in 1982 by Richard Feynman, and he suggested that possibly a computer based on quantum mechanics would be better suited to simulate quantum systems [3]. A few years later, David Deutsch investigated a similar question: are there computational problems that can be solved more efficiently using quantum mechanics than with a classical computer, the latter represented by the "Turing machine" [4]. In 1994 Peter Shor discovered the now famous quantum algorithm for factorizing a number into its primes [5]. This algorithm proved exponentially faster than any classical algorithm, strengthening the idea that indeed a quantum computer is more powerful than a classical computer.

To obtain an intuitive picture of the enhanced computing power of a quantum computer, consider the following (simplified) comparison. In a normal (binary) computer, the information is represented by *bits*, which are physical systems that each can be in one of two states. These states are labeled 0 and 1. A register of N bits can hold 2^N different values. In a calculation, the value from such a register serves as the input value and the calculation consists of performing the

appropriate operations on the bits of the register. If the output is required for multiple input values, the full calculation has to be repeated from the start.

In a quantum computer these bits are replaced by quantum mechanical two-level systems, referred to as quantum bits, or *qubits*. A qubit cannot only be in its ground state $|0\rangle$ or excited state $|1\rangle$, but in any superposition of these two states. In a sense, a register of N qubits can contain *all* 2^N values simultaneously. A calculation on such a register contains a certain parallelism, which, together with the wave-like properties of a quantum-mechanical system, can result in operations that are not possible with a classical system. Note, however, that the aspect of parallelism is mostly lost the moment the register is read out, as the measurement projects the register in one of the possible outcomes, eliminating all the other values in the register. Nevertheless, quantum algorithms such as the Shor algorithm have been discovered that benefit from the quantum-mechanical operations.

A large number of implementations for a quantum computer have been proposed. The range of physical systems is very diverse, including cavity-quantum electrodynamics systems [6], ion traps [7], nuclear spins [8], electron spins or charge in quantum dots, [9, 10], lattice defects in diamond [11] and systems based on Josephson junction circuits [12]. Until now, the most advanced demonstration of quantum computation was an implementation of the Shor algorithm in a system with 7 nuclear spin qubits [8].

1.3 Josephson circuits

The qubit implementations that are used and studied in this thesis are electrical circuits containing Josephson junctions. In 1962 Brian Josephson predicted new effects characterising tunneling between two weakly coupled superconductors [13]. He stated that the tunneling of charge carriers from one superconductor to the other is a phase coherent process, and that this tunneling can give a net supercurrent through the barrier. If φ is the difference between the superconducting phase values on both sides of the barrier, the voltage V across the junction and the supercurrent I_s are related through the equations:

$$V = \frac{\Phi_0}{2\pi}\frac{\partial\varphi}{\partial t}, \tag{1.1}$$

and

$$I_s = I_c \sin\varphi, \tag{1.2}$$

where I_c is the critical current of the junctions, describing the strength of the coupling between the two superconductors, and $\Phi_0 = h/(2e)$ is the flux quantum.

As a circuit element, a Josephson junction is a unique element to engineer quantum circuits with useful energy levels, as it is non-dissipative and highly non-linear. To describe realistic implementations, the ideal Josephson junction has to be shunted by an electrical capacitance, inherently formed by the isolating barrier, and a resistor, describing the losses due to dissipative behaviour. This model, called the Resistively Capacitively Shunted Junction (RCSJ) model, accurately describes the dynamics of realistic junctions. The shunts can be tailored to accommodate many different applications. For quantum circuits, the junctions are made to have near infinite resistance, meaning that they are highly underdamped. In this case the junction is accurately described by an ideal junction shunted only with a capacitor. The relevant energy scales of the junction are the charging energy $E_C = (2e)^2/(2C)$ of the capacitor, with $2e$ the charge of the charge carriers in a superconductor, and the Josephson energy $E_J = \Phi_0 I_C/(2\pi)$, the energy associated with the coupling between the superconductors. A variety of quantum circuits have been realised, ranging from dominated by the charging energy E_C to dominated by the Josephson energy E_J [14]. In this thesis we focus on the superconducting flux qubit [15], which is in the regime $E_J >> E_C$.

To fabricate Josephson junction devices we use the well-established shadow-evaporation technique [16]. A flux qubit device generally consists of multiple thin-film metal layers, each with a specific pattern. Every thin film metal layer is fabricated using a lift-off bi-layer resist scheme. The wafer or chip surface is coated with two different resists as depicted in Fig. 1.1(a), of which the bottom layer is more sensitive to electrons.

The desired patterns are written into the resist using electron-beam lithography, altering the chemical composition of the resist. This allows the exposed areas to be selectively removed using a wet developer, see Fig. 1.1(b). Now either a single metal layer, or the junction sandwich structure is evaporated onto the chip surface, as shown in Fig. 1.1(c) and Fig. 1.1(d). Finally the excess metal is removed with the unexposed resist in the lift-off step, using a chemical solvent, leaving only the desired pattern, see Fig. 1.1(e).

The devices used in this thesis consist of several thin film metal layers. The first layer is made of AuPd, and contains contact pads, on-chip resistors and electron-beam alignment markers. The pads are used to connect the microchip to the electrical leads of the measurement setup, the resistors are used in filtering structures, and the alignment markers allow for an exact overlay of the following electron-beam patterns. The second layer is a shadow-evaporated Al/AlOx/Al tri-layer, out of which the qubit junctions are formed. Also, the bottom plates of the on-chip capacitors are formed with this layer. An electrical isolation is added towards the next layer by growing an AlOx dielectric layer using an oxygen plasma. Finally, the SQUID detector is fabricated by using a second Al/AlOx/Al tri-layer. This last layer also contains the on-chip wiring, the capacitor top plates

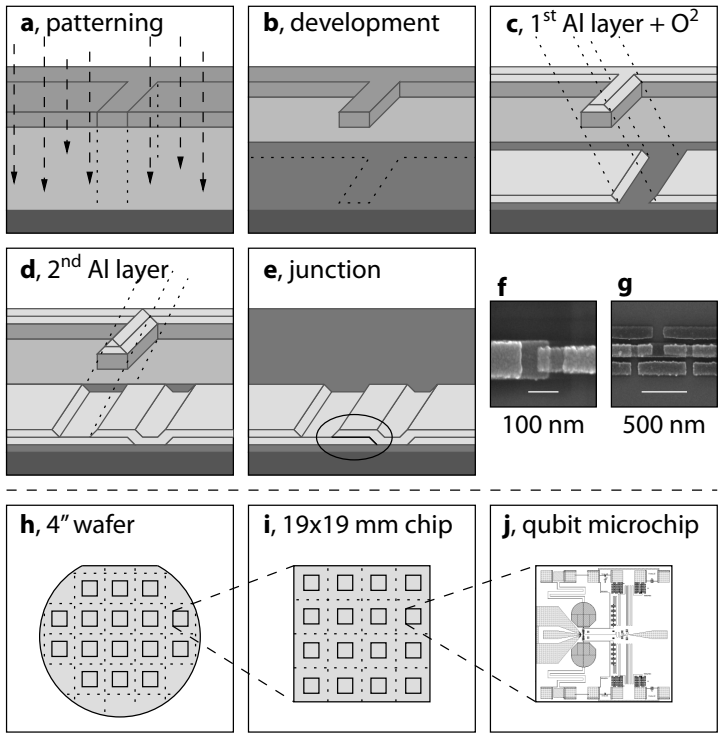

Figure 1.1: Fabrication of flux qubit devices. (a) Patterning using electron-beam lithography. (b) Development of the bi-layer resist. (c) Evaporation of first aluminum layer, followed by oxidation in pure oxygen. (d) Evaporation of second aluminum layer. (e) Lift-off of the resist, leaving the Josephson junction. (f) Scanning electron micrograph of a parallel junction. (g) Scanning electron micrograph of a perpendicular junction. (h) A 4" wafer is diced into 19x19 mm substrates. The first non-critical layers, such as the AuPd layer containing the resistive elements, are typically fabricated on the full wafer. (i) The qubit and SQUID layer are both fabricated on 19x19 mm chips, according to the process of a-e, and contain 16 separate microchips of possibly various pattern variations. (j) A single 3.4x3.4 mm qubit microchip.

and the on-chip inductors used for filtering. In the final step, the 19x19 mm substrates are diced into 16 separate microchips of 3.4x3.4 mm, each containing a single quantum bit circuit.

1.4 Thesis overview

In Chapter 2 we provide an introduction to the flux qubit, including the control of its quantum state, mechanisms that result in loss of quantum information, and a method to read out the state of the qubit. Chapter 3 contains a detailed analysis of a system of two coupled qubits. The excitation spectrum is studied both analytically and experimentally, and the requirements for coherent control of the quantum state of a coupled system are discussed. In Chapters 4 and 5 experiments are presented that demonstrate two different entangling two-qubit gates. In the first case a spectroscopic splitting is employed to individually address the separate transitions of the two-qubit system. Chapter 5 introduces a new method for creating entanglement: the selective darkening of degenerate transitions by local control of the amplitude and phase of the driving field. In a coupled-qubit system, the decoherence of the combined states involves some aspects that do not exist in a single-qubit system. These aspects are discussed in Chapter 6. In the following Chapters 7 and 8 we study the bifurcation readout method. This readout method is first explained in Chapter 7, and an expansion to a double detector-setup is presented. In Chapter 8 the crosstalk between two bifurcation detectors is studied experimentally. Finally, in Chapter 9, we discuss the current status and future directions of superconducting qubit research.

1.5 Acknowledgements

The experiments presented in Chapter 3 and 4 have been performed together with Alexander ter Haar and Jelle Plantenberg, respectively, and the experiments in Chapter 5 and 8 have been performed together with Jürgen Lisenfeld and Arjan van Loo. I thank Adrian Lupaşcu for his contributions and input, specifically regarding the bifurcation readout method, Sahel Ashhab for his contribution to the analysis of the selective darkening method, and Lieven Vandersypen for his contribution to the phase analysis of two-qubit gates. I thank Raymond Schouten, who designed all the home-built electronics, and the Electronics Service Department for building the numerous electronic sources and components. All the devices were fabricated in the Nanofacility of the TU Delft, and I would like to thank the Nanofacility-team for fabrication support, and Bram van der Enden, Remco Roeleveld, Peter van Oossanen, Willem den Braver, Wim Schot and Leo Lander for technical support.

Bibliography

[1] M. Planck, Zur Theorie des Gesetzes der Energieverteilung im Normalspektrum, Verhandl. Deutsch. Phys. Ges. **2**, 237 (1900).

[2] A. Einstein, B. Podolsky, and N. Rosen, Can Quantum-Mechanical Description of Physical Reality Be Considered Complete?, Phys. Rev. **47**, 777 (1935).

[3] R. P. Feynman, Simulating Physics with Computers, Int. J. Theor. Phys. **21**, 467 (1982).

[4] D. Deutsch, Quantum Theory, the Church-Turing Principle and the Universal Quantum Computer, Proceedings of the Royal Society of London. A. Mathematical and Physical Sciences **400**(1818), 97–117 (1985).

[5] P. W. Shor, Algorithms for Quantum Computation: Discrete Logarithms and Factoring, in *Proceedings, 35th Annual Symposium on Foundations of Computer Science*, IEEE Press, 1994.

[6] J. M. Raimond, M. Brune, and S. Haroche, Manipulating quantum entanglement with atoms and photons in a cavity, Rev. Mod. Phys. **73**(3), 565–582 (2001).

[7] D. Leibfried, R. Blatt, C. Monroe, and D. Wineland, Quantum dynamics of single trapped ions, Rev. Mod. Phys. **75**(1), 281–324 (2003).

[8] L. M. K. Vandersypen, M. Steffen, G. Breyta, C. S. Yannoni, M. H. Sherwood, and I. L. Chuang, Experimental Realization of Shor's Quantum Factoring Algorithm using Nuclear Magnetic Resonance, Nature **414**, 883 (2001).

[9] D. Loss and D. P. DiVincenzo, Quantum computation with quantum dots, Phys. Rev. A **57**(1), 120–126 (1998).

[10] D. P. DiVincenzo, D. Bacon, J. Kempe, G. Burkard, and K. B. Whaley, Universal quantum computation with the exchange interaction, Nature **408**, 339–342 (2000).

[11] F. Jelezko, T. Gaebel, I. Popa, A. Gruber, and J. Wrachtrup, Observation of Coherent Oscillations in a Single Electron Spin, Phys. Rev. Lett. **92**(7), 076401 (2004).

[12] M. H. Devoret, A. Wallraff, and J. M. Martinis, Superconducting Qubits: A Short Review, arXiv:cond-mat/0411174 .

[13] B. D. Josephson, Possible new effects in superconductive tunnelling, Physics Letters **1**(7), 251 – 253 (1962).

[14] G. Wendin and V. S. Shumeiko, *Superconducting Quantum Circuits, Qubits, and Computing*, Handbook of Theoretical and Computational Nanotechnology, Ed. M. Rieth and W. Schommers.

[15] J. E. Mooij, T. P. Orlando, L. Levitov, L. Tian, C. H. van der Wal, and S. Lloyd, Josephson Persistent-Current Qubit, Science **285**, 1036–1039 (1999).

[16] G. J. Dolan, Offset masks for lift-off photoprocessing, Appl. Phys. Lett. **31**, 337 (1977).

Chapter 2

The flux qubit

The Josephson persistent-current qubit, better known as the flux qubit, consists of a micrometer-sized superconducting loop with three or more Josephson tunnel junctions [1]. For the proper conditions this electrical circuit behaves as a quantum mechanical two-level system, with states composed of clockwise and counter-clockwise persistent currents in the loop. In Section 2.1 we provide the model that describes the dynamics of this system for an arbitrary number of states. From this model we derive a simplified two-level model for the two lowest energy states, which is equivalent to a spin-$\frac{1}{2}$ particle in a magnetic field. The state of this quantum system can be manipulated in different ways. Section 2.2 discusses the basic operations for state manipulation, their physical implementations, and translates them to evolution operators. Uncontrolled parameters in the environment can also induce state changes of a qubit, a phenomenon which is referred to as decoherence. The theoretical framework for decoherence is given in Section 2.3. In Section 2.4 we describe how a DC-SQUID can be used as magneto-meter to detect the magnetic fields that are produced by the persistent currents in the loop.

2.1 Theoretical description of the flux qubit

The flux qubit consists of a superconducting loop with at least three Josephson junctions. Figure 2.1 shows a schematic drawing of a qubit circuit with three junctions with critical currents $I_{c,i}$ ($i = \{1, 2, 3\}$). The intrinsic junction capacitances C_i are drawn explicitly, as they play an important role in the dynamics of the system. The junctions divide the loop into three superconducting islands. The parameter φ_i describes the superconducting phase difference between two islands at the interface formed by junction i.

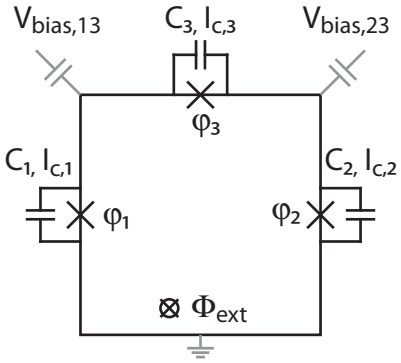

Figure 2.1: Schematic drawing of a flux qubit. The qubit consists of a superconducting loop with three Josephson tunnel junctions. The junctions are characterised by their critical current $I_{c,i}$ and intrinsic capacitance C_i. The externally applied magnetic flux Φ_{ext} and voltage bias $V_{\text{bias,nm}}$ can be used as external control parameters.

2.1.1 Full quantum-mechanical model

The total energy of the circuit comprises the capacitive energy and the Josephson energy of the junctions. The capacitive energy $\frac{1}{2}C_iV_i^2$, with V_i being the potential difference across the capacitors, is transformed using the second Josephson relation (Equation 1.1), yielding the kinetic energy terms

$$T(\vec{\dot{\varphi}}) = \sum_{i=1}^{3} \frac{1}{2} C_i \left(\frac{\Phi_0}{2\pi}\right)^2 \dot{\varphi}_i^2 = \sum_{i=1}^{3} \frac{e^2}{E_{C,i}} \left(\frac{\Phi_0}{2\pi}\right)^2 \dot{\varphi}_i^2, \tag{2.1}$$

where $E_{C,i} = (2e)^2/(2C_i)$ is the charging energy associated with the displacement of a single charge carrier, which is $2e$ for superconductors. The Josephson energy

is the potential energy stored in the phase difference over the junctions

$$U(\vec{\varphi}) = \sum_{i=1}^{3} E_{J,i}[1 - \cos(\varphi_i)], \tag{2.2}$$

where $E_{J,i} = \Phi_0 I_{c,i}/(2\pi)$. These energy terms yield the Lagrangian

$$L(\vec{\varphi}, \dot{\vec{\varphi}}) = \sum_{i=1}^{3} \frac{e^2}{E_{C,i}} \left(\frac{\Phi_0}{2\pi}\right)^2 \dot{\varphi}_i^2 - \sum_{i=1}^{3} E_{J,i}[1 - \cos(\varphi_i)]. \tag{2.3}$$

Flux qubits are typically characterised by $E_{C,i} \ll E_{J,i}$.

The superconducting loop imposes quantisation of the phase around the loop

$$\sum_{i=1}^{3} \varphi_i + 2\pi \frac{\Phi_{\text{ext}}}{\Phi_0} = 2\pi n, \tag{2.4}$$

where n is the integer number of full phase-cycles, and Φ_{ext} is an externally applied magnetic flux, which provides a controllable phase bias in the loop. Because of the phase quantisation, the variables φ_i are not independent. One of the phase terms can be eliminated, leaving only two degrees of freedom. For simplicity, we now limit ourselves to the typical situation that two junctions ($i = \{1, 2\}$) are equal in size, and the area of the third ($i = 3$) is smaller with a scaling factor of α. If we eliminate the third phase φ_3 by the phase quantisation, the Lagrangian reads

$$\begin{aligned} L(\vec{\varphi}, \dot{\vec{\varphi}}) = \quad & \frac{e^2}{E_C} \left(\frac{\Phi_0}{2\pi}\right)^2 \left[\dot{\varphi}_1^2 + \dot{\varphi}_2^2 + \alpha(-\dot{\varphi}_1 - \dot{\varphi}_2)^2\right] + \\ & E_J \left[\cos(\varphi_1) + \cos(\varphi_2) + \alpha \cos(-\varphi_1 - \varphi_2 - 2\pi \frac{\Phi_{\text{ext}}}{\Phi_0})\right], \end{aligned} \tag{2.5}$$

where we dropped the constant energy term $-E_J(2 + \alpha)$.

Before we proceed with the rigorous derivation of the system properties, it is insightful to consider the (classical) potential U. Figure 2.2 shows the potential landscape versus the two degrees of freedom φ_1 and φ_2 for typical qubit parameters. The potential has two minima, located at $\varphi_1 = \varphi_2 = \pm\varphi_{\min} = \pm \arccos(1/(2\alpha))$. The depth of the minima depends on Φ_{ext}. From these considerations we anticipate that the full calculations will present two stable states with persistent currents given by the phase-minima: $I_p \approx \pm I_c \sin(\varphi_{\min})$.

From the Lagrangian we derive the canonical variables

$$q_1 = \frac{\partial L}{\partial \dot{\varphi}_1} = C \left(\frac{\Phi_0}{2\pi}\right)^2 [\dot{\varphi}_1 + \alpha(-\dot{\varphi}_1 - \dot{\varphi}_2)] \tag{2.6a}$$

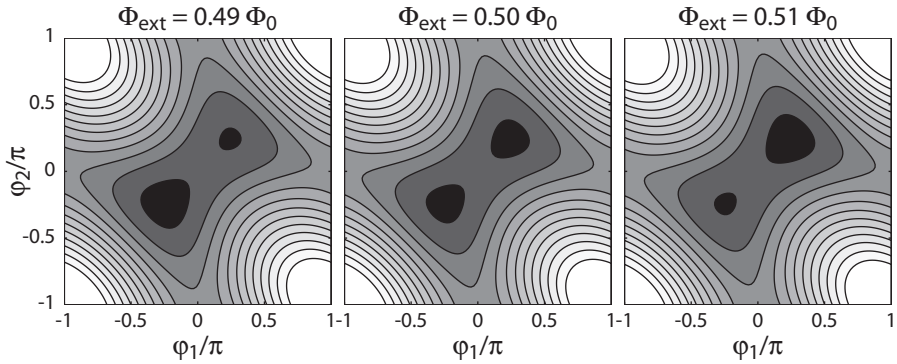

Figure 2.2: Potential energy of a 3-junction qubit as a function of phases φ_1 and φ_2, and for three externally applied magnetic fields Φ_{ext}. For magnetic fields close to Φ_{ext} and relative sizes of $\alpha = 0.5 - 1.0$, the system has a double well potential. The calculations were performed using $E_J = h \times 350$ GHz, $E_C = h \times 20$ GHz, and $\alpha = 0.70$.

$$q_2 = \frac{\partial L}{\partial \dot{\varphi}_2} = C \left(\frac{\Phi_0}{2\pi}\right)^2 \left[\dot{\varphi}_2 + \alpha(-\dot{\varphi}_1 - \dot{\varphi}_2)\right], \tag{2.6b}$$

which yields

$$\dot{\varphi}_1 = \frac{1}{C\left(\frac{\Phi_0}{2\pi}\right)^2} \left(\frac{(1+\alpha)q_1 - \alpha q_2}{1+2\alpha}\right) \tag{2.7a}$$

$$\dot{\varphi}_2 = \frac{1}{C\left(\frac{\Phi_0}{2\pi}\right)^2} \left(\frac{\alpha q_1 - (1+\alpha)q_2}{1+2\alpha}\right). \tag{2.7b}$$

With a Legendre transformation we get the Hamiltonian

$$\begin{aligned} H(\vec{\varphi}, \vec{q}) &= \sum \dot{\varphi}_i q_i - L \\ &= \frac{E_C}{\left(2e\frac{\Phi_0}{2\pi}\right)^2} \left[\frac{1+\alpha}{1+2\alpha} q_1^2 - \frac{2\alpha}{1+2\alpha} q_1 q_2 + \frac{1+\alpha}{1+2\alpha} q_2^2\right] - \\ &\quad E_J \left[\cos(\varphi_1) + \cos(\varphi_2) + \alpha \cos(-\varphi_1 - \varphi_2 - 2\pi \frac{\Phi_{\text{ext}}}{\Phi_0})\right]. \end{aligned} \tag{2.8}$$

Up to this point, the description is fully classical. To find the quantum mechanical eigenvalues and wavefunctions, we can either transform the system using the charge basis ($\varphi \to -i\hbar \frac{\partial}{\partial q}$), or the phase basis ($q \to -i\hbar \frac{\partial}{\partial \varphi}$), and both should yield the same result. Although for flux qubits the phase seems the most natural parameter, since $E_J/E_C > 1$, the charge basis proves to be more efficient. This

is because the cosine terms couple only nearest integer charge states [2], which can be understood considering $\cos(\varphi) = (e^{i\varphi} + e^{-i\varphi})/2$ and

$$e^{\pm i\varphi_i}|n_i\rangle = |n_i \pm 1\rangle \tag{2.9a}$$

$$e^{i(\varphi_i \pm k)} = e^{\pm ik}|n_i + 1\rangle. \tag{2.9b}$$

The integer charge states n_i are given by

$$q_1 = \hbar n_1 \tag{2.10a}$$

$$q_2 = \hbar n_2, \tag{2.10b}$$

and k represents an additional phase offset, such as the term $2\pi\Phi_{\text{ext}}/\Phi_0$ in Eq. 2.8.

We write the Hamiltonian in terms of integer charge states n_1, n_2

$$\begin{aligned} H(\vec{\varphi}, \vec{n}) \quad = \quad & E_C \left[\frac{1+\alpha}{1+2\alpha} n_1^2 - \frac{2\alpha}{1+2\alpha} n_1 n_2 + \frac{1+\alpha}{1+2\alpha} n_2^2 \right] - \\ & E_J \left[\cos(\varphi_1) + \cos(\varphi_2) + \alpha \cos(-\varphi_1 - \varphi_2 - 2\pi \frac{\Phi_{\text{ext}}}{\Phi_0}) \right]. \end{aligned} \tag{2.11}$$

The charge basis consists of states of increasing charge differences across the junctions $|n_1, n_2\rangle$, with $n_1, n_2 = \{0, \pm 1, \pm 2, \ldots, \pm n_{\max}\}$. The Hamiltonian can be solved numerically for an arbitrary number of states, and the accuracy of the lower states increases for larger values of $n_{\max}$.

Figure 2.3(a) shows the lowest three calculated energy levels of a flux qubit as a function of the applied flux Φ_{ext} for the typical junction parameters $E_J = h \times 350$ GHz, $E_J/E_C = 17.5$, and $\alpha = 0.70$. The most important region is around $\Phi_{\text{ext}} = 0.5\Phi_0$. In this region the lowest two energy states are well separated from the other states, which allows the system to be regarded as a two-level system. At $\Phi_{\text{ext}} = 0.5\Phi_0$ the minimum level separation is denoted by Δ, the spectrum gap.

The states of the flux qubit also depend on the applied charge bias $n_{g,ij}$. Figure 2.3(b) shows the energy dependence of the lowest two energy levels on the charge bias $n_{g,12}$ for a magnetic frustration of $\Phi_{\text{ext}} = 0.5\Phi_0$. The modulation of the energy has an amplitude of approximately $h \times 1$ MHz, which shows that the flux qubit is relatively insensitive to charge noise. Note however that the sensitivity depends on the qubit parameters, and for smaller E_J/E_C ratio, the charge sensitivity increases. Although flux qubits are rarely implemented with dedicated charge-bias gates, the charge-dependence is relevant from a decoherence point of view, as stray capacitance to sources of charge noise in the environment is unavoidable (see Section 2.3). Also, the charge dependence is potentially interesting for implementing individual control channels for a system of multiple qubits; charge is much easier to apply locally than the currently used magnetic fields (see Section 2.2).

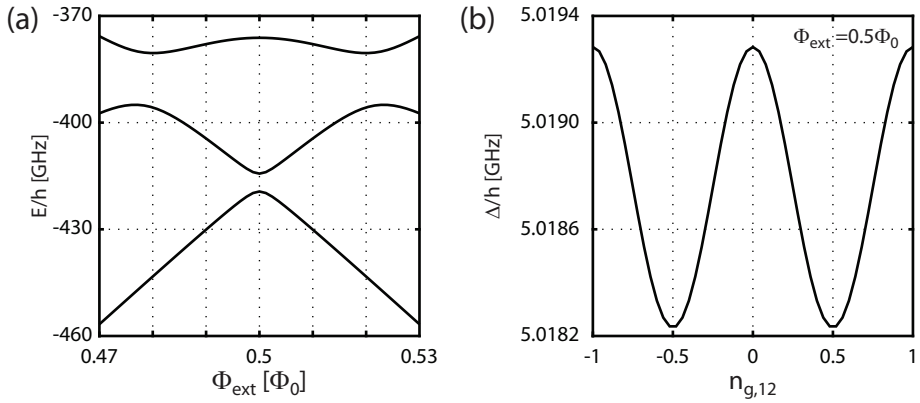

Figure 2.3: Calculated eigenenergies of the flux qubit circuit versus the applied magnetic flux Φ_{ext} (a) and gate voltage $n_{g,12}$ (b). Close to Φ_{ext}, the two lowest levels are well separated from the higher levels, forming an effective two-level system. This two-level system can be used as a logical qubit. The charge dependence of the anti-crossing Δ at $\Phi_{\text{ext}} = 0.5\Phi_0$ is shown in (b), showing that the flux qubit is only weakly sensitive to external charge offsets. The calculations were performed using $E_J = h \times 350$ GHz, $E_C = h \times 20$ GHz, and $\alpha = 0.70$.

2.1.2 Simplified two-level model

The description in the previous section is based on the full quantum mechanical calculations. In the flux bias region around $\Phi_{\text{ext}} = 0.5\Phi_0$ the energy splitting between the ground and the first excited state is much smaller than the splitting between the first excited state and the higher states. In this region the system can effectively be described as a spin-$\frac{1}{2}$ particle in a magnetic field. The Hamiltonian of this simplified two-level system is

$$H = -\frac{\varepsilon}{2}\hat{\sigma}_z - \frac{\Delta}{2}\hat{\sigma}_x, \tag{2.12}$$

where $\varepsilon = -2I_p\left(\Phi_{\text{ext}} - \frac{1}{2}\Phi_0\right)$, Δ is the energy gap at the avoided crossing, and $\hat{\sigma}_i$ are the Pauli-spin matrices. This subspace forms our logical qubit. Figure 2.4(a) shows the energy levels for the full quantum-mechanical calculations (circles), and the simplified two level description (solid lines).

The eigenenergies of this system are $E_{0,1} = \mp\frac{1}{2}\sqrt{\varepsilon^2 + \Delta^2} = \mp\frac{1}{2}\nu$, and the eigenvectors are

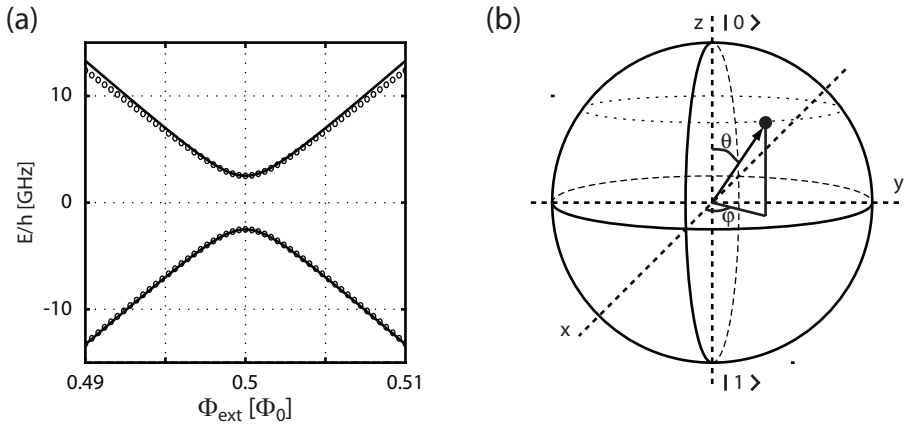

Figure 2.4: (a) Calculated eigenenergies of the full quantum mechanical model (circles) and pseudo spin-$\frac{1}{2}$ model (solid lines). The energy separation at $\Phi_{\text{ext}} = 0.5\Phi_0$ is equal to Δ, and the slopes away from this point are proportional to the persistent currents of the states. (b) Bloch sphere. The quantum mechanical state $|\psi\rangle = \alpha|0\rangle + \beta|1\rangle$ can conveniently be represented by a point on a sphere, with φ the azimuth, and θ the elevation. The state is then given by $|\psi\rangle = \cos(\theta/2)|0\rangle + \sin(\theta/2)e^{i\varphi}|1\rangle$, up to a global phase-factor.

$$|0\rangle = \frac{1}{\sqrt{2\nu^2 + 2\nu\varepsilon}} \begin{pmatrix} \nu + \varepsilon \\ \Delta \end{pmatrix} \tag{2.13}$$

$$|1\rangle = \frac{1}{\sqrt{2\nu^2 + 2\nu\varepsilon}} \begin{pmatrix} -\Delta \\ \nu + \varepsilon \end{pmatrix}. \tag{2.14}$$

The expectation value of the current for the two eigenstates is given by $\langle \hat{I} \rangle = -\frac{\partial E}{\partial \Phi}$. Outside of the degeneracy point, $\langle \hat{I} \rangle$ is different for the two states. This difference can be used for state detection (see Section 2.4).

It is often convenient to describe the quantum mechanical state $|\psi\rangle = \alpha|0\rangle + \beta|1\rangle$ of a two-level system (with $\alpha, \beta \in \mathbb{C}$ and $|\alpha|^2 + |\beta|^2 = 1$) using the Bloch sphere approach [3]. Herein the qubit state is written as

$$|\psi\rangle = \cos\left(\frac{\theta}{2}\right)|0\rangle + \sin\left(\frac{\theta}{2}\right)e^{i\varphi}|1\rangle, \tag{2.15}$$

which can be conveniently visualised as a point on a sphere (see Fig. 2.4(b)). The angle θ determines the angle of the state with respect to the positive z-axis

along which the two eigenstates lie. The angle φ determines the phase in the x, y-plane.

2.1.3 Large loops and additional junctions

Although the qubit as described in the previous section can be realised in practice, some commonly used fabrication techniques and design criteria require extra attention for the proper calculation of its main properties: shadow evaporation and qubits with large self-inductance.

Shadow evaporation: four Josephson junctions Shadow evaporation is a commonly used technique to create Josephson junctions (see Chapter 1). Without additional tricks, this technique intrinsically creates an even number of junctions. The 3-junction model (Eq. 2.5) is easily extended to m junctions:

$$\begin{aligned} L(\vec{\varphi},\dot{\vec{\varphi}}) \;=\; & \sum_{i=1}^{m-1} \frac{e^2}{E_{C,i}} \left(\frac{\Phi_0}{2\pi}\right)^2 \dot{\varphi}_i^2 \\ & + \frac{e^2}{E_{C,m}} \left(\frac{\Phi_0}{2\pi}\right)^2 \left(\sum_{i=1}^{m-1} -\dot{\varphi}_i\right)^2 \\ & - \sum_{i=1}^{m-1} E_{J,i}[1-\cos(\varphi_i)] \\ & - E_{J,m}\left[1-\cos\left(-2\pi\frac{\Phi_{\text{ext}}}{\Phi_0} - \sum_{i=1}^{m-1}\varphi_i\right)\right]. \end{aligned} \tag{2.16}$$

Analogously to the 3-junction case, one degree-of-freedom is eliminated by the fluxoid-quantisation constraint. We find that any number of Josephson junctions larger than three, with one junction smaller than the others, yields qualitatively the same behaviour as in the previous section. Quantitatively, the extra junctions do have a significant contribution to I_p and Δ. In practice the loops have either four or six junctions; here we will focus on the case of four junctions, for which the Hamiltonian reads

$$\begin{aligned} H(\vec{\varphi},\vec{n}) = & \frac{E_C}{(r_1r_2r_3 + r_1r_2r_4 + r_1r_3r_4 + r_2r_3r_4)} \cdot \\ & \big[(r_2r_3 + r_2r_4 + r_3r_4)n_1^2 + (r_1r_3 + r_1r_4 + r_3r_4)n_2^2 + (r_2r_1 + r_2r_4 + r_1r_4)n_3^2 \\ & \quad -2r_3r_4n_1n_2 - 2r_2r_4n_1n_3 - 2r_1r_4n_2n_3\big] \\ & -E_J\big[r_1\cos(\varphi_1) + r_2\cos(\varphi_2) + r_3\cos(\varphi_3) \\ & \quad + r_4\cos(-\varphi_1-\varphi_2-\varphi_3 - 2\pi\frac{\Phi_{\text{ext}}}{\Phi_0})\big], \end{aligned} \tag{2.17}$$

where $[r_1, r_2, r_3, r_4]$ are the relative junctions sizes. We investigate two of the most relevant cases: making the fourth junction either much larger than the original two large junctions, or making it equal to the original two large junctions.

Figure 2.5(a) shows the most common approach: making the extra junction much larger than the other junctions, such that its contribution is negligible ($[\alpha, 1, 1, \beta], \beta >> 1$). We find that for increasing relative size of the fourth junction β, the gap Δ increases and saturates for $\beta \to \infty$. The horizontal dashed line is the calculated value for a 3-junction qubit. As expected, when the fourth junction is very large, it does not contribute to the dynamics, and the system behaves as a 3-junction qubit.

Fig. 2.5(b) shows calculations where all the junctions, except for the α-junction, are of the same size ($\alpha, \beta, \beta, \beta$). As expected, Δ increases for decreasing ratio α/β. The dashed lines indicate the value of β for which the 4-junction qubit has the same energy gap as the equivalent 3-junction qubit ($[\alpha, 1, 1]$). In a rough approximation, the large junctions can be regarded as linear inductors, and the relevant parameter for the size of the gap Δ is the ratio of the inductance of the small α junction to the *sum* of the inductances of the large junctions. The inductance of a junction is given by (see Section 7.1)

$$L_J = \frac{\Phi_0}{2\pi} \frac{1}{I_c}. \tag{2.18}$$

For a fixed size of the smaller junction, the relative sizes of the three large junctions in the 4-junction qubit need to be a factor 1.5 larger than the two large junctions in the 3-junction qubit to achieve the same total inductance. This is roughly confirmed by the result shown in Fig. 2.5(b), as $\beta \approx 1.42$ gives the same gap of a 4-junction qubit as the equivalent 3-junction qubit.

Large-sized qubits: self-inductance To achieve strong coupling between two qubits, or between a qubit and another object like a detector or resonator, it is often desirable to design a large mutual inductance between the two objects. Especially in the case when this mutual inductance is a geometric inductance, this can involve increasing the size and thus the self-inductance of the qubit-loop. For relevant cases, this self-inductance turns out to be non-negligible in the calculation of the qubit properties.

A rigorous model including the self-inductance of the qubit loop is given by Maassen van den Brink *et al.* [4]. It is, however, insightful to consider again the rough approximation that the large junctions in the qubit loop are linear inductors, and the dynamical properties are mostly determined by the ratio of the inductance of the small junction α to the *sum* of the inductances of the large junctions. In this model, the contribution of the self-inductance of the loop can simply be added to the total inductance of the large junctions. We can

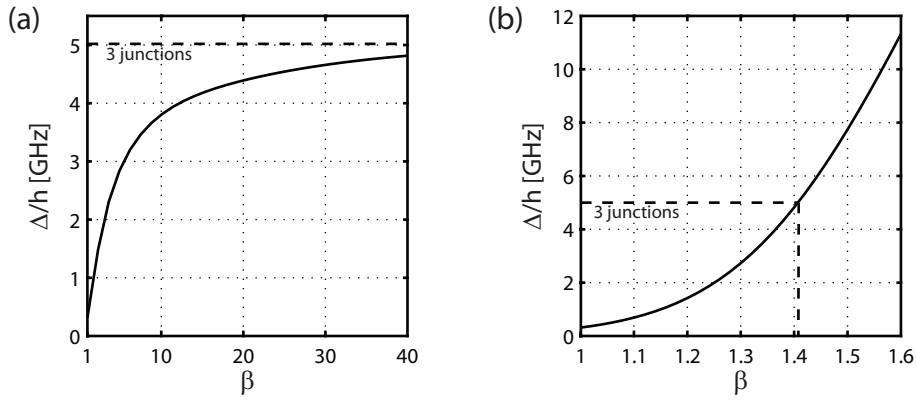

Figure 2.5: Calculated energy gap Δ of a 4-junction qubit versus the relative size β of the large junction(s). (a) The relative junction sizes are given by $[\alpha, 1, 1, \beta]$. For large β of the fourth junction, the energy gap Δ approaches the value of the 3-junction qubit. (b) The relative junctions sizes are $[\alpha, \beta, \beta, \beta]$. The energy gap Δ increases rapidly for increasing ratio β/α. The relative size for which the gap is equal to the 3-junction qubit is indicated by the dashed lines. The calculations were performed using $E_J = h \times 350$ GHz, $E_C = h \times 20$ GHz, and $\alpha = 0.70$.

define a qubit with relative junction sizes $[\alpha, \beta', \beta', \beta']$, with the self-inductance included in rescaled junctions sizes $\beta' > \beta$. From this perspective, it is clear that the gap Δ will sensitively depend on the self-inductance of the loop, as it directly affects the ratio α/β'. The high sensitivity of the gap to the effective α renders this correction extremely important; it has significantly contributed to more reliable predictions of the persistent currents and gaps of some of the experiments presented in this thesis.

2.2 Operation

The operation of a qubit involves inducing well-controlled changes of the quantum-mechanical state. This can be achieved in different ways. The main categories are formed by adiabatic and non-adiabatic shifts of the qubit energy levels, and by driving the qubit with an oscillating field, which can either be resonant or non-resonant with a level splitting in the system.

2.2.1 Larmor precession

For any quantum state that is a superposition of eigenstates of different energies, the relative phases will precess with a frequency ([5], Chapter IV)

$$\omega_{\text{Larmor}} = \nu/\hbar = \omega_{\text{qb}}, \tag{2.19}$$

where ν is the level splitting between the levels. This well-known phenomenon is called *Larmor precession*. As most qubit implementations have a non-zero energy splitting to avoid thermal excitations, the phases of a typical qubit are revolving continuously. In most cases, however, only phase changes *relative* to the precession rate are relevant, naturally leading to the use of a rotating-frame picture. For qubits that have a tunable level splitting, a phase gate can be implemented by inducing an adiabatic shift $\delta\omega_{\text{qb}}$ away from the base splitting ω_{qb} for a time t. In a frame rotating with frequency ω_{qb}, the effective Hamiltonian for this operation is $\hat{H}_{\delta\omega_{\text{qb}}} = -\frac{\delta\omega_{\text{qb}}}{2}\hat{\sigma}_z$. The evolution of the state is described by the operator

$$\begin{aligned} \hat{U}(t) &= e^{-i\frac{\hat{H}_{\delta\omega_{\text{qb}}}}{\hbar}t} \\ &= \begin{pmatrix} \cos\left(\frac{\delta\omega_{\text{qb}}}{2}t\right) + i\sin\left(\frac{\delta\omega_{\text{qb}}}{2}t\right) & 0 \\ 0 & \cos\left(\frac{\delta\omega_{\text{qb}}}{2}t\right) - i\sin\left(\frac{\delta\omega_{\text{qb}}}{2}t\right) \end{pmatrix}. \end{aligned} \tag{2.20}$$

Note that in practice phase gates can often be replaced by a mathematical basis rotation of the succeeding operations.

2.2.2 Rabi oscillations

When a two-level system is driven with a transverse rotating field that is close to resonance with the level splitting, the state of the system will oscillate between the ground and excited state ([5], Chapter IV). These oscillations are called *Rabi oscillations*. For a driving field with amplitude $\hbar\Omega$ and frequency ω, the frequency of these oscillations is given by

$$\omega_{\text{Rabi}} = \sqrt{\Omega^2 + \delta\omega^2}, \tag{2.21}$$

where $\delta\omega = \omega_{\text{qb}} - \omega$ is the detuning between the driving field and the level splitting.

Flux qubits are most naturally driven with an oscillating magnetic field, which, in the persistent current basis, is given by

$$\hat{H}^{[I]}_{\text{AC}} = -\frac{\varepsilon_{\text{AC}}}{2}\cos(\omega t + \varphi)\,\hat{\sigma}_z, \tag{2.22}$$

with $\varepsilon_{\rm AC} = -2I_p\Phi_{\rm AC}$. Transformed to the eigenbasis of the qubit, this driving term reads

$$\hat{H}_{\rm AC}^{[E]} = U_I^{-1}\hat{H}_{\rm AC}^{[I]}U_I = -\frac{\varepsilon}{\nu}\frac{\varepsilon_{\rm AC}}{2}\cos(\omega t+\varphi)\,\hat{\sigma}_z - \frac{\Delta}{\nu}\frac{\varepsilon_{\rm AC}}{2}\cos(\omega t+\varphi)\,\hat{\sigma}_x, \quad (2.23)$$

with $U_I = (|0\rangle|1\rangle)^{[I]}$. Only at the degeneracy point ($\varepsilon = 0$) this driving is purely transverse. Away from the degeneracy point the additional $\hat{\sigma}_z$ contribution complicates the exact evolution of the state. However, this contribution can be neglected for low driving amplitudes. A more detailed description is given in Ref. [6].

The transverse sinusoidal field can be decomposed in a co-rotating and a counter-rotating field. Assuming that the driving field is resonant ($\omega = \omega_{\rm qb}$), the transformation of the system to the rotating frame of the qubit frequency gives

$$\hat{H}_R = U_R^{\dagger}\hat{H}U_R - A = -\frac{1}{2}\frac{\Delta}{\nu}\frac{\varepsilon_{\rm AC}}{2}[i\cos(\varphi)\hat{\sigma}_x + \sin(\varphi)\hat{\sigma}_y], \quad (2.24)$$

where $U_R = e^{-iAt/\hbar}$ and $A = -\frac{\omega}{2}\hat{\sigma}_z$. Here we made a rotating-wave approximation by dropping the counter-rotating fields, which are off-resonant by 2ω.

With this transformed Hamiltonian the solution of the Schrödinger equation is readily obtained, which results in the evolution operator

$$\begin{aligned}\hat{U}(t) &= e^{i\frac{\omega_{\rm Rabi}t}{2}(\cos(\varphi)\hat{\sigma}_x+\sin(\varphi)\hat{\sigma}_y)} \quad (2.25)\\ &= \begin{pmatrix} \cos\frac{\omega_{\rm Rabi}t}{2} & (\sin\varphi + i\cos\varphi)\sin\frac{\omega_{\rm Rabi}t}{2} \\ (-\sin\varphi + i\cos\varphi)\sin\frac{\omega_{\rm Rabi}t}{2} & \cos\frac{\omega_{\rm Rabi}t}{2}\end{pmatrix},\end{aligned}$$

where

$$\omega_{\rm Rabi} = \frac{\Delta}{\nu}\frac{\varepsilon_{AC}}{2}. \quad (2.26)$$

On the Bloch sphere this operation describes in the rotating frame a rotation around an axis in the equatorial plan. The orientation of the axis is determined by the phase φ.

2.2.3 AC Stark effect

The qubit can also be driven with a non-resonant field. For driving fields with a detuning $\delta\omega >> \Omega$, the Rabi oscillations are completely suppressed. The oscillating field, however, causes a net shift of the level splitting given by ([5], Chapter IV)

$$\hbar\delta\omega_{\rm qb} = \frac{\Omega^2}{2\delta\omega}. \quad (2.27)$$

This effect is analogous to the AC Stark effect [7]. The level shift can be used to implement a phase gate, and forms an alternative for the DC shift discussed in Section 2.2.1. The evolution operator is the same as in Eq. 2.21.

For systems of more than one qubit, this dynamical shifting of the levels is very important, albeit most often in a negative sense. When a certain transition in the multi-level system is resonantly driven, all the other levels are slightly shifted, effectively performing a (unwanted) phase-gate. This could also be used to define entangling gates, but most often this is an unwanted effect.

2.3 Decoherence

One of the main limiters on the rate of progress of superconducting quantum circuits is the uncontrolled influence of the environment. It proves hard to control the large number of degrees of freedom in the environment, or alternatively shield the qubits from them. Variations of these parameters in the environment can cause uncontrolled changes of the qubits state, leading to a reduced knowledge of this state, and thus the ability to perform well-defined operations. This process is called decoherence. As most experiments involve averaging over many repetitions of a certain experiment, and each individual realisation is different due to the environmental noise, many critical aspects are lost in the resulting average.

Better understanding of the sources of the noise is essential for improving qubit coherence. We make a distinction between circuit noise from the detectors and control lines, and noise from microscopic fluctuations in the environment. These are discussed in Sections 2.3.2 and 2.3.3, respectively. In the next section we first discuss the mathematical framework for quantifying the rate of decoherence for a general noise source.

2.3.1 General Framework for quantifying decoherence rates

Here we provide the theoretical framework used to predict and analyse the decoherence of our qubits. For an in-depth discussion see Ithier *et al.* [8], from which this paragraph is mainly derived.

The uncontrolled degrees of freedom in the environment appear as noise in the parameters of the qubit Hamiltonian. In the case of the flux qubit, relevant parameters are the flux Φ, the critical currents of the junctions $I_{c,i}$, the bias currents applied through the junctions $I_{b,i}$ and the induced gate charges on the islands in between the junctions $n_{g,ij}$.

Decoherence is characterised by two rates or times: the longitudinal relaxation (depolarisation) rate $\Gamma_1 = T_1^{-1}$ and the transverse relaxation (dephasing) rate

$\Gamma_2 = T_2^{-1}$. The depolarisation is a combination of excitation and relaxation:

$$\Gamma_1 = \Gamma_{rel} + \Gamma_{ex} \underset{\hbar\omega \gg k_B T}{\approx} \Gamma_{rel} = \pi S_{\delta\omega_\perp}(\omega_{ij}), \tag{2.28}$$

where $S_{\delta\omega_\perp}(\omega_{ij})$ is the symmetrised spectral density of the transverse component of the noise at the qubit splitting ω_{ij}. The relaxation dominates over excitation, the latter being exponentially suppressed at low temperature. This rate equation is valid for any spectral shape, since only the density at the qubit energy resonance is important. The relaxation rate can be conveniently expressed in the relevant physical parameters by the qubit sensitivity D to this parameter

$$\Gamma_1 = \pi S_{\delta\omega_\perp}(\omega_{ij}) = \pi D_{\lambda\perp}^2 S_\lambda(\omega_{ij}), \tag{2.29}$$

where

$$D_{\lambda\perp} = \frac{1}{h}\left|\langle j|\frac{\partial H_0}{\partial \lambda}|i\rangle\right|. \tag{2.30}$$

This is a first-order approximation, and can be extended to higher orders as described in Ref. [8].

The dephasing rate Γ_2 is determined by the relaxation rate Γ_1 and by the pure dephasing Γ_φ:

$$\Gamma_2 = \frac{1}{2}\Gamma_1 + \Gamma_\varphi, \tag{2.31}$$

where the pure dephasing rate depends on the spectral density of the longitudinal component of the noise

$$\Gamma_\varphi = \pi \lim_{\omega\to 0} S_{\delta\omega_z}(\omega) = \pi D_{\lambda,z}^2 \lim_{\omega\to 0} S_\lambda(\omega), \tag{2.32}$$

with

$$D_{\lambda,z} = \frac{\partial \omega_{ij}}{\partial \lambda}. \tag{2.33}$$

This description is a first-order approximation, and only valid when the noise has correlation times less than all the (inverse) energies in the system, as well as it should be weak. In addition the spectral shape of the noise has to be smooth from $\omega \approx 0$ up to frequencies of the order of Γ_ϕ. For noise that is less well-behaved, such as the very important 1/f dependent noise, there are alternative approaches to translate the spectral shapes to dephasing rates [8]. Nevertheless, the spectral density at sufficiently low frequency can already yield an insight into the impact of the noise on the qubit dephasing.

2.3.2 Johnson-Nyquist noise in the electrical circuits

The circuits required for the readout and control of the qubit state also introduce noise that can cause the qubit to decohere. As these circuits are critical for the operation of the qubit, the unavoidable decoherence needs to be handled by controlling the noise, rather than removing its source. The two main contributions for electromagnetic noise in the circuit are Johnson-Nyquist noise, originating from the resistive elements in the circuit, and noise from the active elements, such as amplifiers or signal generators. The spectral density of the latter type depends on the details of the device. Therefore, we will only consider Johnson-Nyquist noise in this section. The other sources can be treated similarly.

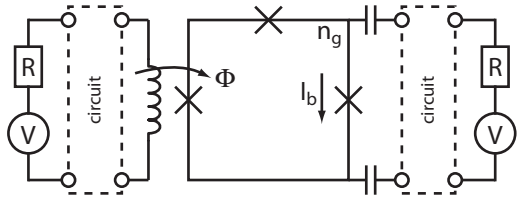

Figure 2.6: Schematic drawing of circuit noise coupling to the qubit. The noise originates from Johnson-Nyquist noise of the resistive elements in the circuit. For a floating qubit there are two main channels that can couple the circuit noise to the qubit. Current carrying lines in the vicinity of the qubit can induce an extra flux Φ into the qubit loop via the mutual inductance M (left). Capacitive coupling to different superconducting islands can cause charge fluctuations (n_g) and high-frequency bias currents running through the junctions (I_b) (right).

Many sources of electromagnetic noise can be modelled using the symmetric Johnson-Nyquist voltage fluctuations of a resistor R at temperature T, given by

$$S_V(\omega) = 2R\hbar\omega \coth \frac{\hbar\omega}{2k_BT}, \tag{2.34}$$

which reduces to $S_V = 4k_BTR$ for $k_BT \gg \hbar\omega$. This noise source is modelled as a voltage source in series with the resistor (see Fig. 2.6).

The resistive element can reside anywhere in the circuit. The noise is transferred through the circuit, with transfer function $A(\omega)$, to the parameter λ (see Section 2.3.1) of the qubit:

$$S_\lambda(\omega) = A^2_{V,\lambda}(\omega) S_V(\omega). \tag{2.35}$$

This approach neatly splits up the decoherence calculations into the spectral density of the source $S_V(\omega)$, the transfer to the qubit $A_{V,\lambda}$, and the sensitivity of the qubit to this noise D_λ.

A simple example is a real impedance R in series with an inductor L which couples inductively to the qubit (see Figure 2.6). Such an RL circuit is a model for the high frequency current bias lines used in the experiments, with R representing the impedance of the transmission line, and L representing the inductance of the line shorting the transmission line close to the qubit. The noise couples to the parameter Φ through the mutual inductance between the bias line and the qubit. In this simple case, we obtain

$$A_{V,\Phi}(\omega) = M\frac{1}{R + j\omega L} \tag{2.36}$$

$$D_{\Phi\perp} = \frac{2I_p}{h}\frac{\Delta}{\nu} \tag{2.37}$$

$$D_{\Phi,z} = \frac{2I_p}{h}\frac{\varepsilon}{\nu}, \tag{2.38}$$

which gives $T_1 = 1.1$ μs and $T_\varphi = \infty$ at the degeneracy point ($\nu = \Delta$), and $T_\varphi = 1.1$ μs and $T_1 = \infty$ far away from the degeneracy point ($\nu \gg \Delta$). For these calculations we used $\nu = h \times 5$ GHz, $I_p = 500$ nA, $R = 50$ Ω, $T = 100$ mK, $L = 0.5$ nH, $M = 1$ pH.

The combined decoherence rates from multiple independent noise sources are simply obtained by the sum of the individual contributions. With this approach many noise sources at different locations and temperatures can be taken into account.

2.3.3 Microscopic noise sources

The influence of microscopic noise sources can be described similarly to circuit noise. However, the coupling to the qubit cannot be engineered as freely as in the case for electric circuits. Therefore, the main route to handle this source of decoherence is given by removal or reduction of the microscopic sources by appropriate choice of materials, or minimising the sensitivity of the qubit to this noise. We discuss three types of microscopic noise sources: charge noise, flux noise, and critical-current noise.

Charge fluctuations Charge noise is a well established phenomenon in solid-state [9]. It is generally associated with electrons hopping between two states, generating random telegraph noise. The combined effect of a large number of these two level fluctuators produces a 1/f shape spectral density. Direct measurements of the charge noise using SETs have yielded typical spectral densities in the order of $10^{-6} \ldots 10^{-7}$ e^2/Hz [10]. For a flux qubit that is not charge-biased at an optimal point, this spectral density translates to typical dephasing times of approximately $1 - 10$ μs. This is the same order of magnitude of the best known flux-qubit devices, and could become a limiting factor in the future.

Magnetic fluctuations Magnetic 1/f noise is also widely encountered in various experiments, and has recently attracted a lot of attention [11, 12, 13]. The origin of this noise is not yet fully established, but is assumed to be connected to the spin of charge-fluctuators. This idea is supported by experiments that show that the effective noise scales with the length of a structure, rather than the area [12], indicating that the origin is local rather than global. The reported spectral densities range over several orders of magnitude $S_\Phi(1\text{Hz}) = 10^{-10} \dots 10^{-13}\ \Phi_0^2/\text{Hz}$ [14, 15]. Inversely, from the best achieved dephasing times of approximately 1 μs in flux qubits, a spectral density of $S_\Phi(1\text{Hz}) = 10^{-12}\ \Phi_0^2/\text{Hz}$ can be deduced. This indicates that the used materials and structures are on the favourable side of the reported spectral densities. Although the qubit is more sensitive to flux than to charge, it is not clear which of the two is dominant.

Critical-current fluctuations Charge fluctuations localised in the barrier of the Josephson junctions may lead to critical-current fluctuations, as the charge distribution in the oxide determines the transparency of the barrier. Single fluctuators have been observed at frequencies comparable to the qubit splitting [16, 17], and for lower frequencies, many of these fluctuators are considered to be the source of the experimentally observed 1/f fluctuations. Typical reported spectral densities are $S_{I_c}(1\text{Hz}) = 10^{-13} A^2/\text{Hz}$ per square micrometer. Measurement on one of our own fabricated junctions provided a similar result of about a quarter of the mentioned value [18]. This spectral density would translate to a dephasing time of approximately 1 to 10 μs, mostly determined by the smallest junction, to which the system is the most sensitive.

2.4 Qubit state detection with a DC-SQUID

The most common detector used for the readout of superconducting qubits is the switching DC-SQUID. Flux qubits produce a net-magnetic field when biased away from the degeneracy point (see Section 2.1.2). This difference in magnetic field can be used to distinguish the states. Figure 2.7 shows a schematic of the SQUID circuit. The circuit can support a supercurrent I_b up to a maximum value $I_{c,\text{sq}}$, which depends on the magnetic field Φ_{sq} penetrating the loop, given by

$$I_{c,\text{sq}} = 2I_c \left| \cos\left(\pi \frac{\Phi_{\text{sq}}}{\Phi_0}\right) \right|, \tag{2.39}$$

where I_c is the critical current of each of the junctions. For bias currents close to or exceeding the critical current, the system can switch to a finite voltage state. This is a stochastic process, and is described by thermal and quantum switching

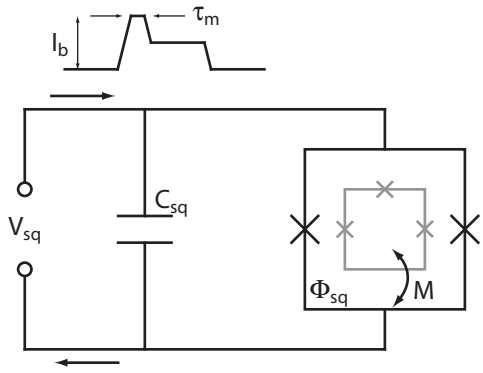

Figure 2.7: Schematic drawing of the SQUID detection circuit. A current pulse is applied to the circuit close to the critical current $I_{c,sq}$, such that the SQUID has a predefined switching probability $P_{\rm sw}$. The switch events are detected by measuring the voltage $V_{\rm sq}$. The switching probability depends on the magnetic flux $\Phi_{\rm sq}$ penetrating the SQUID loop, and is used to detect the difference in flux generated by the two states of the qubit. The SQUID is shunted with a capacitor C_{sq} to control the plasma frequency and the switching statistics.

rates [19]

$$\Gamma_{th}(T, i_b) = f_{\rm pl}(i_b) e^{-\frac{\Delta U(i_b)}{k_B T}} \tag{2.40}$$

$$\Gamma_q(i_b) = f_{\rm pl}(i_b) \sqrt{120\pi \frac{36}{5} \frac{\Delta U(i_b)}{h f_{{\rm pl}(i_b)}}} e^{-\frac{36}{5}\frac{\Delta U(i_b)}{h f_{\rm pl}}}, \tag{2.41}$$

where $i_b = I_b / I_{c,\rm sq}$ is the normalised bias current,

$$\Delta U(i_b) = 2\frac{\Phi_0 I_c}{2\pi}\left(\sqrt{1-i_b^2} - i_b \arccos(i_b)\right) \tag{2.42}$$

is the barrier in the SQUIDs washboard shaped potential, and

$$f_{\rm pl}(i_b) = \frac{1}{2\pi}\sqrt{\frac{2\pi}{\Phi_0}\frac{I_c}{C}} \cdot (1-i_b^2)^{1/4} \tag{2.43}$$

is the plasma frequency of the SQUID. The SQUID circuit is designed such that $\Gamma_q > \Gamma_{th}$.

For the detection process, a short current pulse is applied to the SQUID, with an amplitude close to the critical current. The switching probability is given by

$$P_{\rm sw}(i, \tau_m) = 1 - e^{-\Gamma(i)\tau_m}, \tag{2.44}$$

and depends on the magnetic field, and thereby the state of the qubit. The voltage of the switched state is detected, and the value of $P_{\rm sw}$ is determined by repeating the experiment.

The two expressions for the SQUID switching rates in the classical thermal regime and in the quantum regime have been used to evaluate the switching probability and the detector sensitivity, i.e., the degree to which the detector can discriminate between the two qubit states $|0\rangle$ and $|1\rangle$ with its associated difference in the expectation values of the circulating currents $\Delta I_{10} = \langle I_1\rangle - \langle I_0\rangle$. Note that the quantum regime is most attractive for detection purposes, as its slope $d\Gamma/dI_b$ is larger than its thermal counterpart. However, two words of caution are appropriate on these rate expressions, related to their use if short readout times τ_m are employed, and concerning the role of the temperature. The switching rates (Equations 2.40 and 2.41) have been derived assuming that the loss rate of occupation probability in the meta-stable well is small compared to the plasma frequency of the well, i.e., $\Gamma/\omega_{\rm pl} \ll 1$. With the prefactors in the rate equations being the plasma frequency, this implies that the exponents should be small and so the barrier should be large compared to the temperature or the plasma frequency. The detector sensitivity is at its maximum if the derivative $dP_{\rm sw}/dI_c$ (at fixed I_b) is largest, and this condition is fulfilled if $P_{\rm sw}(I_b) \approx 0.6$. It is easy to see that this implies $\tau_m \approx 1/\Gamma(I_b)$, and so a fast readout requires a large switching rate. As $\Gamma/\omega_{\rm pl} \ll 1$, one finds $\tau_m \ll 1/\omega_{\rm pl}$. In various experiments described in this thesis we employ readout times $\tau_m \approx$ few ns while $\omega_{\rm pl}/(2\pi) \approx 1$ GHz, from which it is obvious that we are well in the limit of the validity of the two escape rate equations (Equations 2.40 and 2.41), stressing the need to be cautious in using these in a quantitative way.

A second aspect of the switching readout is the role of the temperature. While commonly the temperature of the refrigerator is kept in the range of a few tens of mK, this does not imply that the detector will actually operate at that temperature. For one, any noise beyond the local thermal noise level arriving at the SQUID, e.g. via the bias leads, will lead to an effective increase of the switching rate. Also, the switching of the SQUID itself may lead to significant local heating, resulting in an increased local temperature. Consequently, the effective temperature of the SQUID detector can be significantly larger than the refrigerator base temperature, making the detector operate in the thermal regime despite the low base temperature, and consequently reducing its sensitivity below the quantum case.

The switching readout is relatively simple to implement, but the back-action caused by the dissipation is an important concern. In recent work by Picot *et al.* [20] a cryogenic amplifier is employed for ultra fast operation, and a shunting resistor is used to reduce the production of quasi particles. This reduces the main shortcomings of the switching readout method significantly. An alternative

readout method has been developed for flux qubits that uses the inductance of the SQUID rather than the probability to switch to the finite voltage state [21]. The main advantage of this approach is that it completely avoids the dissipation caused by the switched SQUID. In Chapters 7 and 8, the implementation of two of these detectors on a single chip is discussed, and how they can be used for the simultaneous readout of two coupled qubits.

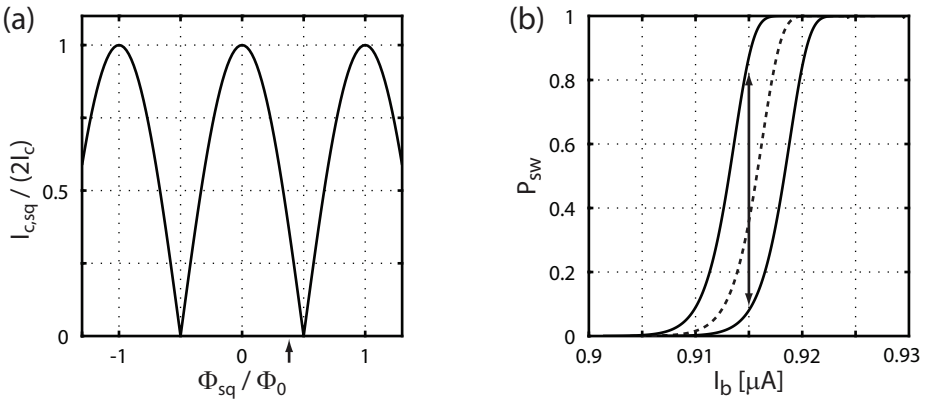

Figure 2.8: (a) Critical current of the SQUID as a function of the $\Phi_{\rm sq}$ picked up by the loop. (b) Switching probability P_{sw} in dependence of the current through the SQUID I_b, for the case of no qubit present (dashed line), the qubit in the ground state $|0\rangle$, and in the excited state $|1\rangle$ (solid lines). For these calculations we assumed only quantum-mechanical tunnelling ($T = 0$), and used $C_{sq} = 6$ pF, $I_c = 1.5$ μA, $\Phi_{\rm sq} = 0.4$ Φ_0, $\tau_m = 20$ ns, $I_{p,qb} = 300$ nA, and $M = 2$ pH.

Bibliography

[1] J. E. Mooij, T. P. Orlando, L. Levitov, L. Tian, C. H. van der Wal, and S. Lloyd, Josephson Persistent-Current Qubit, Science **285**, 1036–1039 (1999).

[2] J. B. Majer, *Superconducting Quantum Circuits*, Ph.d. thesis, Delft University of Technology, 2002.

[3] M. A. Nielsen and I. L. Chuang, *Quantum Computation and Quantum Information*, Cambridge University Press, 2000.

[4] A. Maassen van den Brink, Hamiltonian for coupled flux qubits, Phys. Rev. B **71**, 064503 (2005).

[5] C. Cohen-Tannoudji, *Quantum Mechanics*, J. Wiley and Sons, 1977.

[6] M. C. Goorden, Theory of Josephson persistent-current qubits with driving and dissipation, Master thesis, Delft University of Technology, 2002.

[7] S. H. Autler and C. H. Townes, Stark Effect in Rapidly Varying Fields, Phys. Rev. **100**, 703–722 (1955).

[8] G. Ithier, E. Collin, P. Joyez, P. J. Meeson, D. Vion, D. Esteve, F. Chiarello, A. Shnirman, Y. Makhlin, J. Schriefl, and G. Schön, Decoherence in a superconducting quantum bit circuit, Phys. Rev. B **72**, 134519 (2005).

[9] P. Dutta and P. M. Horn, Low-frequency fluctuations in solids: $1/f$ noise, Rev. Mod. Phys. **53**(3), 497–516 (1981).

[10] M. Kenyon, C. J. Lobb, and F. C. Wellstood, Temperature dependence of low-frequency noise in Al-Al2O3-Al single-electron transistors, Journal of Applied Physics **88**, 6536 (2000).

[11] R. H. Koch, D. P. DiVincenzo, and J. Clarke, Model for $1/f$ Flux Noise in SQUIDs and Qubits, Phys. Rev. Lett. **98**(26), 267003 (2007).

[12] L. Faoro and L. B. Ioffe, Microscopic Origin of Low-Frequency Flux Noise in Josephson Circuits, Phys. Rev. Lett. **100**, 227005 (2008).

[13] S. Choi, D.-H. Lee, S. G. Louie, and J. Clarke, Localization of Metal-Induced Gap States at the Metal-Insulator Interface: Origin of Flux Noise in SQUIDs and Superconducting Qubits, Phys. Rev. Lett. **103**, 197001 (2009).

[14] C. Tesche, K. Brown, A. Callegari, M. Chen, J. Greiner, H. Jones, M. Ketchen, K. Kim, A. Kleinsasser, H. Notarys, G. Proto, R. Wang, and T. Yogi, Practical DC SQUIDs with extremely low 1/f noise, IEEE Trans. Magn. **21**, 1032 (1985).

[15] F. Yoshihara, K. Harrabi, A. O. Niskanen, Y. Nakamura, and J. S. Tsai, Decoherence of flux qubits due to 1/f flux noise, Phys. Rev. Lett. **97**, 167001 (2006).

[16] R. W. Simmonds, K. M. Lang, D. A. Hite, S. Nam, D. P. Pappas, and J. M. Martinis, Decoherence in Josephson Phase Qubits from Junction Resonators, Phys. Rev. Lett. **93**, 077003 (2004).

[17] K. B. Cooper, M. Steffen, R. McDermott, R. W. Simmonds, S. Oh, D. A. Hite, D. P. Pappas, and J. M. Martinis, Observation of Quantum Oscillations between a Josephson Phase Qubit and a Microscopic Resonator Using Fast Readout, Phys. Rev. Lett. **93**(18), 180401 (2004).

[18] J. Eroms, L. C. van Schaarenburg, E. F. C. Driessen, J. H. Plantenberg, C. M. Huizinga, R. N. Schouten, A. H. Verbruggen, C. J. P. M. Harmans, and J. E. Mooij, Low-frequency noise in Josephson junctions for superconducting qubits, Applied Physics Letters **89**, 122516 (2006).

[19] R. F. Voss and R. A. Webb, Macroscopic Quantum Tunneling in 1-μm Nb Josephson Junctions, Phys. Rev. Lett. **47**(4), 265–268 (1981).

[20] T. S. E. Picot, R. N. Schouten, C. J. P. M. Harmans, and J. E. Mooij, QND measurement of the superconducting flux qubit in the weakly projective regime, to be published .

[21] A. Lupaşcu, S. Saito, T. Picot, P. C. de Groot, C. J. P. M. Harmans, and J. E. Mooij, Quantum non-demolition measurement of a superconducting two-level system, Nature Physics **3**, 119–125 (2007).

Chapter 3

Coupled flux qubits

This chapter provides an introduction to the basic properties of a system of two coupled flux qubits. In Section 3.1 we first discuss the mechanisms for coupling flux qubits, and give a simple mathematical description for a system of two coupled flux qubits. This model of two coupled two-level systems, although one of the simplest imaginable, has a rich set of characteristic features. In section 3.2 we discuss the energy spectrum of two coupled flux qubits and present spectroscopy measurements of a two-qubit device with strong ($h \times 1.1$ GHz) coupling. The validity of the simple model is confirmed by a very good agreement with the experiments.

In Section 3.3 we discuss the requirements for an experimental setup to perform a sequence of well-defined operations, such as in a quantum algorithm. As our system is mostly operated through resonant excitation, it is important to consider the phases of all the driving signals. This last section describes how these requirements are implemented in our setup.

3.1 Coupling mechanisms

Superconducting qubits can be coupled in many different ways. All the relevant coupling mechanisms can be categorized as either charge-based [1, 2, 3, 4] or phase-based [5, 6], which indicates the physical quantity that is primarily responsible for the interaction. In addition, coupling can be achieved directly between the qubits [1, 2, 5], or using additional coupling circuits [3, 4, 6]. Additional coupling circuits add complexity, but can have significant benefits, such as tunability of the qubit-qubit coupling, or coupling multiple qubits by acting as a common bus. In this work we focus on direct phase-based coupling, as it is simple to implement and can provide large coupling strengths.

Figure 3.1 shows the three coupling mechanisms that are relevant for the work presented in this thesis. We first discuss Figure 3.1(a), which is the simplest of the three, and derive the proper mathematical expression. The mechanisms shown in Figures 3.1(b,c) are treated next, and are shown to be fully equivalent to the simple case of Figure 3.1(a). For a rigorous theoretical derivation see Reference [7].

We start from the Hamiltonian of two uncoupled qubits (see Section 2.1.2), which in the current basis is given by

$$\hat{H}_{\text{uncoupled}} = (-\frac{\varepsilon_1}{2}\hat{\sigma}_z^1 - \frac{\Delta_1}{2}\hat{\sigma}_x^1) + (-\frac{\varepsilon_2}{2}\hat{\sigma}_z^2 - \frac{\Delta_2}{2}\hat{\sigma}_x^2), \tag{3.1}$$

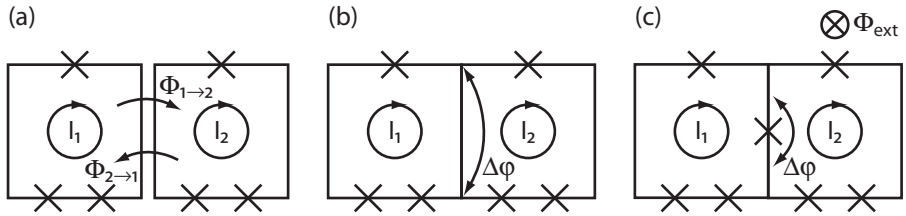

Figure 3.1: Three possible ways of coupling two flux qubits, in order of increasing coupling strength. (a) The qubits are coupled by their geometrical mutual inductance. Flux produced by the current of one qubit is picked up by the other qubit, which changes the total flux penetrating that loop. (b) The two qubits share a common line. Due to the kinetic inductance of the line, the current of one qubit induces a phase difference in the loop of the other, adding to the phase induced by the external magnetic field. The kinetic inductance of the shared line can be made significantly larger than the geometric inductance. (c) Two qubits share an extra junction. Equivalent to the shared line, this couples the qubits by introducing an extra phase in one qubit depending on the current of the other qubit. The Josephson inductance of the shared junction is much larger than the kinetic inductance for typical dimensions.

where $\varepsilon_i = -2I_{p,i}(\Phi_i - \Phi_0/2)$ represents the magnetic energy bias of qubit i, with $I_{p,i}$ the persistent current, Φ_i the flux threading the loop and Φ_0 the superconducting flux quantum, Δ_i is the coupling between the two classical current states, $\hat{\sigma}^1_{x,y,z} = \hat{\sigma}_{x,y,z} \otimes \mathbb{1}$, $\hat{\sigma}^2_{x,y,z} = \mathbb{1} \otimes \hat{\sigma}_{x,y,z}$ and $\hat{\sigma}_{x,y,z}$ are the Pauli spin matrices.

The interaction is based on the magnetic fields that are produced by the currents in the loops. It contains two different contributions. One originates from the flux that is picked up by the other loop and changes the flux bias of that loop. The second contribution is from the total energy in the magnetic field itself. For the contribution based on the flux bias the interaction term is calculated from the operator of the induced flux $\hat{\Phi}_{i\to j}$ produced by qubit i acting on qubit j and the derivative of the Hamiltonian to this flux

$$\begin{aligned} \hat{H}_{\mathrm{int},\Delta\Phi} &= \hat{\Phi}_{1\to 2}\frac{\partial \hat{H}_{\mathrm{uncoupled}}}{\partial \Phi_2} + \hat{\Phi}_{2\to 1}\frac{\partial \hat{H}_{\mathrm{uncoupled}}}{\partial \Phi_1} \\ &= M\hat{I}_{p,1}\hat{I}_{p,2} + M\hat{I}_{p,2}\hat{I}_{p,1} \\ &= 2MI_{p,1}I_{p,2}\hat{\sigma}^1_z\hat{\sigma}^2_z, \end{aligned} \tag{3.2}$$

where M is the mutual inductance between the two qubit loops.

An intuitive picture of this coupling energy is given in Figure 3.2. The flux produced by one qubit changes the energies of the eigenstates of the other qubit. In the figure we take as an example $\Phi_1, \Phi_2 < \frac{1}{2}\Phi_0$ and both qubits are in the

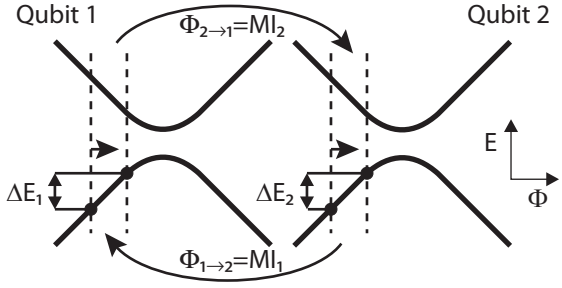

Figure 3.2: Interaction energy based on change in flux bias of the qubits. The flux produced by one qubit shifts the flux bias of the other qubit, thereby changing the energy of the levels.

ground state. Flux produced by the persistent current $I_{p,1}$ in qubit 1 enhances the flux through qubit 2 by an amount of $\Delta\Phi_{1\to 2} = MI_{p,1}$. This raises the energy of qubit 2 by $\Delta E_2 = \Phi_{1\to 2} \cdot \frac{\partial E_2}{\partial \Phi_2} = +MI_{p,1}I_{p,2}$. Similarly we find $\Delta E_1 = +MI_{p,1}I_{p,2}$, giving a total energy contribution of $\Delta E_1 + \Delta E_2 = +2MI_{p,1}I_{p,2}$.

The other contribution to the interaction is related to the inductive energy of the system, i.e. the energy in the magnetic field produced by the qubits. We can

commonly neglect the *self* inductance of the qubits, or, as discussed in Section 2.1.3, can incorporate its effect in the junction values for a good approximation of the systems properties. For describing the coupling energy, the relevant contribution to the field is the *mutual* inductance. For two loops with currents $I_{p,1}$ and $I_{p,2}$ and mutual inductance M, the energy contribution of the mutual inductance is $\Delta E_L = -MI_{p,1}I_{p,2}$ [8]. In the basis of persistent current states this gives the interaction term

$$\hat{H}_{\mathrm{int,L}} = -MI_{p,1}I_{p,2}\hat{\sigma}_z^1\hat{\sigma}_z^2. \tag{3.3}$$

It is clear that for the coupling energy, the contribution of the inductive energy can never be neglected. Adding the two contributions of Equations 3.2 and 3.3 gives the total coupling term

$$\hat{H}_{\mathrm{int}} = +MI_{p,1}I_{p,2}\hat{\sigma}_z^1\hat{\sigma}_z^2 \equiv J\hat{\sigma}_z^1\hat{\sigma}_z^2. \tag{3.4}$$

Note the signs of the interaction terms. For two coupled qubits an anti-ferromagnetic orientation is energetically favorable, while simple loops with currents favor a ferromagnetic orientation.

The other two schemes in Figure 3.1 can easily be shown to be equivalent to the scheme discussed above. The configuration in Fig. 3.1(b) contains an additional coupling energy due to the shared line. For narrow lines the kinetic energy due to the velocity and mass of the charge carriers is not negligible, and is manifest as a series inductance. This phenomenon is referred to as *kinetic inductance*. For a line much thinner than the penetration depth, the current is uniformly distributed, and the kinetic inductance is given by [9]

$$L_{\mathrm{kin}} = \frac{m}{nq^2}\frac{l}{s}, \tag{3.5}$$

where m, n and q are the mass, density and charge of the charge carriers, and l and s are the length and cross-sectional area of the wire. This inductance induces an extra phase difference in the loop, which is equivalent to the effect of the added flux in Figure 3.1(a). Therefore the contribution of the kinetic inductance can be accounted for by simply combining the geometric mutual inductance M_{geo} and the inductance of the shared line M_{kin} into an effective mutual inductance $M = M_{\mathrm{geo}} + M_{\mathrm{kin}}$. For typical line dimensions of flux qubits, which are $100 - 300$ nm in width and $15 - 50$ nm in height, the kinetic inductance can easily dominate the geometric inductance. Especially when small devices are preferred, using the kinetic inductance can greatly enhance the maximum achievable coupling strength J.

The last scheme, shown in Figure 3.1(c) adds an extra junction to the mutual line. The currents of both loops contribute to a phase difference over this junction

as described in Chapter 1. When the current through a junction is significantly smaller than the critical current of the junction, the junction can be regarded as a linear inductor (see Section 7.1). The inductance is called the Josephson inductance and is given by

$$L_{\mathrm{J}} = \frac{\Phi_0}{2\pi}\frac{1}{I_c}. \tag{3.6}$$

Similarly as for the kinetic inductance, the total mutual inductance is $M = M_{\mathrm{geo}} + M_{\mathrm{kin}} + M_{\mathrm{J}}$, where M_{J} is the Josephson inductance of the shared junction. The Josephson inductance of a junction is typically much larger than the geometric and kinetic mutual inductances. In fact, it can be hard to fabricate junctions with a high enough critical current I_c, so that the coupling is not larger than the energy gaps Δ of the qubits, which are typically designed for $h \times 2 \ldots 6$ GHz. Only when very high coupling energies are required this technique is attractive.

In this thesis we focus on systems of two coupled qubits. Obviously, a useful quantum computer requires much more than two qubits, however most proposed methods for operating a multi-qubit system are based on sequences of single- and two-qubit operations. Equivalent to classical logic, a universal set of quantum gates can be made from single- and two-qubit gates, from which any other gate can be derived [10]. There are multiple options for "universal" two-qubit gates. In Chapters 4 and 5 we present experimental results on the implementation of controlled-NOT gates in coupled flux qubits. In practice however, there are still many obstacles to scale a quantum system from two to many qubits. In Chapter 9 some of these obstacles will be discussed.

3.2 Energy spectrum of two coupled flux qubits

3.2.1 Theoretical model

The Hamiltonian of a system of two inductively coupled flux qubits is given by

$$\hat{H} = (-\frac{\varepsilon_1}{2}\hat{\sigma}_z^1 - \frac{\Delta_1}{2}\hat{\sigma}_x^1) + (-\frac{\varepsilon_2}{2}\hat{\sigma}_z^2 - \frac{\Delta_2}{2}\hat{\sigma}_x^2) + J\hat{\sigma}_z^1\hat{\sigma}_z^2, \tag{3.7}$$

where $J = MI_{p,1}I_{p,2}$ is the interaction energy as described in the previous section. The parameters that characterise the system are $I_{p,1}, I_{p,2}, \Delta_1, \Delta_2$ and J; these parameters are the primary design parameters of a two-qubit system. (Note that flux qubits with tunable Δ have been realized [11], but will not be considered here).

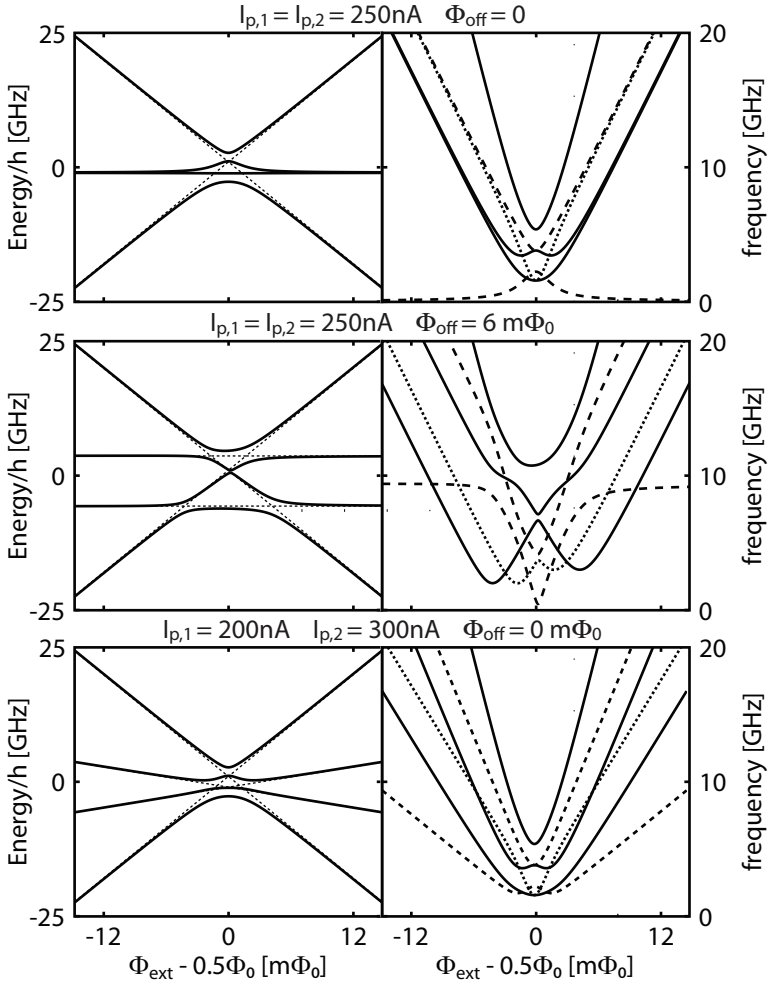

Figure 3.3: Calculated energy-level diagrams (left), and excitation spectra (right) of two coupled qubits versus the applied magnetic flux $\Phi_{\rm ext}$. For all panels $J = h \times 1$ GHz, $\Delta_1 = h \times 2$ GHz and $\Delta_2 = h \times 3$ GHz. In the level diagrams, the dashed lines are the results for $\Delta_1 = \Delta_2 = 0$. In the excitation spectra, the solid (dashed, dotted) lines represent the excitation frequencies from the ground (1st excited, 2nd excited) state. The persistent currents and the flux offset are indicated in the figure.

Figure 3.3 shows the calculated energy-level diagram (left) and excitation spectra (right) versus an externally applied flux Φ_{ext}. In addition to the common external flux, we take into account a flux offset Φ_{off} between the two qubits:

$$\Phi_1 = \Phi_{\text{ext}} + \frac{\Phi_{\text{off}}}{2} \tag{3.8a}$$

$$\Phi_2 = \Phi_{\text{ext}} - \frac{\Phi_{\text{off}}}{2}. \tag{3.8b}$$

If Φ_{off} is non-zero, the two qubits have their degeneracy point at different Φ_{ext}, which is often the case experimentally. The same effect could be caused by an inhomogeneity of the magnetic field, or by a difference in area of the two qubit loops. In practice however, it is hard to distinguish between these effects, so we will treat them all as an offset Φ_{off}.

For the top two panels in Figure 3.3 the persistent currents are equal and there is no flux offset between the two qubits. In the energy-level diagrams the dashed lines represent the results for $\Delta_1 = \Delta_2 = 0$, which we refer to as the "classical" or "persistent current" states. The derivatives of the four energy levels are $dE/d\Phi_{\text{ext}} = \pm(I_{p,1} + I_{p,2})$ for the classical parallel states, and $dE/d\Phi_{\text{ext}} = \pm(I_{p,1} - I_{p,2}) = 0$ for the classical anti-parallel states. The finite energy gaps Δ_1 and Δ_2 are observed as anti-crossings in the level-diagram. The qubit-qubit coupling is easily observed at $\Phi_{\text{ext}} = 0.5\Phi_0$, as the vertical displacement between the classical anti-parallel states and the classical parallel states. This displacement is equal to $2J$, explained by the energy cost of J for parallel states and energy gain of J for anti-parallel states. The middle and bottom panels show the results for finite flux offset and different persistent currents respectively.

3.2.2 Spectroscopy measurements

As the fabrication process inevitably leads to spread in the system parameters, any experiment with flux qubits will generally start by determining these parameters from a spectroscopy-type experiment. In this experiment an AC driving pulse is applied to the system after which the state of the qubits is read out. This procedure is repeated, varying the frequency of the driving pulse and the flux bias. Whenever the frequency of the driving signal matches an energy difference in the (four-level) system, exchange of populations between the levels can occur, and potentially lead to a change in the detector signals.

The experiments presented here are performed with the device depicted in Figure 3.4, which contains a single DC-switch type detector for the combined readout of both qubits (see Section 2.4), and uses an external coil for the flux bias Φ_{ext} (see Eq. 3.8).

The spectroscopy results are shown in Figure 3.5. Panel (b) shows the calculated resonance frequencies from Eq. 3.7 superimposed on the data of (c),

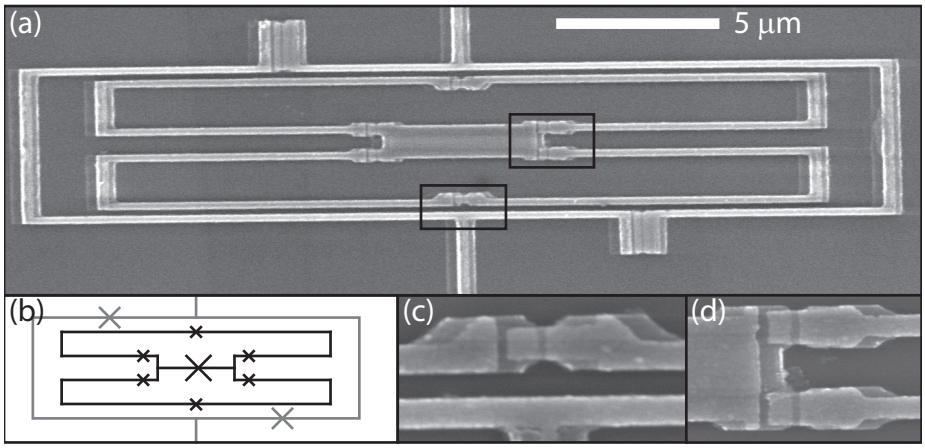

Figure 3.4: (a) Scanning Electron Micrograph of a device with two coupled qubits. The outer loop is the SQUID magnetic field detector, which was operated in the DC-switch mode and detects the combined field of both qubits. In the SQUID loop are the two qubit loops, both connected to a large junction, formed by the entire central island. The coupling junction has a critical current of $I_c = 44$ μA. (b) Schematic representation of the qubit circuit (black) and SQUID circuit (grey). (c,d) Magnification of the junctions indicated in panel (a).

using $I_{p,1} = 270$ nA, $\Delta_1 = h \times 1.74$ GHz, $I_{p,2} = 250$ nA, $\Delta_2 = h \times 0.50$ GHz, $J = h \times 1.1$ GHz and $\Phi_{\rm off} = 5.8$ mΦ_0. The resonances from the ground state to the excited states are easily recognized (solid lines). In addition we observe two resonances that correspond to excitations from the first excited state to higher excited states. This indicates that the first excited state has a non-negligible population, which is likely due to the non-zero effective temperature. The experiment was performed at an elevated temperature of 100 mK to enhance the visibility of these lines. Only the resonance between the second and third excited state is not present, as the temperature is not high enough to provide sufficient population of the second excited state.

We conclude from the good agreement between experiment and calculations, that the simple model of two two-level systems, with a $\hat{\sigma}_z^1\hat{\sigma}_z^2$-type coupling (in the persistent-current basis) is a good description of two inductively coupled flux qubits. We now proceed to investigate coherent operations in this system and discuss the related requirements of an experimental setup.

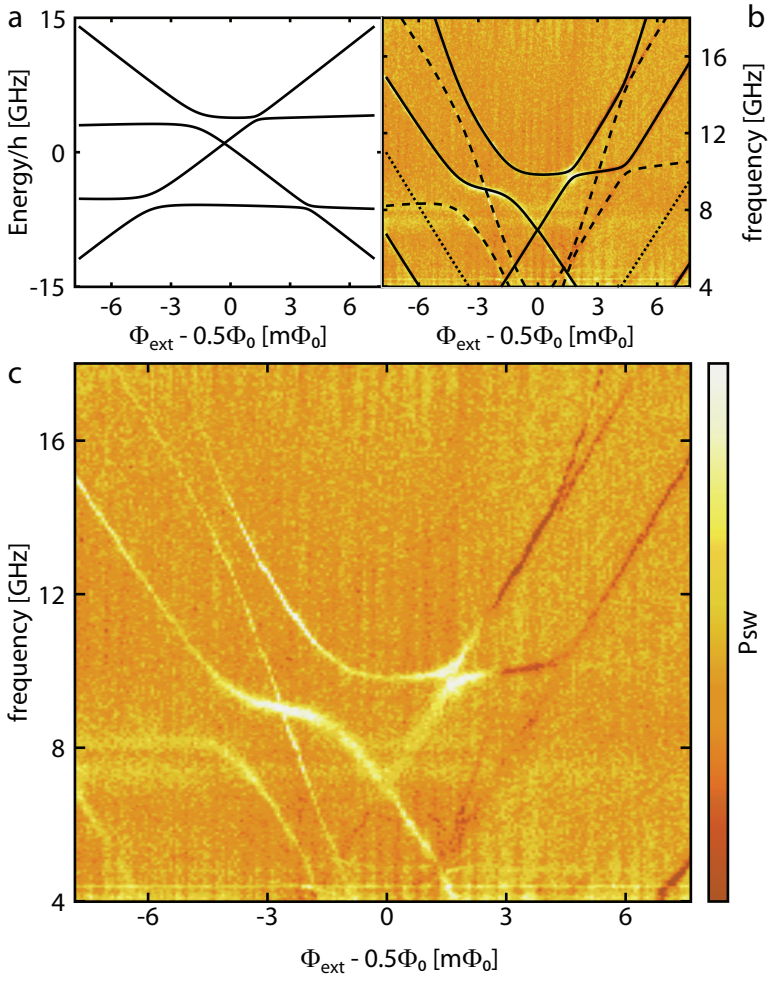

Figure 3.5: Measurement results for spectroscopy experiments performed on the device depicted in Fig. 3.4. (c) The SQUID switching probability in color, versus the excitation frequency and flux bias Φ_{ext}. The top panels show the theoretical fit of the excitation spectrum superimposed on the data (b), and the corresponding energy levels (a). Measurements were performed at a temperature of 100 mK.

3.3 Requirements for performing a quantum-algorithm

One of the main applications of qubits is to serve as the logical units in a quantum computer. The computational operations, or gates, are physical manipulations performed on the system that lead to a well-defined state-change of one or more qubits. There are three basic types of physical implementations of quantum gates: (1) driving the system with an AC-signal that is resonant with a level splitting in the system, (2) changing one of the parameters in the system non-adiabatically and (3) changing one of the parameters in the system adiabatically. The first two are useful for changing qubit state populations; the third can only be used to perform phase-changes. In addition to the three basic types mentioned here, there also exist more advanced types of control operations. These advanced operations commonly involve pulse-shaping and are designed for example to enhance gate fidelity or gate speed.

In the following section we will study gates based on resonant driving. These gates provide a universal set of gates. Non-adiabatic shifts are rarely used in flux qubit systems, as for typical flux qubit parameters the demands on bandwidth and transmission for the experimental setup are higher than for gates based on resonant driving. Adiabatic shifts can be used to perform single- and two-qubit phase-gates. Single-qubit phase-gates are not very important, as algorithms can often be transformed to a form without these gates. Two-qubit phase gates are of interest for creating entanglement between two (flux) qubits, but will not be discussed further.

3.3.1 Single- and two-qubit gates based on resonant driving: a universal set

Resonant driving between any two states in a coupled two-qubit system can be described analogously to the single-qubit driving discussed in Section 2.2.2. Neglecting any spurious driving of the other transitions, the 4-level system can simply be reduced to the 2 levels for which the driving is resonant. Expressed in the rotating frame of a two-level system this yields

$$e^{i\frac{\omega\tau}{2}(\cos\varphi\sigma_x+\sin\varphi\sigma_y)} = \begin{pmatrix} \cos\frac{\omega\tau}{2} & (\sin\varphi + i\cos\varphi)\sin\frac{\omega\tau}{2} \\ (-\sin\varphi + i\cos\varphi)\sin\frac{\omega\tau}{2} & \cos\frac{\omega\tau}{2}, \end{pmatrix}, \tag{3.9}$$

where ω corresponds to the Rabi frequency, τ is the duration of the applied resonant driving. The phase φ relates to the microwave phase and determines the angle of the rotation axis in the x, y-plane. We will assume that all resonance

frequencies in the system are unique, which for inductively coupled flux qubits is *not* the case at $\Phi_1 = \Phi_0/2$ or $\Phi_2 = \Phi_0/2$ or both; Chapter 5 studies the case of degenerate transitions at $\Phi_1 = \Phi_2 = \Phi_0/2$.

To keep the expressions compact we assume $\varphi = 0$, which describes rotations around the x-axis of the Bloch-sphere. Any other axis in the equatorial plane can be obtained for proper choice of φ. To indicate on which qubit a certain gate operates, we use the logical-bit notation {00, 01, 10, 11} for the energy levels {$|0\rangle$, $|1\rangle$, $|2\rangle$, $|3\rangle$}, which away from the degeneracy points of the qubits correspond to the persistent-current states. The four operations corresponding to the four transition frequencies that involve flipping a single qubit are represented by

$$\hat{R}_{00-01}(\omega,\tau) = \begin{pmatrix} \cos\frac{\omega\tau}{2} & i\sin\frac{\omega\tau}{2} & 0 & 0 \\ i\sin\frac{\omega\tau}{2} & \cos\frac{\omega\tau}{2} & 0 & 0 \\ 0 & 0 & 1 & 0 \\ 0 & 0 & 0 & 1 \end{pmatrix} \tag{3.10a}$$

$$\hat{R}_{10-11}(\omega,\tau) = \begin{pmatrix} 1 & 0 & 0 & 0 \\ 0 & 1 & 0 & 0 \\ 0 & 0 & \cos\frac{\omega\tau}{2} & i\sin\frac{\omega\tau}{2} \\ 0 & 0 & i\sin\frac{\omega\tau}{2} & \cos\frac{\omega\tau}{2} \end{pmatrix} \tag{3.10b}$$

$$\hat{R}_{00-10}(\omega,\tau) = \begin{pmatrix} \cos\frac{\omega\tau}{2} & 0 & i\sin\frac{\omega\tau}{2} & 0 \\ 0 & 1 & 0 & 0 \\ i\sin\frac{\omega\tau}{2} & 0 & \cos\frac{\omega\tau}{2} & 0 \\ 0 & 0 & 0 & 1 \end{pmatrix} \tag{3.10c}$$

$$\hat{R}_{01-11}(\omega,\tau) = \begin{pmatrix} 1 & 0 & 0 & 0 \\ 0 & \cos\frac{\omega\tau}{2} & 0 & i\sin\frac{\omega\tau}{2} \\ 0 & 0 & 1 & 0 \\ 0 & i\sin\frac{\omega\tau}{2} & 0 & \cos\frac{\omega\tau}{2} \end{pmatrix}. \tag{3.10d}$$

Each of these operations can be used as an entangling gate. For instance if $\omega\tau = \pi$, Equations 3.10(a) and (b) are 0- and 1-controlled NOT gates up to a single-qubit rotation, with the first qubit acting as the control, and the second qubit as the target qubit. Similarly for Equations 3.10(c) and (d), with the role of target and control reversed. Combined with the single-qubit z-rotation, Eq.

3.10(a) performs the well-known CNOT gate up to a global phase factor,

$$\hat{R}_{\mathrm{qb1},z}\left(-\frac{\pi}{2}\right)\cdot\hat{R}_{10-11}\left(\pi\right)=$$
$$\frac{\sqrt{2}}{2}\begin{pmatrix}1+i & 0 & 0 & 0\\ 0 & 1+i & 0 & 0\\ 0 & 0 & 1-i & 0\\ 0 & 0 & 0 & 1-i\end{pmatrix}\begin{pmatrix}1 & 0 & 0 & 0\\ 0 & 1 & 0 & 0\\ 0 & 0 & 0 & i\\ 0 & 0 & i & 0\end{pmatrix}=$$
$$\frac{\sqrt{2}}{2}\left(1+i\right)\begin{pmatrix}1 & 0 & 0 & 0\\ 0 & 1 & 0 & 0\\ 0 & 0 & 0 & 1\\ 0 & 0 & 1 & 0\end{pmatrix}=e^{i\frac{\pi}{4}}M_{\mathrm{CNOT}}. \tag{3.11}$$

Single-qubit phase-gates are in practice often not necessary, because they can be accounted for by a mathematical transformation of the following gates.

A single qubit rotation is realized by combining the appropriate 0- and 1-controlled operations,

$$\hat{R}_{\mathrm{qb2}}(\omega,\tau)=\hat{R}_{00-01}\cdot\hat{R}_{10-11}=\begin{pmatrix}\cos\frac{\omega\tau}{2} & i\sin\frac{\omega\tau}{2} & 0 & 0\\ i\sin\frac{\omega\tau}{2} & \cos\frac{\omega\tau}{2} & 0 & 0\\ 0 & 0 & \cos\frac{\omega\tau}{2} & i\sin\frac{\omega\tau}{2}\\ 0 & 0 & i\sin\frac{\omega\tau}{2} & \cos\frac{\omega\tau}{2}\end{pmatrix} \tag{3.12}$$

These single qubit gates combined with the conditional NOT gates above together form a universal set with which any other operation can be made [10].

Two sequentially driven CNOT gates induce a phase operation,

$$\hat{R}_{10-11}\left(\pi\right)^2=\hat{R}_{10-11}\left(2\pi\right)=$$
$$\begin{pmatrix}1 & 0 & 0 & 0\\ 0 & 1 & 0 & 0\\ 0 & 0 & 0 & i\\ 0 & 0 & i & 0\end{pmatrix}^2=\begin{pmatrix}1 & 0 & 0 & 0\\ 0 & 1 & 0 & 0\\ 0 & 0 & -1 & 0\\ 0 & 0 & 0 & -1\end{pmatrix}=M_{\mathrm{PHASE}}. \tag{3.13}$$

Using two consecutive microwave pulses all four Bell-states can be generated,

$$|\beta_{00}\rangle=\frac{|00\rangle+|11\rangle}{\sqrt{2}}=\hat{R}_{10-11}\left(-\pi\right)\cdot\hat{R}_{00-10}\left(\frac{\pi}{2}\right)\cdot|00\rangle \tag{3.14a}$$

$$|\beta_{01}\rangle=\frac{|00\rangle-|11\rangle}{\sqrt{2}}=\hat{R}_{10-11}\left(\pi\right)\cdot\hat{R}_{00-10}\left(\frac{\pi}{2}\right)\cdot|00\rangle \tag{3.14b}$$

$$|\beta_{10}\rangle=\frac{|01\rangle+|10\rangle}{\sqrt{2}}=\hat{R}_{00-10}\left(\pi\right)\cdot\hat{R}_{00-01}\left(\frac{\pi}{2}\right)\cdot|00\rangle \tag{3.14c}$$

$$|\beta_{11}\rangle=\frac{|01\rangle-|10\rangle}{\sqrt{2}}=\hat{R}_{00-10}\left(-\pi\right)\cdot\hat{R}_{00-01}\left(\frac{\pi}{2}\right)\cdot|00\rangle. \tag{3.14d}$$

3.3.2 Phase requirements when employing multiple driving frequencies

In the previous section we showed that resonant driving of the four primary transitions in a two-qubit system provides a universal set of gates. The required AC-signals will in practice be generated by four independent AC-sources, each set to one of the four transition frequencies. As the phase of an AC-signal determines the rotation axis for a certain operation, the phase requirements for the AC-signals need to be considered.

In most experiments the measurement outcome is obtained from averaging over a large number of individual realisations of operations and sequential read-out. In the absence of phase-locking between the AC-signals and the repetition rate of the experiment, every individual experiment will start with a different phase of the AC-signals. For a single-qubit experiment this is not a problem, because the initial orientation, or angle, of the computational rotating frame can be freely defined. The first AC-pulse applied to a qubit in the ground state *defines* the orientation of the rotating frame, and the phase of following AC-pulses are defined relative to the first pulse.

For a two-qubit experiment, with four relevant transition frequencies, the associated phases are not independent, as we will derive below. Note that if the *absolute* phases need to be well-defined, and not only the *relative* phases, also the exact timing of the AC-pulses becomes important, and thus the time jitter of the pulse-source that created envelopes of the AC-pulse. Therefore special attention is also given to the timing.

We consider four transitions with angular frequencies $\omega_1 - \omega_J$, $\omega_1 + \omega_J$, $\omega_2 - \omega_J$ and $\omega_2 + \omega_J$, which is typical for two inductively coupled flux qubits biased outside their degeneracy points ($\omega_J = J/\hbar$). We take four AC-sources, with angular frequencies ω_A, ω_B, ω_C and ω_D, and at time $t = t_0$ have phases φ_A, φ_B, φ_C and φ_D. The sources produce the effective rotating fields $\exp(-i(\omega_i(t - t_0) + \varphi_i))$, with $i = \{A, B, C, D\}$, and are each in resonance with one of the transitions

$$\omega_1 - \omega_J = \omega_A \tag{3.15a}$$

$$\omega_1 + \omega_J = \omega_B \tag{3.15b}$$

$$\omega_2 - \omega_J = \omega_C \tag{3.15c}$$

$$\omega_2 + \omega_J = \omega_D. \tag{3.15d}$$

Now consider the four-dimensional rotating frame that is co-rotating with all of the four resonances:

$$e^{-i(\omega_1 t+\varphi_1)\hat{\sigma}_z^1/2} e^{-i(\omega_2 t+\varphi_2)\hat{\sigma}_z^2/2} e^{-i(\omega_J t+\varphi_J)\hat{\sigma}_z^1\hat{\sigma}_z^2/4}, \tag{3.16}$$

where φ_1, φ_2 and φ_J are the initial phases of the rotating frame, and are free to define. If we choose these phases to line up with the phases of the AC-sources, the operations in the resulting rotating frame would be rotations around the x-axis. In this case the conditions are

$$(\omega_1 - \omega_J)t_0 + \varphi_1 - \varphi_J = \varphi_A \tag{3.17a}$$

$$(\omega_1 + \omega_J)t_0 + \varphi_1 + \varphi_J = \varphi_B \tag{3.17b}$$

$$(\omega_2 - \omega_J)t_0 + \varphi_2 - \varphi_J = \varphi_C \tag{3.17c}$$

$$(\omega_2 + \omega_J)t_0 + \varphi_2 + \varphi_J = \varphi_D. \tag{3.17d}$$

Note that if the phases match at $t = t_0$, they will always match as the frame runs at the same rate as the AC-signals. For rotations around the y-axis the right-hand side of Equation 3.17 would have an additional term $+\pi/2$. Any arbitrary axis in the equatorial plane can be chosen using appropriate phase factors.

The main question to be answered is whether there exist values for φ_1, φ_2 and φ_J that solve Equations 3.17, and ultimately, if there are constraints on the phases φ_A, φ_B, φ_C and φ_D and timing t_0. For convenience we write Eq. 3.17 in matrix notation

$$\begin{pmatrix} \omega_1 - \omega_J & 1 & 0 & -1 \\ \omega_1 + \omega_J & 1 & 0 & 1 \\ \omega_2 - \omega_J & 0 & 1 & -1 \\ \omega_2 + \omega_J & 0 & 1 & 1 \end{pmatrix} \begin{pmatrix} t_0 \\ \varphi_1 \\ \varphi_2 \\ \varphi_J \end{pmatrix} = \begin{pmatrix} \varphi_A \\ \varphi_B \\ \varphi_C \\ \varphi_D \end{pmatrix} \tag{3.18}$$

This is a set of linearly dependent equations, i.e. the determinant is zero. This is clearer if we make a change of basis

$$\begin{pmatrix} \omega_1 & 1 & 0 & 0 \\ \omega_J & 0 & 0 & 1 \\ \omega_2 & 0 & 1 & 0 \\ \omega_J & 0 & 0 & 1 \end{pmatrix} \begin{pmatrix} t_0 \\ \varphi_1 \\ \varphi_2 \\ \varphi_J \end{pmatrix} = \begin{pmatrix} (\varphi_A + \varphi_B)/2 \\ (\varphi_A - \varphi_B)/2 \\ (\varphi_C + \varphi_D)/2 \\ (\varphi_C - \varphi_D)/2 \end{pmatrix} \tag{3.19}$$

We conclude that the phases of the AC-sources need to satisfy $\varphi_A - \varphi_B = \varphi_C - \varphi_D$. Under this condition the remaining requirements are expressed by

$$\begin{pmatrix} \omega_1 & 1 & 0 & 0 \\ \omega_2 & 0 & 1 & 0 \\ \omega_J & 0 & 0 & 1 \end{pmatrix} \begin{pmatrix} t_0 \\ \varphi_1 \\ \varphi_2 \\ \varphi_J \end{pmatrix} = \begin{pmatrix} (\varphi_A + \varphi_B)/2 \\ (\varphi_C + \varphi_D)/2 \\ (\varphi_C - \varphi_D)/2 \end{pmatrix} \tag{3.20}$$

These equations can be solved for *any* t_0. This means that the *exact* timing does not play a role, and neither do the absolute phases of the AC-signals. The

requirement $\varphi_A - \varphi_B = \varphi_C - \varphi_D$ involves only relative phases, and is conveniently (but not surprisingly) time-independent because $\omega_A - \omega_B = \omega_C - \omega_D$. In practice however, the requirement that the four AC-sources need to maintain a fixed phase relation throughout an entire experiment, which can take several hours, is not easily satisfied. In the next section we will discuss some critical components in the setup that were built to reach the derived condition.

3.3.3 Hardware for phase and timing control

In this section we show how we control and monitor the phases of all the AC-signals used in the experiments and how we control the timing of the experiments. Several components were designed specifically for this experiment; the electrical designs and concepts were made by Raymond Schouten.

Figure 3.6 shows a schematic overview of the relevant parts of the measurement setup. We distinguish two main channels: The (continuous) 10 MHz clock (black/white), and the trigger circuit that determines the timing of every individual experiment (white/grey).

stable 10 MHz distribution The whole experiment runs on a single clock, represented in the Figure by "10 MHz Ref". This signal is split into multiple lines to provide all the parts of the setup with the common clock. We found that the phase stability of this 10 MHz splitter is critical for the stability of the relative phases of the outputs of the AC-sources. The splitter was designed and built in-house; Figure 3.7(a) shows a photograph of the front-panel. The critical design point is the amplification of the input signal *before* splitting into the separate channels. This prevents the introduction of uncorrelated noise between the channels, which is the case for many commercially available splitters. The phase stability is 0.5 degrees peak-to-peak at 10 GHz, measured over 100 s.

phase-stable AC-sources The heart of the setup is formed by the AC-sources. If the AC-sources do not have sufficient phase-stability over a typical time-scale of minutes, it becomes extremely impractical, if not impossible, to measure and adjust the phases in between measurements. For the phase-critical experiments we used Agilent E8257D signal generators (with 'low noise'-option "UNX"). These generators have a frequency range of 1kHz to 20GHz. Phase stability measurements taken over a period of 24 hours showed a variation of $\approx$ 10 degrees at 10 GHz, mainly caused by the temperature difference between day and night of $\approx$ 5 °C. Together with the phase-monitoring discussed next, this is considered sufficient for all near-future multi-qubit experiments.

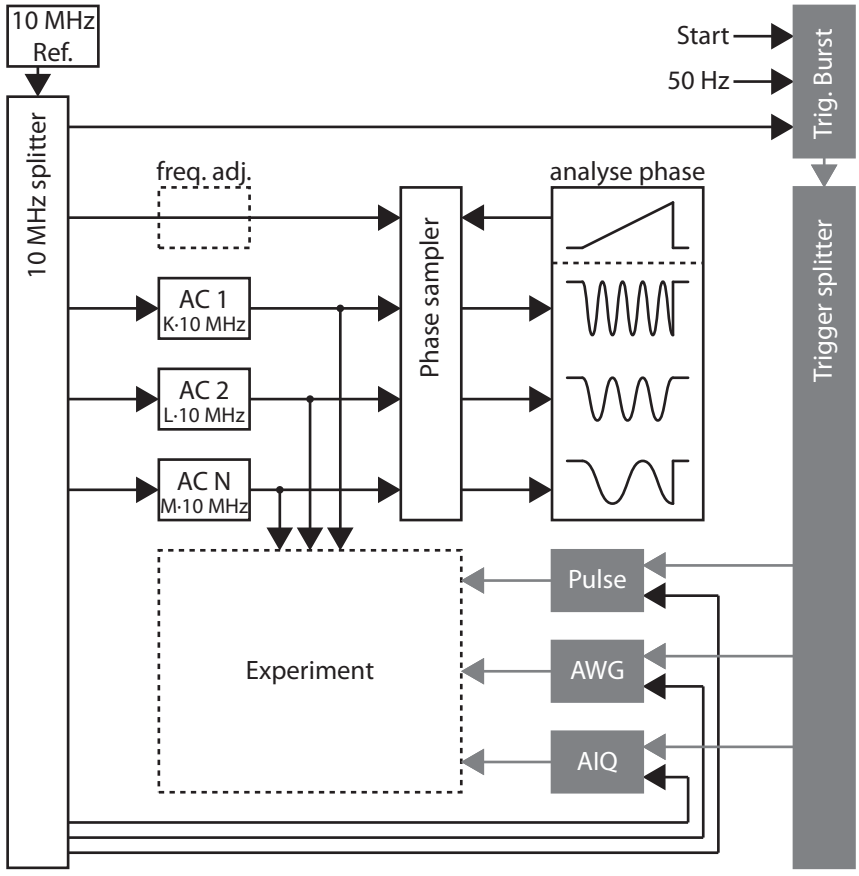

Figure 3.6: Schematic representation of the phase and timing control in the experimental setup. The 10 MHz clock and AC-phase control circuitry is drawn in black and white. The trigger and timing circuitry is drawn in white and grey. The dashed box "freq. adj." was not used in any of the experiments, but indicates the place where a frequency adjustment could be made to achieve a frequency resolution of the AC-sources higher than 10 MHz.

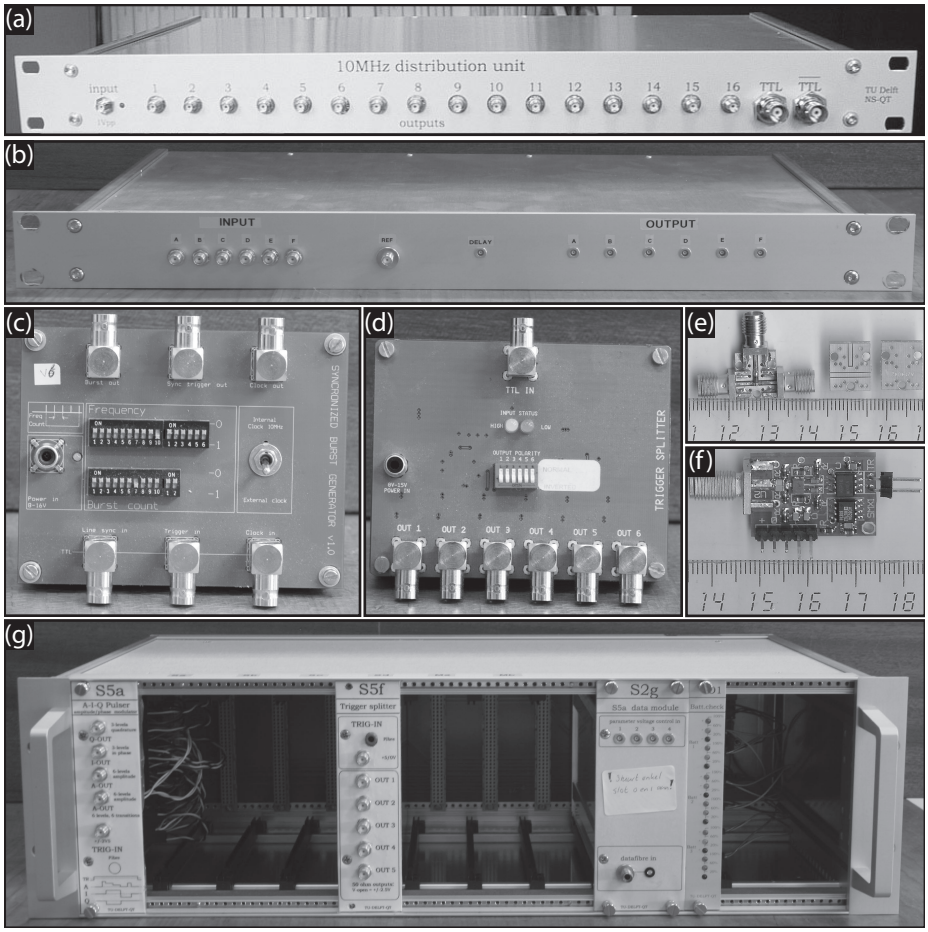

Figure 3.7: Photographs of the electronics devices built for phase and timing control. (a) Stable 10 MHz distribution. (b) Phase sampler for monitoring the phase of the AC-sources. (c) Trigger burst generator. Inputs are a starting trigger signal, 50 Hz line-sync signal and a 10 MHz reference clock. Outputs are a trigger-pulse-train with jumper-programmable frequency and trigger count, 10 MHz clock, and start-time of the burst. (d) Trigger splitter (e) Microwave Tee for splitting of ≈ -20 dB of the signal of the AC-sources (f) Sampling head as used in (b), (g) 19“ frame with ”AIQ“-pulse module, trigger splitter, and computer interface from left to right.

phase monitoring of AC-sources To be able to verify and correct the phase of the AC-sources, we monitor their output signals. This is done by splitting off a small portion of the signal (≈ -20 dB) and sampling the amplitude of the wave with a pulse of ≈ 70 ps. The delay of this pulse can be controlled with a DC-voltage. The measurement is repeated for various delays, over a range of 1.5 ns, which gives at least one full period for all signal frequencies above 0.7GHz. The resulting wave is fit with a sine function and the phase is determined. This procedure gives a reliable phase measurement (± 3 degrees at 5 GHz) of four AC-sources well within 0.5 s. Figure 3.7(b) shows a photograph of the front of the device, Figure 3.7(e) shows the splitter for the AC-signal and 3.7(f) the sampling head.

low-jitter trigger distribution and synchronization to 10 MHz Jitter is the time variation of a periodic signal with respect to a reference time. In the experiments we use different types of timed pulses, for instance magnetic-shift pulses applied to the qubit, or the envelopes of the AC-pulses for qubit control or readout. All the timed sources, such as pulse sources or arbitrary waveform generators, are triggered with the same trigger-burst. This trigger burst is generated by the device depicted in Figure 3.7(c), and is based on a programmed micro-controller and runs synchronized with the 10 MHz clock. The start of the burst is triggered with an external TTL signal ("start"), which is produced by the computer that controls the measurement. After the micro-controller detects a "start"-event, it waits for a zero-crossing of the power grid ("50 Hz") and initiates a burst of triggers. The frequency of the burst, and the number of pulses within the burst are programmable by jumpers. When the burst is generated it is distributed by the "Trigger splitter" (Figure 3.7(d)). The jitter of the 'trigger-burst'-unit is 25 ps peak-to-peak, and the trigger jitter of the 'trigger-splitter'-unit is < 20 ps peak-to-peak (both measured over 100 s).

low-trigger-jitter pulse-sources Anticipating experiments demanding many pulses and high timing accuracy we developed a multi-level pulse source. Figure 3.7(g) shows a photograph of a 19"-frame, containing three modules. The module on the left, labeled "S5a", is the pulse source. It is based on an analogue voltage ramp, defining the time delay and initiated by an external trigger, and on comparators that define the time events. Both the ramp time and comparator voltage are programmable through on-board DAC's, with a maximum resolution of 2 ps for the fastest ramp of 100 ns. Every time the voltage-ramp surpasses a comparator value, an additional output voltage is added, with a typical rise-time of 1 ns. The jitter of these timing events with respect to the external trigger is 100 ps peak-to-peak (measured over 100 s). The two main outputs, labeled "A", are identical and can output one voltage-level for each timing event. The

secondary outputs, "I" and "Q", have independent levels, but are only triggered by three of the six time-events. If employed together with RF-mixers, this combination of pulses can be used to create 3 AC-pulses with independent phase and amplitude. Alternatively, output "A" can be used to create a pulse of maximally 6 independent levels.

The other two modules in the rack are a dedicated trigger splitter (30 ps trigger jitter peak-to-peak over 100 s), so several modules in the rack can be triggered using only one external trigger, and a data-module that is used to program the on-board DAC's from a computer.

The commercial pulse sources we used in some experiments are the Agilent 81110A (5 ps time-resolution, 3 ns trigger jitter peak-to-peak), Bergman-SG02 delay cards (25 ps time-resolution, 250 ps trigger jitter RMS), and for generating arbitrary waveforms we used the Tektronix AWG520 (1 ns time-resolution, 1 ns trigger jitter peak-to-peak). Jitter values are based on external triggering.

In this Chapter we discussed the basic properties of coupled flux qubits and how such a system is operated. The phase- and timing-critical parts of the experimental setup are explained, and we conclude that the setup fulfills the basic requirements for performing a multi-pulse experiment such as a quantum algorithm. The next two chapters will employ these results in the experimental demonstration of entangling gates.

Bibliography

[1] T. Yamamoto, Y. A. Pashkin, O. Astafiev, Y. Nakamura, and J. S. Tsai, Demonstration of Conditional Gate Operation Using Superconducting Charge Qubits, Nature **425**, 941–944 (2003).

[2] R. McDermott, R. W. Simmonds, M. Steffen, K. B. Cooper, K. Cicak, K. D. Osborn, S. Oh, D. P. Pappas, and J. M. Martinis, Simultaneous State Measurement of Coupled Josephson Phase Qubits, Science **307**, 1299–1302 (2005).

[3] J. Majer, J. M. Chow, J. M. Gambetta, J. Koch, B. R. Johnson, J. A. Schreier, L. Frunzio, D. I. Schuster, A. A. Houck, A. Wallraff, A. Blais, M. H. Devoret, S. M. Girvin, and R. J. Schoelkopf, Coupling superconducting qubits via a cavity bus, Nature **449**, 443–447 (2007).

[4] M. A. Sillanpää, J. I. Park, and W. Simmonds, Coherent quantum state storage and transfer between two phase qubits via a resonant cavity, Nature **449**, 438–442 (2007).

[5] J. B. Majer, F. G. Paauw, A. C. J. ter Haar, C. J. P. M. Harmans, and J. E. Mooij, Spectroscopy on Two Coupled Superconducting Flux Qubits, Phys. Rev. Lett. **94**, 090501 (2005).

[6] A. O. Niskanen, K. Harrabi, F. Yoshihara, Y. Nakamura, S. Lloyd, and J. S. Tsai, Quantum Coherent Tunable Coupling of Superconducting Qubits, Science **316**, 723–726 (2007).

[7] A. Maassen van den Brink, Hamiltonian for coupled flux qubits, Phys. Rev. B **71**, 064503 (2005).

[8] W. J. Duffin, *Electricity and Magnetism*, McGraw-Hill, 4th edition, 1990.

[9] T. P. Orlando and K. A. Delin, *Foundations of Applied Superconductivity*, Addison-Wesley Publishing Company, 1991.

[10] M. A. Nielsen and I. L. Chuang, *Quantum Computation and Quantum Information*, Cambridge University Press, 2000.

[11] F. G. Paauw, A. Fedorov, C. J. P. M. Harmans, and J. E. Mooij, Tuning the Gap of a Superconducting Flux Qubit, Phys. Rev. Lett. **102**, 090501 (2009).

Chapter 4

Controlled-NOT gates on coupled flux qubits

Quantum computation requires quantum logic gates that use the interaction within pairs of quantum bits (qubits) to perform conditional operations [1]. Superconducting qubits may offer an attractive route towards scalable quantum computing. In previous experiments on coupled superconducting qubits, conditional gate behaviour [2] and entanglement [3] were demonstrated. Here we demonstrate selective execution of the complete set of four different controlled-NOT (CNOT) quantumlogic gates, by applying microwave pulses of appropriate frequency to a single pair of coupled flux qubits. All two-qubit computational basis states and their superpositions are used as input, while two independent single-shot SQUID detectors measure the output state, including qubit-qubit correlations. We determined the gate's truth table by directly measuring the state transfer amplitudes and by acquiring the relevant quantum phase shift using a Ramsey-like interference experiment. The four conditional gates result from the symmetry of the qubits in the pair: either qubit can assume the role of control or target, and the gate action can be conditioned on either the 0-state or the 1-state. These gates are now sufficiently characterized to be used in quantum algorithms, and together form an efficient set of versatile building blocks.

4.1 Introduction

In order to use superconducting circuits in quantum computing implementations, it is necessary to find a way to implement efficient quantum logic gates on pairs of qubits. Single superconducting qubits can be designed to operate in the charge [4], charge-phase [5], flux [6] and phase [7] regimes. In our experiments, we use a flux qubit consisting of a superconducting loop interrupted by three Josephson junctions, which can behave as a quantum two-level system [8]. Varying the magnetic flux threading the loop controls the energy level separation. At exactly half a flux quantum, the two classical states carrying a clockwise and an anticlockwise persistent current are degenerate. Quantum mechanical level repulsion occurs, and the eigenstates are formed by a symmetric and an antisymmetric superposition of the classical current states. When moving away from the degeneracy point, the eigenstates approach the classical current states and produce a net magnetic field. The qubit state is manipulated using microwave pulses resonant with the level separation; the circulating currents are used to detect the state with a superconducting quantum interference device (SQUID) magnetometer (see also Chapters 2 and 3.)

4.2 Experimental Setup

Previously, in experiments on two interacting superconducting qubits, spectroscopy was demonstrated [10, 11, 12, 13] as well as coherent qubit- qubit interaction controlled by non-adiabatic bias shifts [2, 3, 14, 15]. In our experiments, we couple two flux qubits magnetically with a fixed strength, resulting in a four-level system that is tunable with the individual flux biases. Four different two-qubit operations are realized with simple microwave pulses. The sample is depicted in Fig. 4.1. The qubit pair is described by the Hamiltonian

$$H = H_1 + H_2 + H_{12} = -\frac{1}{2}\left(\varepsilon_1\sigma_z^1 + \Delta_1\sigma_x^1 + \varepsilon_2\sigma_z^2 + \Delta_2\sigma_x^2\right) + J\sigma_z^1\sigma_z^2 \quad (4.1)$$

where $\varepsilon_i = -2I_{p,i}(\Phi_i - \Phi_0/2)$ represent the magnetic energy biases with $I_{p,i}$ the persistent currents, Φ_i the fluxes threading the loops and Φ_0 the superconducting flux quantum, Δ_i determine the coupling between the two classical current states of the single qubits, J is the qubit-qubit coupling energy and $\sigma_{x,y,z}^i$ are the Pauli spin matrices. To use the flux coupling effectively, the qubits are operated far from their degeneracy points, that is $\varepsilon_i > \Delta_i$, so the qubit energy separations are $\nu_i = \sqrt{\varepsilon_i^2 + \Delta_i^2} \approx \varepsilon_i$. As shown in Fig. 4.2a, this results in four resonance frequencies that change the state of either the first or second qubit. By way of the state-dependent circulating current, one qubit shifts the other's resonance frequency and vice versa. Consequently, all transitions are all either 0-controlled

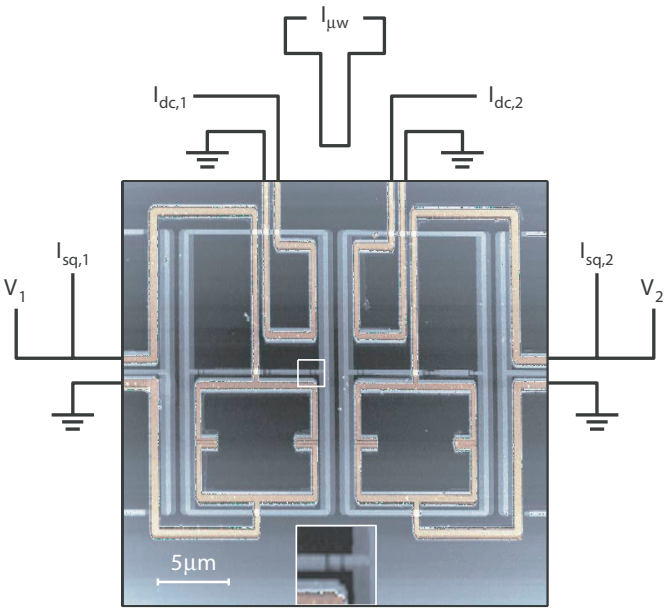

Figure 4.1: Coupled-qubits set-up. Atomic force micrograph of the sample, showing the two '8'-shaped flux qubits in light grey. These are a gradiometric variety of the common three-junction flux qubit, using a trapped supercurrent in the outer uninterrupted loop to bias the qubit at its degeneracy point [9]. The three Josephson junctions defining the qubit are visible on the middle horizontal branches; a single junction (white box) is shown magnified in the inset. The qubits are fabricated with electron beam lithography and two-angle shadow evaporation of aluminium. Two junctions are characterized by the ratio of Josephson to charging energy, $E_J/E_C = 36$; the relative area of the third is taken to be $\alpha = 0.75$. The persistent currents $I_{p,i}$ and energy gaps Δ_i are 450 nA and $h \times 2.6$ GHz for the first qubit, and 480 nA and $h \times 2.2$ GHz for the second. In the presented experiments, the first qubit is chosen to act as control (C) and the second as target (T). The coupling strength $2J = h \times 400$ MHz. On top of the qubits, two SQUIDs (shown in orange), used as switching qubit-state detectors, are fabricated in a separate lithography step. They are electrically isolated from the qubits, and operated by carefully-timed sample-and-hold (5 ns and 250 ns) d.c. pulses from current sources $I_{sq,1}$ and $I_{sq,2}$ ([6]). The resulting voltages V_1 and V_2, which depend on the qubit state, are detected using amplifiers and threshold detectors. Currents $I_{dc,1}$ and $I_{dc,2}$ bias the qubits through two small coils (shown in orange); in the experiments the energy level separations are $\nu_C = 7$ GHz and $\nu_T = 5$ GHz, applying currents $I_{dc,i} \approx 10$ μA. Here the characteristic times are $T_1 = 50 - 100$ ns, $T_{2,free} \approx 5$ns and $T_{2,Rabi} = 15 - 20$ ns. Qubit transitions are induced magnetically using an on-chip wire connected to a 50Ω microwave source, $I_{\mu w}$. The experiments are performed in a dilution refrigerator at $T < 50$ mK, with all current and voltage connections carefully filtered and/or attenuated.

or 1-controlled operations, with 0 and 1 representing the state of the second qubit. Given the symmetry of the qubits in the pair, we are free to select either one to act as the control (C) qubit and the other as the target (T) qubit, thereby defining the computational basis 0_C0_T , 0_C1_T, 1_C0_T, 1_C1_T.

4.3 Controlled-NOT gate by resonant driving

A resonant microwave pulse induces rotations of the states, and its microwave phase determines the orientation of the rotation axis (see Section 3.3). The pulse induces a quantum gate, which is characterized by a transfer matrix relating input to output states, both in amplitude and phase. For example, a microwave pulse inducing a rotation around the x-axis of the $1_C0_T - 1_C1_T$ transition (and thus off-resonant with respect to the $0_C0_T - 0_C1_T$ transition) is expressed by the gate matrix:

$$\hat{R}_{1_C0_T-1_C1_T}(\omega,\tau) = \begin{pmatrix} 1 & 0 & 0 & 0 \\ 0 & 1 & 0 & 0 \\ 0 & 0 & \cos\frac{\omega\tau}{2} & i\sin\frac{\omega\tau}{2} \\ 0 & 0 & i\sin\frac{\omega\tau}{2} & \cos\frac{\omega\tau}{2} \end{pmatrix} \tag{4.2}$$

where τ is the pulse length and ω is the Rabi frequency. This conditional rotation performs the ideal CNOT gate if $\omega\tau = \pi$, up to a single-qubit quantum phase shift. Here we only show measurements for this 1_C-controlled excitation of the target qubit, corresponding to the usual CNOT gate, and 0_C-controlled excitation of the target qubit. Similar results were obtained when control and target qubits were interchanged, yielding the four transitions of different frequency. Note that with this scheme one can conveniently produce the four maximally entangled two-particle Bell states, by applying two consecutive microwave pulses. Comparable techniques have been used in nuclear magnetic resonance experiments [16].

In Fig. 4.2d the microwave pulse scheme of the presented experiments is shown. The system is initialized by allowing it to relax to the ground state 0_C0_T, after which the desired input state is prepared. Now a two-qubit conditional gate is executed using a pulse selective to either a 0- or 1-controlled transition. Next, probe pulses can be applied to analyse the resulting density matrix. Finally, the states of the two qubits are determined simultaneously and independently using the two single-shot state detectors. Repeating this scheme N times, the result is represented by the state counts $N00$, $N01$, $N10$ and $N11$, directly yielding the measured joint-probabilities P_{00}, P_{01}, P_{10} and P_{11}. In addition to the individual switching probabilities of the control and target qubit detectors, $P_C = P_{10} + P_{11}$ and $P_T = P_{01} + P_{11}$, this method extracts correlation information, $P_{C=T} = P_{00} + P_{11}$.

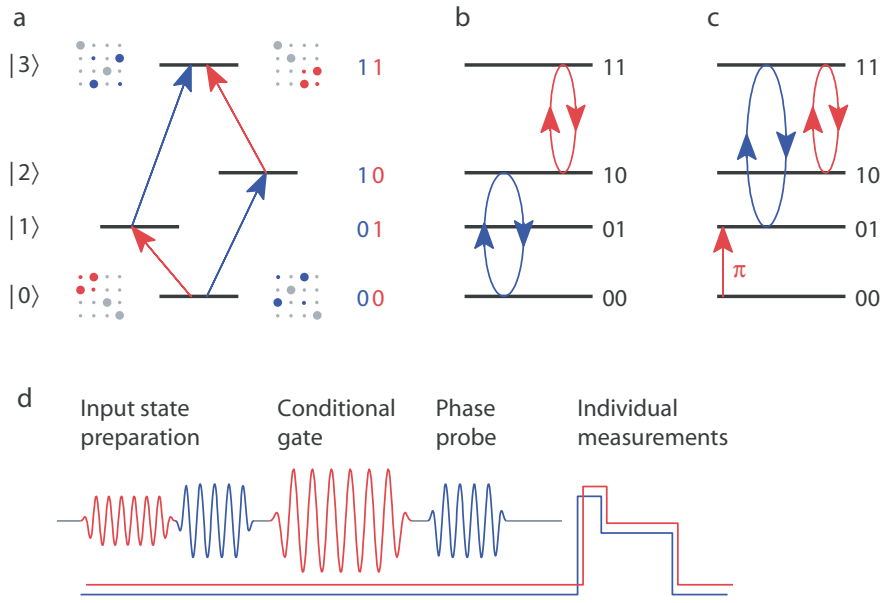

Figure 4.2: Operation of the coupled-qubits device. a, Energy level diagram of the two-qubit system. The qubit transitions are indicated by blue and red arrows, and the corresponding rotation matrices are depicted schematically with the computational basis increasing from left to right and from top to bottom. b, Sequence of operations to determine the truth table amplitudes for superpositions of the 0_C0_T and 1_C0_T input states. c, As b but for superpositions of the 0_C1_T and 1_C1_T input states. The π pulse initializes the target qubit in the state 1_T. d, General pulse sequence, displaying the applied microwave pulses and detector readout pulses.

To determine the output amplitudes of the CNOT gate for input superpositions of 0_C0_T and 1_C0_T, the pulse sequence depicted in Fig. 4.2b is used. After its creation, this state is subjected to the gate pulse resonant with the $1_C0_T - 1_C0_T$ transition. In Fig. 4.3a, the switching probability of the control qubit detector shows the superposition created by the first pulse. Fig. 4.3c shows that when the 1_C-controlled gate pulse induces an odd number of π rotations it executes a CNOT gate, inverting the target qubit state only if the control qubit was in the state 1_C; for the 0_C state the gate pulse is off-resonant, leaving the target qubit unaffected. Similarly, Fig. 4.2c illustrates the pulse sequence used to determine the matrix amplitudes for input superpositions of 0_C1_T and 1_C1_T. First, the target qubit is initialized in the 1_T state by inducing a π rotation on the $0_C0_T - 0_C1_T$ transition. The control qubit is then brought into a superposition by driving the $0_C1_T - 1_C1_T$ transition, as depicted in Fig. 4.3b. Finally, the CNOT gate is executed with the identical microwave gate pulse as used previously for the $0_C0_T - 1_C0_T$ superposition input states. Fig. 4.3d shows that the gate only inverts the target qubit back to the state 0_T if the control qubit was in the state 1_C.

Figure 4.4 shows the results for the same experiment described above, now for both the 0_C- and 1_C-controlled gate operations, and over a wider range of pulse durations. For Fig. 4.4(c,d) the 0_C-controlled transition and for Fig. 4.4(a,b) the 1_C-controlled transition was induced. Fig. 4.4a and Fig. 4.4b show the switching probabilities of the control qubit detector, depicting the superposition created by the first pulse. Comparing Fig. 4.4b and Fig. 4.4d shows that the 0_C- and 1_C-controlled transitions are complementary, only one of the two can be excited depending on the control qubit state.

The truth table amplitudes follow directly from the joint probabilities. In Fig. 4.5a the output state counts are depicted for the prepared computational basis input states. The measured data qualitatively agree with the amplitude matrix of an ideal CNOT gate:

$$M_{\mathrm{CNOT}} = \begin{pmatrix} 1 & 0 & 0 & 0 \\ 0 & 1 & 0 & 0 \\ 0 & 0 & 0 & 1 \\ 0 & 0 & 1 & 0 \end{pmatrix} \tag{4.3}$$

The input states 0_C0_T and 0_C1_T remain unaffected by the gate and translate directly to the same output state, hence the two high values on the diagonal of the matrix. For the states 1_C0_T and 1_C1_T, the gate inverts the target qubit, explaining the two high off-diagonal values. Fig. 4.5a can be related to Fig. 4.3 by considering the points at the intersections of the dotted lines of the latter. Note that the states 0_C and 1_C correspond to the elements from Fig. 4.3 where a 2π and 3π rotation, respectively, were induced, which explains the comparable

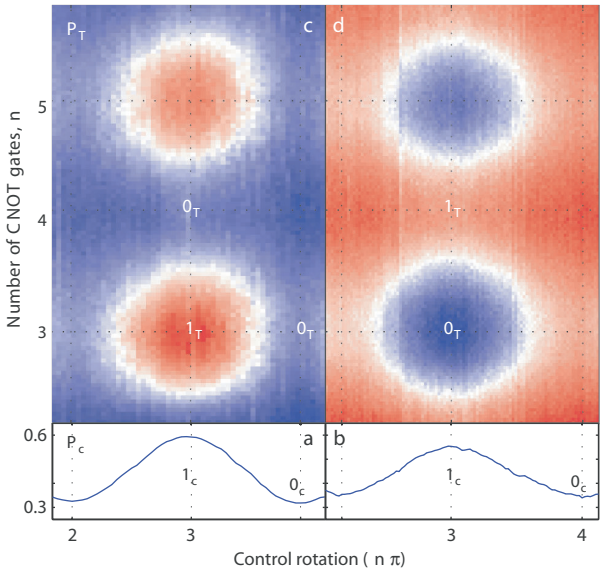

Figure 4.3: 1C-controlled gate operation. The horizontal axis represents the control qubit rotation, and the ordinate of the colour figures sets the number of CNOT gates (n) that was executed. The pulses needed for control and gate rotations significantly smaller than π were too short to generate reliably. a, b, Control qubit input state preparation, where P_C represents the measured switching probability of the control qubit detector. A 2π rotation corresponds to a pulse length of 5 ns. c, d, Target qubit state after the CNOT pulse, where P_T represents the measured switching probability of the target qubit detector, ranging from 0.3 (blue) through 0.5 (white) to 0.7 (red). A single CNOT π rotation corresponds to a 3 ns pulse. a, c, Results for superpositions of the 0_C0_T and 1_C0_T input states, corresponding to the experimental scheme of Fig. 4.2b. b, d, Results for superpositions of the 0_C1_T and 1_C1_T input states, corresponding to the experimental scheme of Fig. 4.2c.

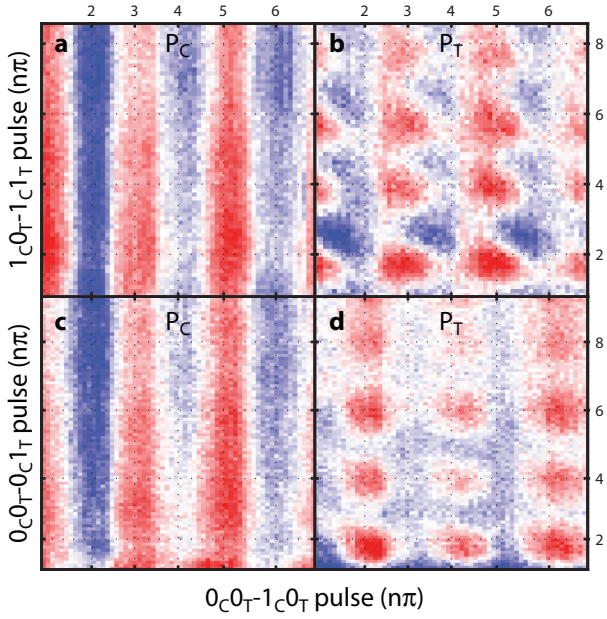

Figure 4.4: 0_C- and 1_C-controlled gate operations. The horizontal axes set the control qubit state and along the vertical axes of the colour figures the controlled gate pulse length is varied. a, c, Control qubit input state. b, d, Target qubit state after the gate pulse. a, b, Results for the $1_C0_T - 1_C1_T$ transition. b, d, Results for the $0_C0_T - 0_C1_T$ transition.

input state fidelities.

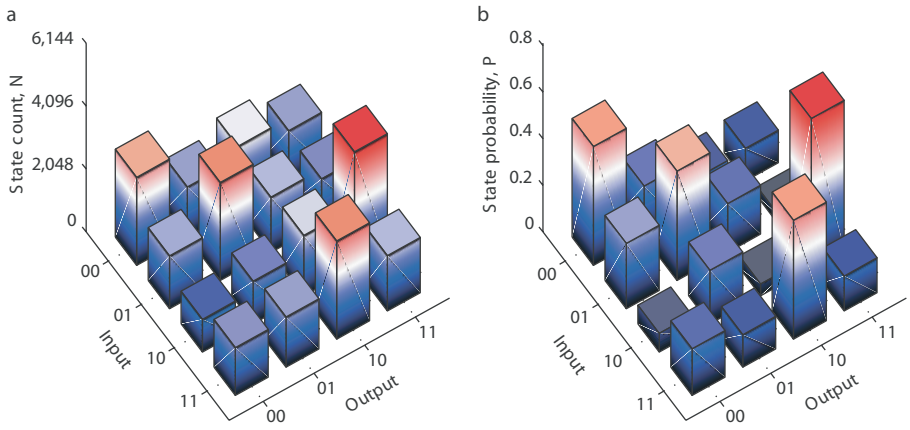

Figure 4.5: Truth table amplitudes of the CNOT quantum gate. a, State counts (N_{00}, N_{01}, N_{10} and N_{11}) of the detectors after $n = 3$ CNOT rotations, for 8,192 single-shot measurements. b, Truth table amplitudes corrected for measurement visibility using conditional spectroscopy measurements. The average gate fidelity equals $F = 0.4$.

The major factors contributing to the deviations of Fig. 4.5a from the ideal transfer-matrix M_{CNOT} are qubit decoherence, control errors and measurement visibility. The last is only 40% for this sample; note that more advanced SQUID detection methods have approached 90% visibility [17]. To compensate for this influence, we performed conditional spectroscopy measurements [18] that convert the normalized detector counts P_{ij} to qubit state occupation probabilities. For an ideal single-shot detector, these two sets are identical. As explained below in section 4.4, conditional spectroscopy provides two detection mechanisms in parallel for the control qubit: one using the control qubit detector directly and a second using the excitation spectrum of the target qubit. The latter is now used as a means to calibrate the former, in this way compensating for the effect of the limited measurement visibility. Using this technique, the CNOT data of Fig. 4.5a are corrected, and the result is depicted in Fig. 4.5b. Note that the influences of decoherence and control errors are preserved. We quantify the resulting average of the logical basis amplitude fidelities by $F = \mathrm{Tr}(M_{\mathrm{exp}} M_{\mathrm{CNOT}}^{\mathrm{T}})/4$, with $F = 1$ for the ideal case. The experimental data from Fig. 4.5b can be represented by

the matrix M_{exp}:

$$M_{\mathrm{exp}} = \begin{pmatrix} 0.51 & 0.22 & 0.13 & 0.14 \\ 0.28 & 0.47 & 0.21 & 0.04 \\ 0.08 & 0.23 & 0.05 & 0.64 \\ 0.20 & 0.14 & 0.51 & 0.15 \end{pmatrix} \tag{4.4}$$

resulting in $F = 0.4$. The significant reduction of F is mostly due to the short coherence time of this particular sample. We expect to increase this number to gate performances similar to that of simple microwave-driven Rabi experiments [6, 17].

4.4 Conditional spectroscopy for detector visibility calibration

The measured detector state counts N_{00}, N_{01}, N_{10} and N_{11}, presented in Fig. 4.5a, and their associated probabilities can be corrected for the limited detection visibility using a conditional spectroscopy experiment. In this experiment we scan the spectrum of the target qubit using its own detector output P_T. This spectrum is modified by the control qubit state, since the control shifts the target's resonance frequency. This state detection mechanism for the control qubit supplements the direct state detector output P_C and can be used as a calibration of the latter to obtain the qubit state probability. Figure 4.6 shows the results. A Rabi oscillation of the resonantly driven control qubit is shown, in dependence of the microwave pulse duration. The three insets show the target qubit spectrum (which is measured simultaneously with the control qubit detector) for different microwave pulse lengths. In inset a, the control qubit is in its ground state where the control detector switching probability $P_C = 0.45$ and the target qubit spectrum only shows a resonance at $f = 5.2$ GHz. Inducing a π rotation on the control qubit to bring it to the 1_C-state, reduces the detector switching probability to $P_C = 0.28$ and reduces the target qubit resonance at $f = 5.2$ GHz, but creates a new resonance at $f = 5.6$ GHz (inset b). Rotating the control qubit back to its ground state (inset c) restores the direct switching probability P_C and the target qubit spectrum. The relative heights of the target qubit spectrum are now used to normalize the control detector switching probability, effectively yielding the control qubit state probability. Similarly, the target qubit detector is calibrated to represent the target qubit state probability by interchanging target and control.

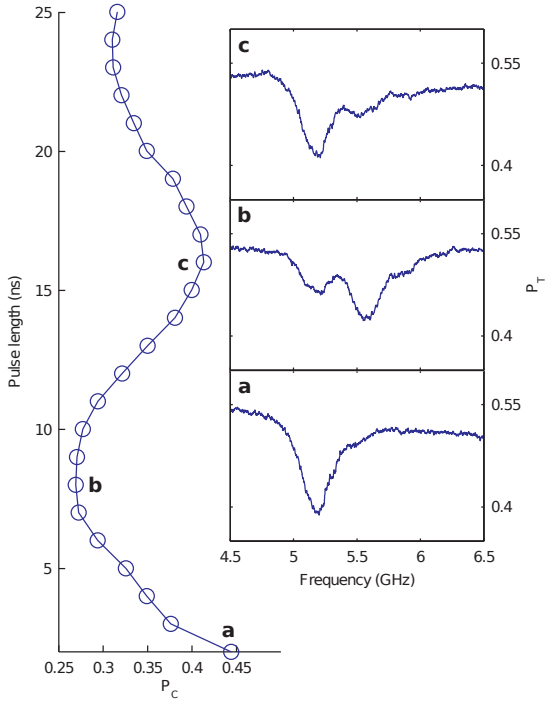

Figure 4.6: Controlled spectroscopy detector calibration. The main figure shows a Rabi oscillation of the control qubit, where the vertical axis sets the microwave pulse length and along the horizontal axis the control qubit detector switching probability is measured. a, b, c, Target qubit spectra at the corresponding points in the Rabi trace that are used as a calibration for the control qubit detector.

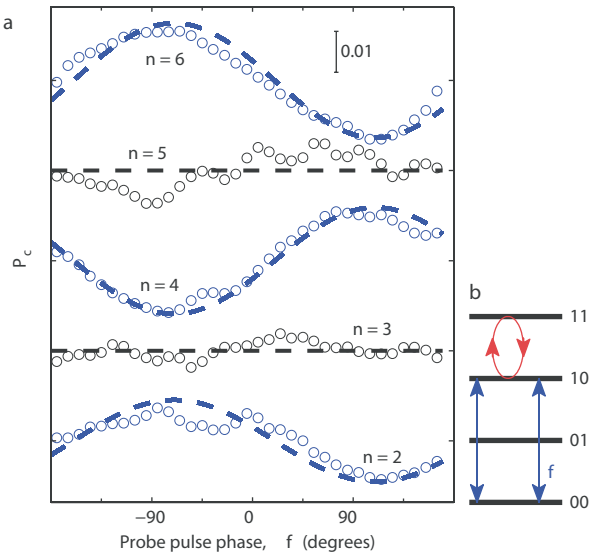

Figure 4.7: Quantum phase induced after $n = 2 - 6$ CNOT operations. a, Phase probing of the control qubit with the relative microwave phase of the second Ramsey $\pi/2$ pulse along the horizontal axis. After an odd number n of CNOT gates, the system population is in an entangled superposition of the states 0_C0_T and 1_C1_T (Bell state), extinguishing the Ramsey interference pattern. An even number of gates executes $n/2$ PHASE gates, and returns the system to a disentangled state, restoring the Ramsey signal. The 180° phase shift that occurs between even traces with $\Delta n = 2$ agrees with the description of driven Rabi evolution. b, The sequence of operations used to acquire the quantum phase shift of the CNOT gates.

4.5 Quantum phase induced by the CNOT gate

In order to use this gate in a quantum algorithm, the phase factors of the amplitudes of M_{exp} at the positions of non-zero elements of M_{CNOT} have to be determined. Using a Ramsey-like interference experiment on n consecutive CNOT gates, we show that these phase shifts agree with the driven Rabi evolution. Equation 4.2 predicts that for $n = 2$ CNOT gates (that is, $\omega\tau = 2\pi$) a PHASE gate is executed which inverts the phase of the states $1_{\mathrm{C}}0_{\mathrm{T}}$ and $1_{\mathrm{C}}1_{\mathrm{T}}$ relative to the states $0_{\mathrm{C}}0_{\mathrm{T}}$ and $0_{\mathrm{C}}1_{\mathrm{T}}$. The scheme used to measure this shift is depicted in Fig. 4.7b. First a $\pi/2$ pulse with a fixed microwave phase is applied, bringing the control qubit into an equal weight superposition of states 1_{C} and 1_{C}. Next the CNOT gates are executed. The states before and after the gates are then interfered by means of a second $\pi/2$ probe pulse, of which the microwave phase φ, corresponding to the rotation axis, is varied. In Fig. 4.7a the extra quantum phase between the states $0_{\mathrm{C}}0_{\mathrm{T}}$ and $1_{\mathrm{C}}0_{\mathrm{T}}$ is depicted. As expected, the Ramsey fringe is inverted by the quantum phase shift of 180° induced by a full Rabi cycle, thus executing a PHASE gate. Experimentally we find, in addition to the quantum phase, a second shift which is due to off-resonant effects of the CNOT microwave pulse on the control qubit transition. It is distinguished from the quantum phase by performing a second measurement with exactly the same pulse sequence with the target qubit detuned from any relevant frequency. In this case, the CNOT gate pulse only induces the off-resonant z-rotation of the control qubit. We find that this effect is nearly linear in driving power and it is compensated for in Fig. 4.7a, leaving only the genuine quantum phase shift.

4.6 Conclusions

In conclusion, we have implemented the complete set of four two-qubit CNOT gates in a symmetric pair of superconducting flux qubits. Complemented with longer coherence times [6, 17] and optimized detector visibility [17], the presented gates enable experiments on two-qubit quantum algorithms and solid-state qubit entanglement using the four Bell states. This scheme, combined with controllable coupling [13], can be used for the implementation of solid-state quantum computing.

Bibliography

[1] M. A. Nielsen and I. L. Chuang, *Quantum Computation and Quantum Information*, Cambridge University Press, 2000.

[2] T. Yamamoto, Y. A. Pashkin, O. Astafiev, Y. Nakamura, and J. S. Tsai, Demonstration of Conditional Gate Operation Using Superconducting Charge Qubits, Nature **425**, 941–944 (2003).

[3] M. Steffen, M. Ansmann, R. McDermott, N. Katz, R. C. Bialczak, E. Lucero, M. Neeley, E. M. Weig, A. N. Cleland, and J. M. Martinis, Measurement of the entanglement of two superconducting qubits via state tomography, Science **313**, 1423–1425 (2006).

[4] Y. Nakamura, Y. A. Pashkin, and J. S. Tsai, Coherent Control of Macroscopic Quantum States in a Single-Cooper-Pair Box, Nature **398**, 786–788 (1999).

[5] D. Vion, A. Aassime, A. Cottet, P. Joyez, H. Pothier, C. Urbina, D. Esteve, and M. H. Devoret, Manipulating the quantum state of an electrical circuit, Science **296**, 886–889 (2006).

[6] I. Chiorescu, Y. Nakamura, C. J. P. M. Harmans, and J. E. Mooij, Coherent Quantum Dynamics of a Superconducting Flux Qubit, Science **299**, 1869–1871 (2003).

[7] J. M. Martinis, S. Nam, J. Aumentado, and C. Urbina, Rabi oscillations in a large Josephson-junction quibt, Phys. Rev. Lett **89**, 117901 (2002).

[8] J. E. Mooij, T. P. Orlando, L. Levitov, L. Tian, C. H. van der Wal, and S. Lloyd, Josephson Persistent-Current Qubit, Science **285**, 1036–1039 (1999).

[9] J. B. Majer, J. R. Butcher, and J. E. Mooij, Simple phase bias for superconducting circuits, Appl. Phys. Lett. **80**, 3638–3640 (2002).

[10] A. J. Berkley, H. Xu, R. C. Ramos, M. A. Gubrud, F. W. Strauch, P. R. Johnson, J. R. Anderson, A. J. Dragt, C. J. Lobb, and F. C. Wellstood, Entangled macroscopic quantum states in two superconducting qubits, Science **300**, 1548–1550 (2003).

[11] J. B. Majer, F. G. Paauw, A. C. J. ter Haar, C. J. P. M. Harmans, and J. E. Mooij, Spectroscopy on Two Coupled Superconducting Flux Qubits, Phys. Rev. Lett. **94**, 090501 (2005).

[12] M. Grajcar, A. Izmalkov, S. H. W. van der Ploeg, S. Linzen, T. Plecenik, T. Wagner, U. Hübner, E. Il'ichev1, H.-G. Meyer, A. Y. Smirnov, P. J. Love, A. M. van den Brink, M. H. S. Amin, S. Uchaikin, , and A. M. Zagoskin, Four-qubit device with mixed couplings, Phys. Rev. Lett. **96**, 047006 (2006).

[13] T. Hime, P. A. Reichardt, B. L. T. Plourde, T. L. Robertson, C.-E. Wu, A. V. Ustinov, and J. Clarke, Solid-state qubits with current-controlled coupling, Science **314**, 1427–1429 (2006).

[14] Y. A. Pashkin, T. Yamamoto, O. Astafiev, Y. Nakamura, D. V. Averin, and J. S. Tsai, Quantum oscillations in two coupled charge qubits, Nature **421**, 823–826 (2003).

[15] R. McDermott, R. W. Simmonds, M. Steffen, K. B. Cooper, K. Cicak, K. D. Osborn, S. Oh, D. P. Pappas, and J. M. Martinis, Simultaneous State Measurement of Coupled Josephson Phase Qubits, Science **307**, 1299–1302 (2005).

[16] D. G. Cory, M. D. Price, and T. F. Havel, Nuclear magnetic resonance spectroscopy: An experimentally accessible paradigm for quantum computing, Physica D **120**, 82–101 (1998).

[17] A. Lupaşcu, S. Saito, T. Picot, P. C. de Groot, C. J. P. M. Harmans, and J. E. Mooij, Quantum non-demolition measurement of a superconducting two-level system, Nature Physics **3**, 119–125 (2007).

[18] A. C. J. ter Haar, *Single and coupled Josephson junction quantum bits*, Ph.d. thesis, Delft University of Technology, 2005.

Chapter 5

Selective darkening of degenerate transitions

Controlled manipulation of quantum states is central to studying natural and artificial quantum systems. If a quantum system consists of interacting sub-units, the nature of the coupling may lead to quantum levels with degenerate energy differences. This degeneracy makes frequency-selective quantum operations impossible. For the prominent group of transversely coupled two-level systems, i.e. qubits, we introduce a method to selectively suppress one transition of a degenerate pair while coherently exciting the other, effectively creating artificial selection rules. It requires driving two qubits simultaneously with the same frequency and specified relative amplitude and phase. We demonstrate our method on a pair of superconducting flux qubits [1]. It can directly be applied to the other superconducting qubits [2, 3, 4, 5, 6], and to any other qubit type that allows for individual driving. Our results provide a single-pulse controlled-NOT gate for the class of transversely coupled qubits.

5.1 Introduction

In coupling two qubits one can distinguish interactions that are oriented either along or perpendicular to the eigenstates of the qubits. While in both cases the resulting two-qubit energy level spectrum reflects the coupling strength, the response to a change of the state of a qubit differs greatly. With longitudinal coupling the state of one qubit affects the energy splitting of the other qubit. Although this spectroscopic shift enables simple resonant driving for all operations [7, 8], in practice it requires refocussing schemes to compensate for the continuously evolving phases [9]. In contrast, for transverse coupling the energy splitting of one qubit does not depend on the state of the other qubit. This latter case is appealing as in the absence of driving the system acts as a set of uncoupled qubits, and the coupling is effectively switched on when AC driving is applied [10]. The price to pay for the advantage of transverse coupling is obvious; the degeneracy prohibits schemes for selective excitation that rely on a frequency splitting. Previous experiments used either additional coupling elements [11], extra modes [12], or shifted levels into and out of resonance by DC [13] or strong AC fields [14, 15]. Note that level shifting can imply passing through conditions of low coherence [16], or passing resonances with other qubits. In contrast, our method works for simple direct coupling as well as for systems with additional coupling elements, such as harmonic oscillators, as long as the effective coupling is transverse. It uses only a single pulse of a single frequency and does not require (dynamical) shifting of the levels.

5.2 Method

We consider the class of systems of transversely coupled qubits, described with the Hamiltonian

$$H = -\frac{1}{2}\left(\Delta_1\sigma_z^1 + \Delta_2\sigma_z^2\right) + J\sigma_x^1\sigma_x^2, \tag{5.1}$$

where Δ_i is the single-qubit energy splitting of qubit i, J is the qubit-qubit coupling energy and $\sigma_{x,y,z}^i$ are the Pauli spin matrices. This Hamiltonian describes many actively used quantum systems [1, 2, 3, 4, 5, 6], and often applies for operation at a coherence sweet-spot [3, 17, 14, 18, 19]. The energy levels of this system are shown schematically in Fig. 5.1b. The arrows indicate the transitions of interest; the blue and red arrows describe the transitions of qubit 1 and 2, respectively. Both pairs are degenerate in frequency, which is typical for transverse coupling. For simplicity, we label the states as if the qubits were uncoupled, although the single-qubit states are mixed by the coupling. This state mixing is central to the method we introduce here. As for all schemes with fixed coupling,

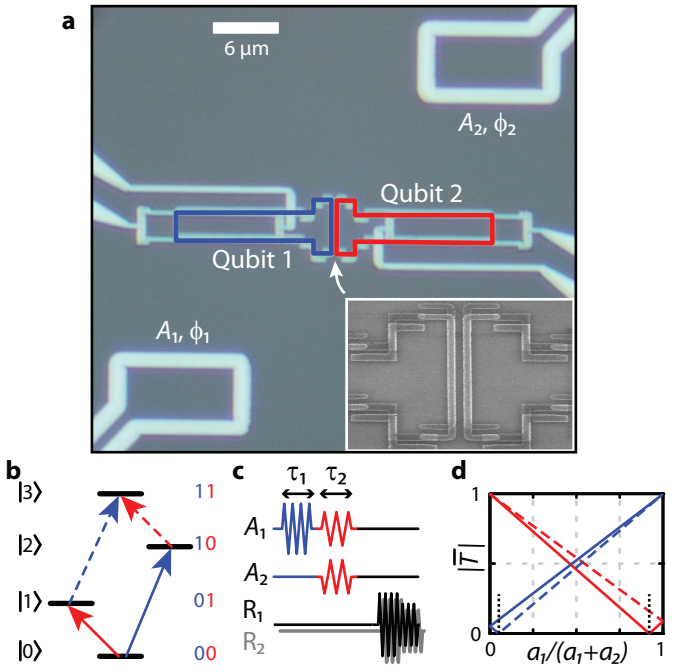

Figure 5.1: Coupled qubit system and transitions. **a**, Optical micrograph of the sample, showing two flux qubits colored in blue and red. The inset shows part of each qubit loop, both containing four Josephson tunnel junctions. Overlapping the qubit loops, in light-grey, are the SQUID-based qubit-state detectors. In the top right and bottom left are the two antennas from which the qubits are driven. **b**, Energy level diagram of the coupled qubit system. Arrows of the same color indicate transitions of the same qubit and are degenerate in frequency. **c**, Pulse sequence used for the coherent excitation of the qubits. The first pulse is resonant with qubit 1. The second pulse, applied from both antennas simultaneously with independent amplitudes and phases, is resonant with qubit 2. After the second pulse the state of both qubits is read out. **d**, The normalized transition strengths of the four transitions in **b** as a function of the net driving amplitudes $a_1/(a_1+a_2)$ for $\varphi_2-\varphi_1=0$. For $\varphi_2-\varphi_1=\pi$ the dashed and solid lines are interchanged. The black dotted lines indicate the locations of the darkened transitions.

the mixing can additionally lead to a difference between the operational basis and the readout basis. Solutions to this problem depend on the details of the readout scheme. For flux qubits, the readout naturally involves shifting the qubits to a bias position where the problem does not exist.

Our method aims at the selective excitation of a transition of one of the degenerate pairs and is based on simultaneously driving both qubits with the resonance frequency of that pair, employing different amplitudes and phases. The driving is described with the Hamiltonian

$$H_{\mathrm{drive}} = \; a_1 \cos(\omega t + \varphi_1)\sigma_x^1 + a_2 \cos(\omega t + \varphi_2)\sigma_x^2, \tag{5.2}$$

where ω is the driving frequency, and a_i and φ_i are the driving amplitude and phase for qubit i. The transition strength $T_{k\leftrightarrow l} = \langle l|\tilde{H}_{\mathrm{drive}}|k\rangle$, with the driving Hamiltonian transformed to an appropriate rotating frame (see Section 5.3), governs the transition rate and depends on both a_i and φ_i. Figure 5.1d shows the normalized $|\overline{T}| = |T|/(a_1 + a_2)$ as a function of $a_1/(a_1 + a_2)$, for a fixed phase difference $\varphi_2 - \varphi_1 = 0$. Clearly the two transitions of each qubit generally do *not* have the same strength T, despite their frequency degeneracy. In addition, for certain settings individual transitions are completely suppressed: the transition is darkened (black dotted lines in Fig. 5.1d). The darkened transitions provide the desired conditions where one of the two transitions can be excited individually, even though the driving field is resonant with both transitions. The difference in transition strength can be understood intuitively. As coupling leads to mixing of the single-qubit eigenstates, qubit 2 can be excited by driving qubit 1 with a frequency that is resonant with qubit 2. This indirect driving can enhance, counteract and even cancel direct driving of qubit 2. The effect differs for the two degenerate transitions, because the states involved are different superpositions of the single-qubit eigenstates (see Section 5.3). For $J \ll |\Delta_1 - \Delta_2|$, and assuming $\Delta_1 > \Delta_2$, one readily finds the driving amplitude ratio

$$\frac{a_2}{a_1} = \frac{J}{\Delta_1 - \Delta_2}, \tag{5.3}$$

which yields $T_{00\leftrightarrow 01} = 0$ for $\varphi_2 - \varphi_1 = 0$ and $T_{10\leftrightarrow 11} = 0$ for $\varphi_2 - \varphi_1 = \pi$. These are the transitions of qubit 2. For the transitions of qubit 1, i.e. $00 \leftrightarrow 10$ and $01 \leftrightarrow 11$, the amplitude ratio is simply inverted. The derivation of Eq. 5.3 and expressions for arbitrary J are given in the following section. Note that for a darkened transition in one qubit, the other is driven more strongly. This non-resonant driving of the other qubit limits the maximum operation frequency. From the usual condition that the transition strength of the unwanted transition should be smaller than its frequency detuning one can derive the maximum operation frequency $4J/h$, which is essentially as fast as any other two-qubit operation.

5.3 Conditions for darkened transition

In this section we derive the driving conditions to obtain a darkened transition. Let us take the Hamiltonian:

$$H = -\frac{1}{2}\left(\Delta_1\sigma_z^1 + \Delta_2\sigma_z^2\right) + J\sigma_x^1\sigma_x^2. \tag{5.4}$$

Without loss of generality we take $\Delta_1 \geq \Delta_2$. Additionally we have the driving term:

$$\begin{aligned} H_{\text{drive}} &= a_1\cos(\omega t+\varphi_1)\sigma_x^1 + a_2\cos(\omega t+\varphi_2)\sigma_x^2 && (5.5a)\\ &= \tilde{H}^+_{\text{drive}}e^{i\omega t} + \tilde{H}^-_{\text{drive}}e^{-i\omega t} && (5.5b)\end{aligned}$$

where

$$\tilde{H}^{\pm}_{\text{drive}} = \frac{a_1}{2}e^{\pm i\varphi_1}\sigma_x^1 + \frac{a_2}{2}e^{\pm i\varphi_2}\sigma_x^2. \tag{5.6}$$

The Hamiltonian (Eq. 5.4) can be diagonalized without any approximations:

$$\begin{aligned} |0\rangle &= \cos\theta_1|00\rangle - \sin\theta_1|11\rangle && (5.7a)\\ |1\rangle &= \cos\theta_2|01\rangle - \sin\theta_2|10\rangle && (5.7b)\\ |2\rangle &= \cos\theta_2|10\rangle + \sin\theta_2|01\rangle && (5.7c)\\ |3\rangle &= \cos\theta_1|11\rangle + \sin\theta_1|00\rangle, && (5.7d)\end{aligned}$$

where

$$\begin{aligned} \tan 2\theta_1 &= \frac{2J}{\Delta_1+\Delta_2} && (5.8a)\\ \tan 2\theta_2 &= \frac{2J}{\Delta_1-\Delta_2}. && (5.8b)\end{aligned}$$

To calculate the transition strength $T_{k\leftrightarrow l} = \langle l|\tilde{H}_{\text{drive}}|k\rangle$, we ignore the counter-rotating fields, which results in $\tilde{H}_{\text{drive}} = \tilde{H}^+_{\text{drive}}$ for $k < l$ and $\tilde{H}_{\text{drive}} = \tilde{H}^-_{\text{drive}}$ for $k > l$. We find that

$$\begin{aligned} \langle 1|\tilde{H}_{\text{drive}}|0\rangle &= -\frac{a_1}{2}e^{i\varphi_1}\left\{\cos\theta_1\sin\theta_2 + \sin\theta_1\cos\theta_2\right\}\\ &\quad +\frac{a_2}{2}e^{i\varphi_2}\left\{\cos\theta_1\cos\theta_2 + \sin\theta_1\sin\theta_2\right\}\\ &= -\frac{a_1}{2}e^{i\varphi_1}\sin(\theta_1+\theta_2) + \frac{a_2}{2}e^{i\varphi_2}\cos(\theta_2-\theta_1) && (5.9)\\ \langle 3|\tilde{H}_{\text{drive}}|2\rangle &= +\frac{a_1}{2}e^{i\varphi_1}\sin(\theta_1+\theta_2) + \frac{a_2}{2}e^{i\varphi_2}\cos(\theta_2-\theta_1), && (5.10)\end{aligned}$$

and

$$\begin{aligned}\langle 2|\tilde{H}_{\rm drive}|0\rangle &= \frac{a_1}{2}e^{i\varphi_1}\{\cos\theta_1\cos\theta_2-\sin\theta_1\sin\theta_2\}\\ &\quad+\frac{a_2}{2}e^{i\varphi_2}\{\cos\theta_1\sin\theta_2-\sin\theta_1\cos\theta_2\}\\ &= \frac{a_1}{2}e^{i\varphi_1}\cos(\theta_1+\theta_2)+\frac{a_2}{2}e^{i\varphi_2}\sin(\theta_2-\theta_1) \qquad (5.11)\\ \langle 3|\tilde{H}_{\rm drive}|1\rangle &= \frac{a_1}{2}e^{i\varphi_1}\cos(\theta_1+\theta_2)-\frac{a_2}{2}e^{i\varphi_2}\sin(\theta_2-\theta_1). \qquad (5.12)\end{aligned}$$

We therefore find that the required ratio of driving amplitudes to drive only one of the two transitions of qubit 2 is given by

$$\frac{a_2}{a_1}=\frac{\sin(\theta_1+\theta_2)}{\cos(\theta_2-\theta_1)}, \qquad (5.13)$$

with $\varphi_2-\varphi_1=0$ for suppressing the $00\leftrightarrow 01$ transition, and $\varphi_2-\varphi_1=\pi$ for suppressing the $10\leftrightarrow 11$ transition. For driving the transitions of qubit 1, the ratio is

$$\frac{a_2}{a_1}=\frac{\cos(\theta_1+\theta_2)}{\sin(\theta_2-\theta_1)}, \qquad (5.14)$$

with $\varphi_2-\varphi_1=\pi$ for suppressing the $00\leftrightarrow 10$ transition, and $\varphi_2-\varphi_1=0$ for suppressing the $01\leftrightarrow 11$ transition.

The resonance frequencies are given by:

$$E_1-E_0=E_3-E_2=\frac{1}{2}\left(\sqrt{4J^2+(\Delta_1+\Delta_2)^2}-\sqrt{4J^2+(\Delta_1-\Delta_2)^2}\right) \qquad (5.15a)$$

$$E_2-E_0=E_3-E_1=\frac{1}{2}\left(\sqrt{4J^2+(\Delta_1+\Delta_2)^2}+\sqrt{4J^2+(\Delta_1-\Delta_2)^2}\right). \qquad (5.15b)$$

If we now make the assumption that $J\ll|\Delta_1-\Delta_2|$, then to lowest order approximation $\theta_1=0$ and $\theta_2=J/|\Delta_1-\Delta_2|$. The eigenvectors reduce to

$$\begin{aligned}|0\rangle &= |00\rangle \qquad (5.16a)\\ |1\rangle &= |01\rangle-\frac{J}{\Delta_1-\Delta_2}|10\rangle \qquad (5.16b)\\ |2\rangle &= |10\rangle+\frac{J}{\Delta_1-\Delta_2}|01\rangle \qquad (5.16c)\\ |3\rangle &= |11\rangle, \qquad (5.16d)\end{aligned}$$

and $E_1-E_0=E_3-E_2=\Delta_2$, $E_2-E_0=E_3-E_1=\Delta_1$. Following the same procedure as above we find for the darkened transitions

$$\frac{a_1}{a_2}=\frac{J}{\Delta_1-\Delta_2} \qquad (5.17)$$

and

$$\frac{a_2}{a_1} = \frac{J}{\Delta_1 - \Delta_2} \tag{5.18}$$

for suppressing the transitions of qubit 1 and 2, respectively. The phase conditions are the same as above.

5.4 Experimental Setup

To experimentally demonstrate this method we employ two coupled flux qubits [1], each consisting of a superconducting loop interrupted by four Josephson tunnel junctions. When biased with a magnetic flux close to half a flux quantum Φ_0, the two states of each qubit are clockwise and anti-clockwise persistent-current states. These currents I_p produce opposite magnetic fields, which provides the coupling for the two qubits. Two independent AC-operated SQUID magnetometers are used to simultaneously read out the states of the qubits [20, 21]. These are switching-type detectors, where the switching probability P_{sw} is a measure for the magnetic field. At a bias of $\frac{\Phi_0}{2}$ the system is described by the Hamiltonian of Eq. 5.1. Here the eigenstates of each qubit are symmetric and anti-symmetric superpositions of the two persistent-current states, with level separation Δ. The device is depicted in Fig. 5.1a. The qubits are characterised by the persistent currents $I_{p,1} = 355$ nA and $I_{p,2} = 460$ nA and the energy splittings $\Delta_1/h = 7.88$ GHz and $\Delta_2/h = 4.89$ GHz. The qubit-qubit coupling strength is $2J/h = 410$ MHz.

For our fabricated quantum objects the spatial locations are well-defined, and the individual control of amplitude and phase for each qubit according to Eq. 5.2 can be easily achieved using local magnetic fields. We employ two on-chip antennas, indicated as A_1 and A_2 in Fig. 5.1a, both coupling to both qubits, with a stronger coupling to the closer one. Driving the two qubits from both antennas is described with

$$\begin{aligned} H_{\text{drive}} = \; & A_1 \cos(\omega t + \phi_1)(m_{11}\sigma_x^1 + m_{12}\sigma_x^2) \\ & + A_2 \cos(\omega t + \phi_2)(m_{21}\sigma_x^1 + m_{22}\sigma_x^2), \end{aligned} \tag{5.19}$$

where A_j and ϕ_j are the driving amplitude and phase for antenna j and m_{ji} is the coupling of antenna j to qubit i. Note that *any* combination of a_i and φ_i in Eq. 5.2 can be achieved with the proper choice of A_j and ϕ_j. For this device $m_{12}/m_{11} = 0.32$, $m_{21}/m_{22} = 0.33$ and $m_{11} = m_{22}$.

5.5 Experiment 1: Double Rabi-frequency for driving a degenerate transition

For the experimental demonstration we choose to focus on the degenerate transitions of qubit 2. We first show that, if the qubits are driven from a *single antenna*, the two degenerate transitions exhibit a different Rabi frequency. We apply two pulses on antenna 1: the first pulse is resonant with qubit 1, the second pulse is resonant with qubit 2. Figure 5.1c shows a schematic of the pulse-sequence; note that here $A_2 = 0$. The experiment is repeated for varying durations τ_1 and τ_2 of pulses 1 and 2. The switching probability $P_{sw,1}$ of detector 1 is depicted in Fig. 5.2a, showing a few Rabi oscillation periods as a function of the pulse duration τ_1. Varying τ_2 does not lead to oscillations of qubit 1, as pulse 2 is non-resonant, and only relaxation is observed. The oscillations of qubit 2, induced by the second pulse, are visible in $P_{sw,2}$ (Fig. 5.2b). Here we distinguish two oscillation frequencies. Along the white solid line, where qubit 1 is prepared in the excited state, qubit 2 oscillates with a Rabi frequency of 85 MHz. For qubit 1 prepared in the ground state, along the white dashed line, the Rabi frequency $f = 31$ MHz of qubit 2 is lower. For qubit 1 in a superposition of the ground and excited states, qubit 2 shows a beating pattern of both oscillations.

A more detailed analysis allows us to unravel the two frequencies of Fig. 5.2b and determine which levels are participating in each of the oscillations. We extract the level occupations Q_{00}, Q_{01}, Q_{10} and Q_{11} from the individual switching probabilities (see Section 5.6). The result is shown in Figures 5.2c-f. After an odd number of π-rotations of qubit 1, there are only oscillations between states 10 and 11, not for states 00 and 01. After an even number of π-rotations of qubit 1 the situation is reversed; now the states 00 and 01 oscillate. The two oscillation frequencies are clearly linked to the two different transitions.

5.6 Extracting level occupations from detector switching-probabilities

The detectors are click-type detectors; they either switch or do not switch away from the initial state, depending on the sensed magnetic field. Their fidelities are lower than 1, and the base levels for the switching rates are free to choose. Here we present a procedure to extract the level occupations $Q_i = |\langle i|\psi\rangle|^2$, with $i = 00, 01, 10, 11$ and $|\psi\rangle$ the quantum state of the system.

Each individual measurement event can have one of four possible outcomes: neither detectors switches, only detector 1 switches, only detector 2 switches, or both switch. We determine the respective probabilities P_{00}, P_{01}, P_{10} and P_{11} by repeating the measurement many times. The individual switching probabilities

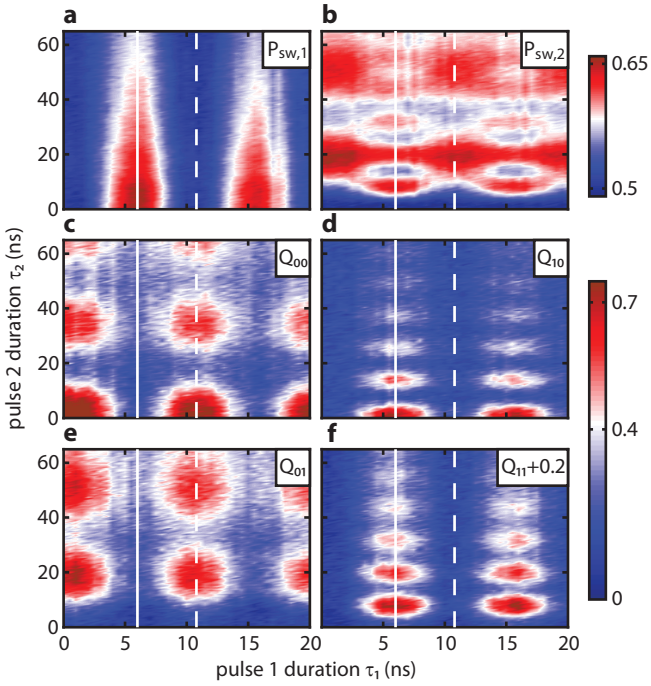

Figure 5.2: Driving from a single antenna. Measurement of the state of the qubits, represented by switching probabilities $P_{sw,1}$ and $P_{sw,2}$, after applying a pulse of duration τ_1 resonant with qubit 1, followed by a pulse of duration τ_2 resonant with qubit 2. **a**, $P_{sw,1}$, showing coherent oscillations of qubit 1 induced by pulse 1. The white solid and dashed lines indicate a π- and 2π-rotation respectively. For pulse 2, qubit 1 only shows relaxation. **b**, $P_{sw,2}$, showing coherent oscillations induced by pulse 2. After an odd number of π-rotations on qubit 1, the oscillation frequency is higher than after an even number of π-rotations. For superposition states of qubit 1, a beating pattern of the two oscillations is observed. **c-f**, Level occupations Q of the four different levels. Note that a value of 0.2 has been added to Q_{11} to improve visibility.

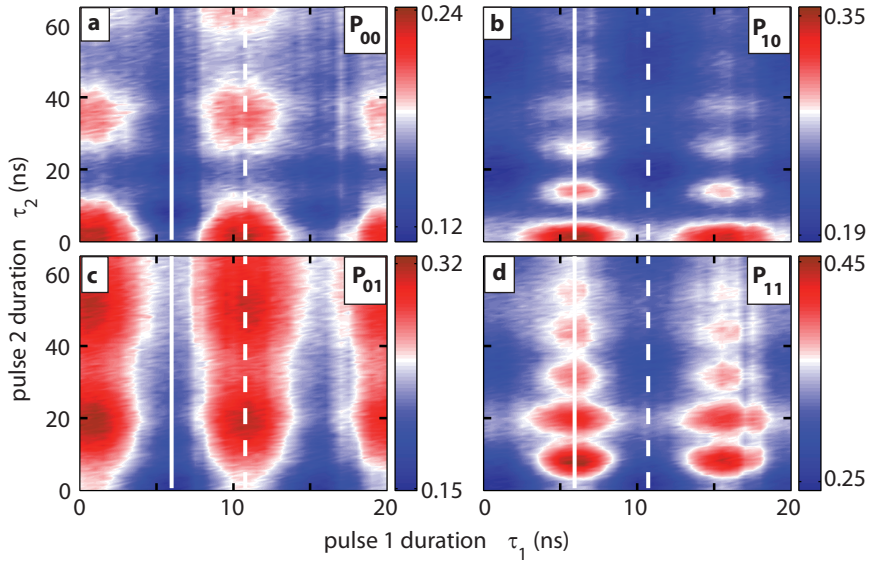

Figure 5.3: a-d Measured combined probabilities P in color versus the durations τ_1 and τ_2 of pulse 1 and pulse 2.

of the detectors are calculated from the combined probabilities: $P_{sw,1} = P_{10}+P_{11}$ and $P_{sw,2} = P_{01} + P_{11}$.

The quantities Q_n and P_n are related by

$$\vec{P} = M\vec{Q} \tag{5.20}$$

where $\vec{P} = (\ P_{00}\ P_{01}\ P_{10}\ P_{11}\ )^T$, $\vec{Q} = (\ Q_{00}\ Q_{01}\ Q_{10}\ Q_{11}\ )^T$ and

$$M = \begin{pmatrix} (1-G_1)(1-G_2) & (1-G_1)(1-E_2) & (1-E_1)(1-G_2) & (1-E_1)(1-E_2) \\ G_2(1-G_1) & E_2(1-G_1) & G_2(1-G_1) & E_2(1-E_1) \\ G_1(1-G_2) & G_1(1-E_2) & E_1(1-G_2) & E_1(1-E_2) \\ G_1G_2 & G_1E_2 & E_1G_2 & E_1E_2 \end{pmatrix} \tag{5.21}$$

The parameters G_i and E_i are the switching probabilities for detector i when the corresponding qubit is in the ground state (G) or the excited state (E) respectively. Assuming no crosstalk between the detectors (see Chapter 8), these four parameters fully characterize the measurement. The calibration values are determined from independent measurements. Measuring the switching probability without applying any driving pulse provides $G_1 = 0.507$ and $G_2 = 0.487$. In another two experiments either qubit 1 or qubit 2 was resonantly excited with a pulse duration much longer than the coherence times of the qubits, so that the final state is a 50/50 incoherent mixture of the ground and excited state. The full excited state must have twice this signal. This procedure is more reliable than doing a coherent π rotation, since that approach is susceptible to gate errors. We measure $E_1 = 0.760$ and $E_2 = 0.744$.

The matrix M is invertible for $G_i \neq E_i$, and the equation

$$\vec{Q} = M^{-1}\vec{P} \tag{5.22}$$

is used to extract the desired level occupations. Figure 5.3 shows the data for the four measurement outcomes of the experiment described in Section 5.5

5.7 Experiment 2: Transition strength tuning

To demonstrate the *tunability of the transition strengths* we drive both antennas simultaneously, using the same frequency and controlling independently the amplitudes A_1, A_2 and phases ϕ_1, ϕ_2. In this 2-pulse experiment (Fig. 5.1c), the first pulse prepares qubit 1 with a $\pi/2$-rotation and the duration τ_2 of the second pulse is varied. Since qubit 1 is in a superposition state, both Rabi frequencies are present in the dynamics of qubit 2. In Figures 5.4a-c we show the Fourier transform for the measured oscillations. Each graph is measured with a different

amplitude ratio A_1/A_2, with fixed phase $\phi_1 = 0$ and varying ϕ_2. Figure 5.4a, with $A_1/A_2 = 1.3$, shows a typical result for an arbitrary amplitude-ratio; the Rabi oscillation frequencies of both transitions clearly depend on $\phi_2 - \phi_1$, but nowhere a transition is darkened. Note the occurrence of equal Rabi frequencies for two phase conditions, as denoted by Y. For $A_1/A_2 = 2.5$ in Figure 5.4b we observe that for $\phi_2 - \phi_1 \approx \pi$ (indicated by X_0) the transition $10 \leftrightarrow 11$ is fully darkened, while the $00 \leftrightarrow 01$ transition shows a non-zero oscillation frequency. In Fig. 5.4c with $A_1/A_2 = 6.3$ the situation is reversed, with the $00 \leftrightarrow 01$ transition being suppressed (denoted by X_1). This clearly demonstrates our method, as we selectively excite one of two transitions, despite their frequency degeneracy. Calculations of T are in good agreement with the experimental results, provided we allow for different transmissions of amplitudes and phases of the antennas to the qubits, which we attribute to the influence of the detector circuits.

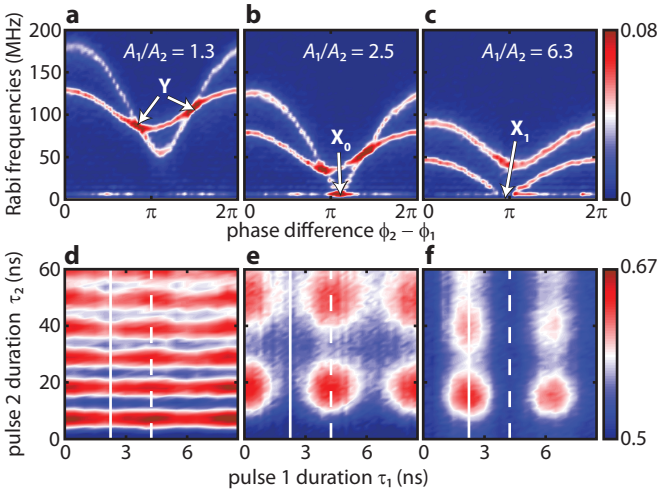

Figure 5.4: Transition strength tuning and darkened transitions. a-c, Rabi frequency dependence on $\phi_2 - \phi_1$ for three different amplitude-ratios. The color scale represents the Fourier component of $P_{sw,2}(\tau_2)$. Qubit 1 is prepared with a $\pi/2$-rotation. Markers X_0 and X_1 indicate the conditions for a darkened transition on $00 \leftrightarrow 01$ and $10 \leftrightarrow 11$ respectively. **d-f** $P_{sw,2}$ versus the durations τ_1 and τ_2. The white solid and dashed lines indicate a π- and 2π-rotation of qubit 1, respectively. The driving conditions are as marked by Y left arrow (**d**), X_0 (**e**) and X_1 (**f**).

5.8 Experiment 3: Darkened transitions

To further investigate the special cases of equal Rabi frequencies (Y), and *darkened transitions* (X_0, X_1), we again vary the durations τ_1 and τ_2, using both antennas for the second pulse. The results should be compared with Fig. 5.2b. Figure 5.4d shows $P_{sw,2}$ for driving conditions denoted by Y (left arrow): the oscillation frequency of qubit 2 does not depend on the state of qubit 1. For the conditions marked by X_0, we only observe oscillations of qubit 2 when qubit 1 is in the ground state, as shown in Fig. 5.4e. Similarly for the conditions marked by X_1, now we only observe oscillations of qubit 2 if qubit 1 is in the excited state (Fig. 5.4f).

The demonstrated capability to selectively manipulate transition strengths in frequency-degenerate transitions has important applications. A π-pulse using condition X_1 or X_0 provides a 1-controlled and 0-controlled NOT gate, respectively. This enables certain systems, including the flux qubit used here, to be fully operated at the coherence-optimal point, without level shifting by either DC or strong AC signals. Note that the use of additional coupling elements is neither required nor prohibited. If additional coupling elements are used, our method can replace more complicated schemes. For conditions similar to Y, taking care of the individual rotation angles, also single-qubit gates can be implemented. The controlled-NOT and single-qubit gates together form a universal set, implying that our method fulfills all requirements for constructing any single- or two-qubit gate.

5.9 Conclusions

In conclusion, we have introduced and experimentally demonstrated a method to control transition strengths by applying a non-uniform driving field. Darkened transitions are created and employed for the selective excitation of degenerate transitions. This method introduces a new method for entangling gates, which can replace or complement the available operations in a variety of quantum systems. For systems with sweet-spot operation points such as the flux qubit, the prospects for performing quantum algorithms is enhanced significantly.

Bibliography

[1] J. E. Mooij, T. P. Orlando, L. Levitov, L. Tian, C. H. van der Wal, and S. Lloyd, Josephson Persistent-Current Qubit, Science **285**, 1036–1039 (1999).

[2] Y. Nakamura, Y. A. Pashkin, and J. S. Tsai, Coherent Control of Macroscopic Quantum States in a Single-Cooper-Pair Box, Nature **398**, 786–788 (1999).

[3] D. Vion, A. Aassime, A. Cottet, P. Joyez, H. Pothier, C. Urbina, D. Esteve, and M. H. Devoret, Manipulating the quantum state of an electrical circuit, Science **296**, 886–889 (2006).

[4] J. M. Martinis, S. Nam, J. Aumentado, and C. Urbina, Rabi oscillations in a large Josephson-junction quibt, Phys. Rev. Lett **89**, 117901 (2002).

[5] J. A. Schreier, A. A. Houck, J. Koch, D. I. Schuster, B. R. Johnson, J. M. Chow, J. M. Gambetta, J. Majer, L. Frunzio, M. H. Devoret, S. M. Girvin, and R. J. Schoelkopf, Suppressing charge noise decoherence in superconducting charge qubits, Phys. Rev. B **77**, 180502 (2008).

[6] V. E. Manucharyan, J. Koch, L. I. Glazman, and M. H. Devoret, Fluxonium: Single Cooper-Pair Circuit Free of Charge Offsets, Science **326**, 113–116 (2009).

[7] N. Linden, H. Barjat, and R. Freeman, An implementation of the Deutsch-Jozsa algorithm on a three-qubit NMR quantum computer, Chemical Physics Letters **296**, 61 – 67 (1998).

[8] J. H. Plantenberg, P. C. de Groot, C. J. P. M. Harmans, and J. E. Mooij, Demonstration of controlled-NOT quantum gates on a pair of superconducting quantum bits, Nature **447**, 836–839 (2007).

[9] J. A. Jones and E. Knill, Efficient Refocusing of One-Spin and Two-Spin Interactions for NMR Quantum Computation, Journal of Magnetic Resonance **141**, 322 – 325 (1999).

[10] G. S. Paraoanu, Microwave-induced coupling of superconducting qubits, Phys. Rev. B **74**, 140504 (2006).

[11] A. O. Niskanen, K. Harrabi, F. Yoshihara, Y. Nakamura, S. Lloyd, and J. S. Tsai, Quantum Coherent Tunable Coupling of Superconducting Qubits, Science **316**, 723–726 (2007).

[12] M. A. Sillanpää, J. I. Park, and W. Simmonds, Coherent quantum state storage and transfer between two phase qubits via a resonant cavity, Nature **449**, 438–442 (2007).

[13] R. McDermott, R. W. Simmonds, M. Steffen, K. B. Cooper, K. Cicak, K. D. Osborn, S. Oh, D. P. Pappas, and J. M. Martinis, Simultaneous State Measurement of Coupled Josephson Phase Qubits, Science **307**, 1299–1302 (2005).

[14] C. Rigetti, A. Blais, and M. Devoret, Protocol for Universal Gates in Optimally Biased Superconducting Qubits, Phys. Rev. Lett. **94**(24), 240502 (2005).

[15] J. Majer, J. M. Chow, J. M. Gambetta, J. Koch, B. R. Johnson, J. A. Schreier, L. Frunzio, D. I. Schuster, A. A. Houck, A. Wallraff, A. Blais, M. H. Devoret, S. M. Girvin, and R. J. Schoelkopf, Coupling superconducting qubits via a cavity bus, Nature **449**, 443–447 (2007).

[16] R. W. Simmonds, K. M. Lang, D. A. Hite, S. Nam, D. P. Pappas, and J. M. Martinis, Decoherence in Josephson Phase Qubits from Junction Resonators, Phys. Rev. Lett. **93**, 077003 (2004).

[17] F. Yoshihara, K. Harrabi, A. O. Niskanen, Y. Nakamura, and J. S. Tsai, Decoherence of flux qubits due to 1/f flux noise, Phys. Rev. Lett. **97**, 167001 (2006).

[18] Y.-x. Liu, L. F. Wei, J. S. Tsai, and F. Nori, Controllable Coupling between Flux Qubits, Phys. Rev. Lett. **96**, 067003 (2006).

[19] P. Bertet, C. J. P. M. Harmans, and J. E. Mooij, Parametric coupling for superconducting qubits, Phys. Rev. B **73**, 064512 (2006).

[20] A. Lupaşcu, S. Saito, T. Picot, P. C. de Groot, C. J. P. M. Harmans, and J. E. Mooij, Quantum non-demolition measurement of a superconducting two-level system, Nature Physics **3**, 119–125 (2007).

[21] P. C. de Groot, A. F. van Loo, J. Lisenfeld, R. N. Schouten, A. Lupaşcu, C. J. P. M. Harmans, and J. E. Mooij, Low-crosstalk bifurcation detectors for coupled flux qubits, Appl. Phys. Lett. **96**, 123508 (2010).

Chapter 6

Decoherence in a two-qubit system

Decoherence in a multi-qubit system involves some aspects that do not exist in a single-qubit system. In this chapter we will study these aspects, focussing on the simple case of two coupled qubits. Section 6.1 discusses the situation where a single noise source couples to two qubits. To illustrate the effect of the resulting correlated noise in the two qubits, two experiments are proposed that use characteristic features in the decoherence to determine the geometric location of a dominant relaxation or dephasing source. In section 6.2 we study a second aspect of multi-qubit decoherence: relaxation to an intermediate state. We present relaxation measurements on a coupled-qubit system. The unfortunate existence of two strong relaxation-enhancing circuits on one of the devices enables us to observe this multi-qubit decoherence phenomenon.

6.1 Location of a noise source

Two important categories of decoherence are circuit noise, i.e. noise that comes from the circuits used for readout and control of the qubits, and noise from microscopic noise sources in the vicinity of the qubit, which are often intrinsic to the employed materials. This distinction is useful from an engineering point of view, as the approach for dealing with these two categories lies either in electrical circuit design or in material science. Because of its more intrinsic nature, microscopic noise receives the most active attention [1, 2, 3, 4, 5] , however new insights on the effects of circuit noise still sometimes emerge [6] and new device designs often take several steps of maturing before all the subtleties in the circuit noise are properly addressed.

Another useful distinction is between localized noise sources and distributed noise sources. A localized noise source couples to the qubits from a well defined geometric location. The noise source can be an ensemble of noise sources, and the dimensions of the relevant structures are allowed to be large compared to the qubit dimensions, as long as the individual noise sources have the exact same *effective location* from the perspective of the qubit coupling. In other words, if a noise source or a collection of noise sources can be replaced with a single (point) noise source with appropriate spectral density that is for the qubits indistinguishable from the original source(s), we call the whole collection a single localized noise source. A distributed noise source is an ensemble of noise sources distributed over a surface or volume with such high numbers that it is often more appropriate to consider the *density* of the noise sources rather than their exact locations. From this perspective, all circuit noise is localized, as well as certain microscopic noise sources, such as a vortex in a superconductor hopping between two pinning sites, or single two-level fluctuators [2]. An example of distributed noise is the widely encountered 1/f charge noise [1] and 1/f flux noise [4]. Distinguishing between localized noise and distributed noise can be a valuable indication to find the origin of noise encountered in an experiment.

For the decoherence of a two-qubit system the location of a noise source plays an important role. Two independent noise sources each of which couples to one of the two qubits have a different effect from a single noise source coupling to both qubits. In the first case the noise in one qubit is uncorrelated with the noise in the other, while in the second case it is fully correlated. This affects both the relaxation and the dephasing of the system. We will discuss the important aspects of multi-qubit decoherence by proposing an experiment that uses characteristic features in the decoherence to determine the location of a dominant noise source. We focus on flux noise, as flux is the most natural quantity coupling to a flux-qubit (see Chapter 2), but similar methods can be used for any other noise parameter.

6.1.1 Relaxation

Any single noise source can be described to have an individual coupling strength to each qubit. These coupling strengths are determined to a large extent by geometry, i.e. the locations and shapes of the noise source and the qubits. This is illustrated in Figure 6.1, where a point source is placed at a distance r_1 from qubit 1 and r_2 from qubit 2. For noise sources placed much farther than the relevant qubit dimensions $r_1 \approx r_2$. In this case the noise couples equally to the two qubits. For noise sources placed closer to the qubits the relative coupling can take any value, with in the limiting cases only coupling to one of the two qubits.

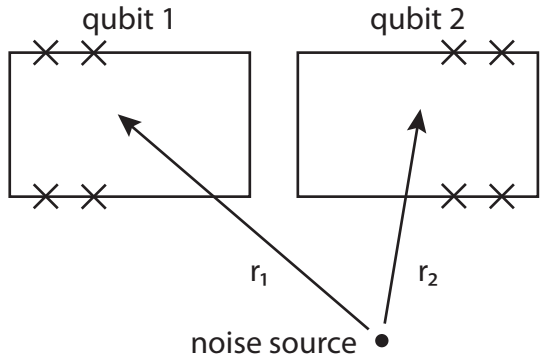

Figure 6.1: Schematic representation of two coupled flux qubits and a single noise source located a distance r_1 from qubit 1 and r_2 from qubit 2. The location of the source will influence the relative coupling strength to the two qubits.

Mathematically the formalism of relaxation in a single-qubit system and in a multi-qubit system is the same. Combining Equations 2.29 and 2.30, the relaxation rate of an excited state $|k\rangle$ to a lower energy state $|l\rangle$ is to first order given by

$$\Gamma_{1,k\to l} = \frac{\pi}{h^2}\left|\langle l|\frac{\partial H_0}{\partial \lambda}|k\rangle\right|^2 S_\lambda(\omega_{kl}), \tag{6.1}$$

where $S_\lambda(\omega_{kl})$ is the spectral density of the noise in the parameter λ at the level-splitting frequency ω_{kl} (see also Section 2.3) and

$$H_0 = -\frac{\varepsilon_1}{2}\sigma_z^1 - \frac{\Delta_1}{2}\sigma_x^1 - \frac{\varepsilon_2}{2}\sigma_z^2 - \frac{\Delta_2}{2}\sigma_x^2 + J\sigma_z^1\sigma_z^2 \tag{6.2}$$

is the Hamiltonian describing the unperturbed system. Here Δ_i is the energy gap and $\varepsilon_i = -2I_{p,i}(\Phi_i - \Phi_0/2)$ is the magnetic energy bias, with $I_{p,i}$ and Φ_i the persistent current and flux bias of qubit i.

We focus on the parameter λ, which describes how a noise source couples to the system, i.e. to which parameter of the Hamiltonian the noise couples. For a source of flux noise coupling to both qubits, λ is given by

$$\lambda = a_1\Phi_1 + a_2\Phi_2 \tag{6.3}$$

where a_1 and a_2 are dimensionless scaling factors that represent the relative coupling strength of the noise source to the two qubits and generally depend on the location (r_1, r_2) of the source. (see Figure 6.1). For the partial derivative in Eq. (6.1), we now substitute

$$\frac{\partial}{\partial\lambda} = a_1\frac{\partial}{\partial\Phi_1} + a_2\frac{\partial}{\partial\Phi_2}, \tag{6.4}$$

which results in

$$\frac{\partial H_0}{\partial\lambda} = a_1 I_{p,1}\sigma_z^1 + a_2 I_{p,2}\sigma_z^2. \tag{6.5}$$

We conclude that when a source of flux noise couples to both qubits, the relaxation rate scales as

$$\Gamma_{1,k\to l} \sim \left|\langle l|\beta\sigma_z^1 + (1-\beta)\sigma_z^2|k\rangle\right|^2, \tag{6.6}$$

where we substituted $\beta = a_1 I_{p,1}/(a_1 I_{p,1}+a_2 I_{p,2})$. The factor β has the convenient property that the full range of relative coupling strengths is given by β ranging from 0 (only coupled to qubit 2) to 1 (only coupled to qubit 1).

The scaling of the relaxation rate expressed in Eq. 6.6 has some interesting properties. Similar to the single-qubit case, the relaxation rate depends on the flux biases Φ_1 and Φ_2 through their influence on the eigenvectors $|k\rangle$ and $|l\rangle$. In addition, the relaxation rate depends on the relative coupling strength β, and can be *fully suppressed* for specific values of β. The value of β for which the relaxation is suppressed, which we denote by β_{kl}^0, depends on the magnetic frustration of the qubits. Figure 6.2(a) shows the dependence of β_{10}^0 on the two flux biases Φ_1 and Φ_2. Note that we focus on the $|1\rangle$-$|0\rangle$ transition so only a single relaxation rate needs to be taken into account; in Section 6.2 we discuss relaxation from higher energy levels.

The full suppression of the relaxation can be understood intuitively in light of the results of Chapter 5, where we demonstrated that the excitation of specific transitions can be suppressed for an appropriate ratio of driving amplitudes. Now imagine that we replace two antennas with a single antenna, and place it such that the relative coupling strength to the two qubits exactly meets the requirements for a darkened transition. This antenna cannot excite the transition to first order. If we now consider the antenna as a source of flux noise, it is also clear that it

could not induce any relaxation, because both the (flux) driving and the flux noise couple to the system in the same way (compare Equations 5.2 and 6.5, and keep in mind the different choice of basis).

The dependence of β_{10}^0 on the flux biases allows us to propose an experiment that, in the case of a single dominant source of relaxation, can determine the location of the source. Any localized source will have a fixed β that is determined by its geometry and location with respect to the two qubits. Measuring the relaxation time of the first excited state as a function of the two flux biases, will exhibit an optimum relaxation time whenever $\beta_{10}^0(\Phi_1, \Phi_2)$ is equal to the fixed β of the noise source. As mentioned earlier, the β of a noise source contains information regarding its geometric location. Figure 6.3 shows a device with contour lines that indicate what the value of β would be for a noise source located on that position on the chip. For the calculation of the contours we assumed that the noise source and the qubits are magnetic point dipoles. Note that experimentally the noise of a specific source often does not have a flat spectrum. This might make the interpretation of the optimum coherence time significantly harder. A practical solution for this problem is to measure the relaxation along an iso-line of the energy splitting. The black line in Fig. 6.2(a) is an example of such a contour at $\nu_{01} = \omega_{01}/(2\pi) = 6.1$ GHz.

One thing we have been ignoring so far is the role of the phase difference $\delta\varphi$ of the noise picked up by the two qubits. From a geometrical point of view, it is to be expected that for most noise sources either $\delta\varphi = 0$ (noise source localized outside the qubit loops) or $\delta\varphi = \pi$ (noise source localized in one of the qubit loops). As mentioned in Chapter 5 however, electrical circuitry might cause some additional phase shift. The model can be easily extended to take the phase into account, similarly to what was done in Chapter 5, but will not be discussed further here.

As a final note, we stress that unlike the coherent excitation in the darkened transition experiment, two noise sources of different β *cannot* be treated by first summing the noise and calculating an effective β. The rates need to be determined individually and added afterwards. For example, two noise sources placed symmetrically with respect to the qubits ($\beta_{\mathrm{src1}} = 1 - \beta_{\mathrm{src2}}$) are not equivalent to one noise source with $\beta_{\mathrm{src3}} = 0.5$. The difference is that in the case of coherent qubit excitation the two driving fields are applied fully (phase) correlated, while two independent noise sources are uncorrelated. A single source of $\beta = 0.5$ has some forbidden transitions, while two sources of different β will each have different conditions for a forbidden transition. At any frustration the strongest relaxation source will determine the total rate; the forbidden transition of one source is washed out by the relaxation of the other. For this reason, the proposed experiment only works in the case of a single dominant noise source. Alternatively, the absence of optima in the relaxation times can indicate that there is more than one dominant noise source, or that the noise is completely distributed.

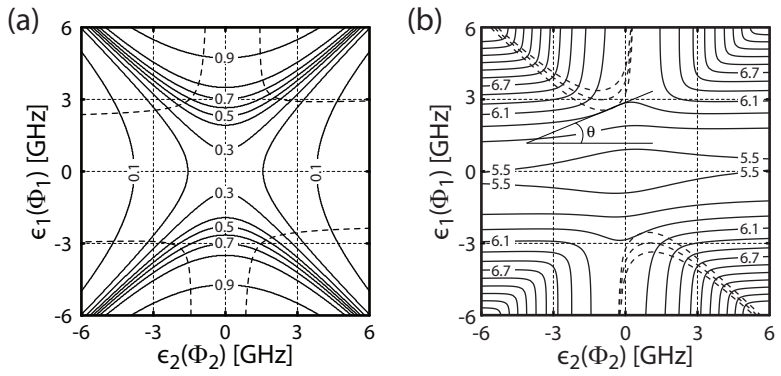

Figure 6.2: (a) The solid lines represent contours of the relative coupling strength β_{10}^0 for which the relaxation rate is to first order suppressed versus the energy biases ε_1 and ε_2. The dashed lines indicate where the level-splitting $\nu_{01} = 6.1$ GHz. (b) Solid lines represent contours of ν_{01} versus ε_1 and ε_2. Dashed lines indicate where $\partial\nu_{01}/\partial\lambda = 0$ for $\beta = 0.33,\ 0.50,\ 0.67$ ($\theta = 26^\circ,\ 45^\circ,\ 64^\circ$), ordered from center outward.

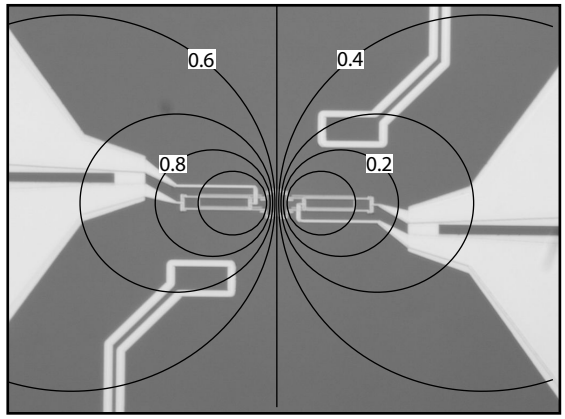

Figure 6.3: Scanning Electron Micrograph of a device of two coupled flux qubits. The qubits are visible in the center, two driving antennas on the top right and bottom left and two capacitor plates on the left and right. The black lines superimposed on the image indicate what the value of β would be for a noise source located on that position of the chip. For simplicity, the noise source and qubits were assumed to be magnetic point dipoles.

6.1.2 Dephasing

When a noise source couples to multiple qubits it also affects the dephasing. Again we will show that characteristic properties can be used to acquire information on the location of the noise source. As discussed in Section 2.3, the total dephasing consists of pure dephasing and relaxation-induced dephasing; here we discuss the pure dephasing.

The pure dephasing rate between two states $|k\rangle$ and $|l\rangle$ is to first order given by

$$\Gamma_{\varphi,kl} = \pi \left(\frac{\partial \omega_{kl}}{\partial \lambda} \right)^2 S_\lambda(\omega \approx 0), \tag{6.7}$$

where ω_{kl} is the angular frequency that corresponds to the level splitting, λ is the parameter that contains the noise and $S_\lambda(\omega)$ is the spectral density of the noise (see Section 2.3).

From this point on the analysis of the dephasing rate can be done completely analogously to the relaxation case described in Section 6.1.1, taking $\lambda = a_1\Phi_1 + a_2\Phi_2$ and substituting the partial derivative and $\beta = a_1 I_{p,1}/(a_1 I_{p,1} + a_2 I_{p,2})$. For a dominant noise source with fixed β, the derivative will be zero for characteristic points in the flux bias and at these points will exhibit an optimum dephasing time. These optimum dephasing points can be found experimentally and translated to an effective β. The geometric location of the noise source can than be determined as in Fig. 6.3. Note that these optimum dephasing points are closely related to the topic of decoherence free subspaces.

To reach a more intuitive understanding of the optima in the two-qubit dephasing, we translate the parameter β to an angle θ in the Φ_1, Φ_2-plane by

$$\tan\theta = \frac{a_1}{a_2} \tag{6.8}$$

This angle θ describes a direction in which a given noise source can move the system (see Figure 6.2(b)). Starting from an arbitrary point on the Φ_1, Φ_2-plane, the magnetic flux coming from this source moves us on a straight line in the plane. As an example we will consider an external coil $\beta_{ext} = 0.5,\ \theta_{ext} = 45°$, and two on-chip antennas with $\beta_{A1} = 0.33,\ \theta_{A1} = 26°$ and $\beta_{A2} = 0.67,\ \theta_{A2} = 64°$. Any (localized) source of flux noise can only move the system along a certain direction in the Φ_1, Φ_2-plane.

The interpretation of the relative coupling strength as an angle in the Φ_1, Φ_2-plane makes it simple to identify coherence optimal points from the energy level splitting. Figure 6.2 shows iso-lines of $\nu_{01} = \omega_{01}/(2\pi)$ versus Φ_1 and Φ_2. For a given noise source, the dephasing time will exhibit an optimum at *any* point in the graph where the iso-lines run in parallel with the direction characteristic

for that noise source. At these points, to first order, the level splitting does not change for noise in the parameter λ. As an example, the dashed lines in Fig. 6.2 show the lines of optimum phase-coherence for noise originating from the above mentioned external coil, antenna 1 and 2, ordered from center outward.

In a recent experiment by Yoshihara *et al.* [7], a similar method was used to show that the dominant source of dephasing in their system was distributed, rather than a single localized (global) noise source.

In conclusion, we have discussed the properties of decoherence as a result from noise sources that couple to both qubits. Two experiments are proposed that use the characteristic features to acquire information on the geometric location of a dominant noise source, or, in absence of the characteristic features, can help to conclude there is more than a single dominant noise source. The proposed experiments are considered useful for identifying noise sources. Identifying noise sources can greatly assist improvements in device designs. For general qubit experiments, however, it is still favourable to bias both qubits at $\Phi_0/2$, where the dephasing time is optimal for *any* (flux) noise source coupling to the system, and for *all* level splittings.

6.2 Relaxation to an intermediate state

In this section we present experimental results on another decoherence process that is typical for a multi-level system: relaxation to an intermediate state. Two resonator circuits, strongly coupled to the qubits, and with a decay time much shorter than the decay time of the qubits, dominate the relaxation time when an energy splitting in the two-qubit system matches the resonance frequency of one of the circuits. This effect is otherwise known as the Purcell-effect [8], which describes the lifetime of an excited state of a quantum object in a cavity.

In a multi-level system, any state higher than the first excited state can relax to the ground state via multiple paths. A 2-qubit system comprises four levels, which means that two of these levels are now of main interest; the highest (3rd) excited state, where both qubits are excited, and the 2nd excited state, where only the qubit with highest splitting is excited. Figure 6.4(a) shows a schematic of the possible relaxation paths. The total relaxation rate of these states is given by the sum of the individual relaxation rates. Note that we will often refer to the excitation or relaxation of one of the two qubits, even though the eigenstates of two permanently coupled qubits are not separable into single qubit states. Nevertheless, it significantly helps in getting an intuitive understanding and is a good approximation when both qubits are biased far away from energy degeneracy points, and points of degenerate level splittings.

The measured device consists of two coupled qubits ($\Delta_1 = h \times 2.1$ GHz, $I_{p,1} = 540$ nA, $\Delta_2 = h \times 4.8$ GHz, $I_{p,2} = 470$ nA, $J = h \times 250$ MHz), and two separate

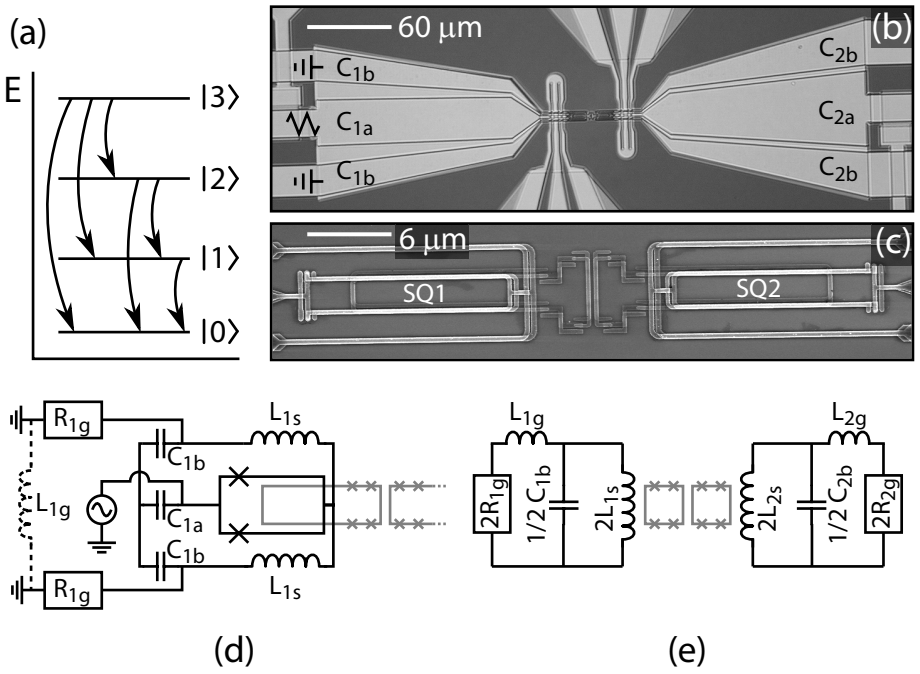

Figure 6.4: (a) Energy level diagram of two coupled qubits with arrows indicating the possible relaxation paths for each level. (b) Optical micrograph showing an overview of the circuits. The qubits and SQUIDs are placed at the center. At the left and right are the capacitor plates, where each capacitor consists of a split design for symmetric coupling to the qubits of certain current paths. At the top and bottom are two waveguides used for qubit driving. (c) Scanning Electron Micrograph of the qubits and SQUIDs. Note the splitting of connection lines of the SQUIDs. (d) Schematic representation of the circuits. For the primary resonance mode, which is used for the readout, the current path runs through the SQUID and $C_{1,2a}$, and splits up equally along the two outer branches with inductance $L_{1,2s}$ and capacitance $C_{1,2b}$. For the extra resonance mode the current runs only along the outer branches, involving only $C_{1,2b}$ and $L_{1,2s}$ (2x in series). (e) Simplified schematic of the extra resonance mode, drawn for both detectors. The load resistance is formed by the ground loop indicated by the dashed line in (d).

qubit-state detectors (see Fig. 6.4(d)). Each detector consists of a resonant circuit, with a resonance frequency of $\sim$ 1.5 GHz. These detector circuits are designed in a symmetrically-split geometry to cancel to first order any noise coupling to the qubits coming from the connection lines of the SQUID-loop. As a consequence of the symmetry, a second resonance in the circuit is introduced with a frequency differing from the 1.5 GHz resonance. The components leading to this resonance are $C_{1,2b}$ and $L_{1,2s}$; they are situated in the two outer branches in Fig. 6.4(d). Notice also the low-impedance path formed by the two ground connections. This load damps the oscillators; the quality factor Q of the oscillators is low.

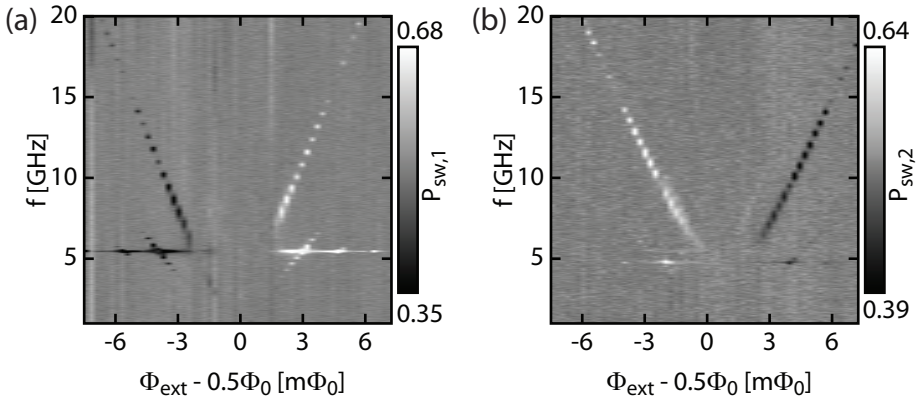

Figure 6.5: Measured spectra of the qubits for detector 1 (a) and detector 2 (b) as a function of the applied external magnetic flux Φ_{ext}. The primary qubit resonance are clearly visible, as well as slightly fainter 2- and 3-photon lines. In addition to the qubit related resonances, detector 1 shows a clear resonance at 5.5 GHz and detector 2 at 4.8 GHz. These are associated to the extra resonance mode in the detector circuits.

A spectroscopy experiment is performed, varying the externally applied magnetic flux Φ_{ext} and the frequency f of the excitation pulse. The measurement outcomes of the individual detectors are shown in Fig. 6.5. The color scale is the switching probability of the AC-operated bifurcation detectors; for more information on the detectors see Chapter 7. The $|0\rangle$-$|1\rangle$ and $|0\rangle$-$|2\rangle$ resonances are clearly visible, as well as some weaker 2- and 3-photon lines of those transitions. Additionally we see a horizontal line at 5.5 GHz and 4.8 GHz on detector 1 and 2 respectively. These lines are the extra resonance frequencies f_{res1} and f_{res2} of the corresponding detector circuits of Figure 6.4(d,e); as expected they do not depend on the applied magnetic flux.

The relaxation times of the first and second excited states are measured. The

system is excited with a resonant pulse, and the time between the excitation and measurement is varied. The resulting decay is fitted with an exponential decay. This experiment is repeated for each transition, and for various external magnetic fields. The result is shown in Figure Fig. 6.6(b), where the relaxation time T_1 is plotted as a function of the resonance frequency ν. Figure Fig. 6.6(a) shows the corresponding resonance frequencies versus the applied external flux. The triangles represent the transitions that excite the transition we associate with qubit 1; pointing upward for magnetic flux bias below the degeneracy point, downward for above. Similarly for qubit 2; squares for below the degeneracy point, circles for above.

These relaxation measurements show a number of interesting features. First of all both qubits show a general upward trend for resonance frequencies above 5 GHz. Around and below 5 GHz the relaxation time was either too short to measure, or the signal amplitude was too low to detect. The extremely low relaxation time around 5 GHz is caused by the lossy resonators that are visible in the spectroscopy measurement. This will be discussed further below.

All curves show sharp dips in the relaxation time at specific frequencies. The main trend-line of the relaxation time lies significantly higher for qubit 1 than for qubit 2, which is qualitatively consistent with the relative qubit gaps, assuming they experience approximately the same level of noise; for uncoupled qubits the transition strength should scale with Δ^2 (Section 2.3).

The relaxation times of transitions below and above the degeneracy point are roughly equal and have dips at the same frequencies (per qubit). One of the two prominent points where this does not hold is for the relaxation time of qubit 1 at $\nu \approx 12.4$ GHz. The relaxation time has a clear dip at fields above the degeneracy point (circles), while this dip is clearly absent on the other branch (squares). The remainder of this section will focus on this difference in relaxation times of qubit 1.

The asymmetry in the measured relaxation times can be understood by considering the extra relaxation paths. As shown in Fig. 6.6(a), the transitions of qubit 1 on the left hand side are associated with transitions between $|0\rangle$ and $|1\rangle$, while on the right-hand side they are between $|0\rangle$ and $|2\rangle$. For qubit 2 these are swapped. The dip is observed on the right-hand side, at a position where the splitting between $|2\rangle$ and $|1\rangle$ is 5.5 GHz. This splitting is equal to the resonance frequency of the resonator in the detector circuit of qubit 1. These observations suggest that at this specific frequency, state $|2\rangle$ relaxes primarily to $|1\rangle$, rather than $|0\rangle$. Note that this implies that after this relaxation step, qubit 2 is in the excited state.

To verify that the relaxation of qubit 1 is indeed through the excitation of qubit 2, we employ two dc bias currents through the two on-chip antennas. Using these bias currents we change the splitting of qubit 2 while keeping the splitting

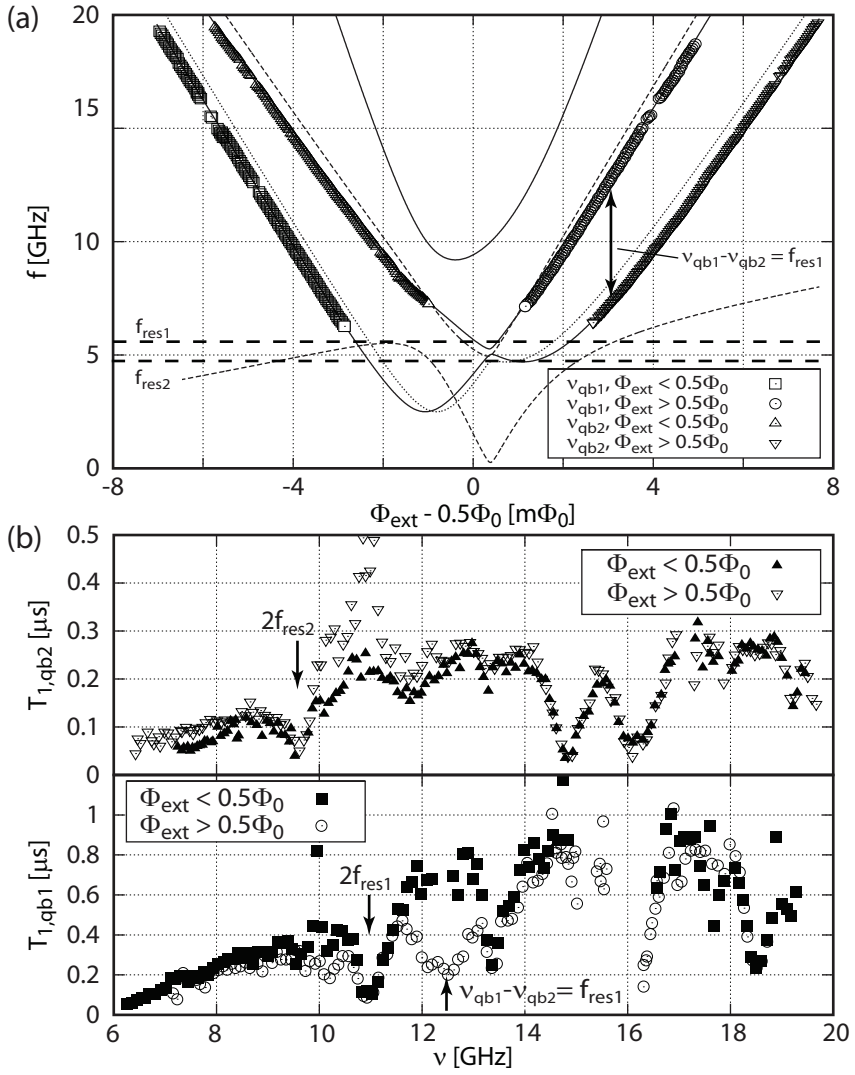

Figure 6.6: (a) Spectroscopy measurement showing the resonance frequency versus the applied external magnetic flux. Symbols indicate the center of a measured resonance peak, lines are theoretical calculations using the system parameters and a flux offset of 1.87 mΦ_0. Solid, dashed and dotted lines indicate transitions from the ground, 1st excited and 2nd excited state respectively. (b) Relaxation time of each of the resonances in (a). The top panel contains the transitions associated with qubit 1, and the bottom panel the transitions of qubit 2.

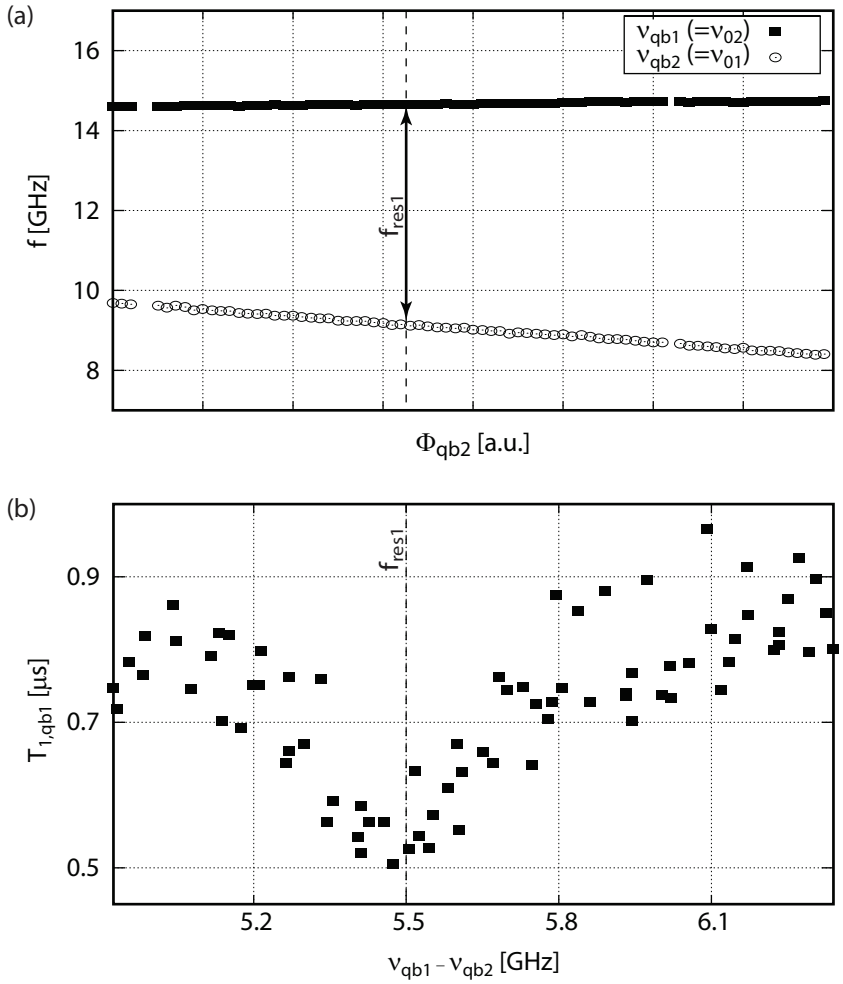

Figure 6.7: (a) Measured resonance frequencies ν_{qb2} and ν_{qb1} versus the flux bias Φ_2 of qubit 2. The independent flux bias of qubit 2 is achieved by applying currents through two local bias lines. (b) Measured relaxation time T_1 of the second excited state (which is the excited state of qubit 1), versus the difference in level splittings $\nu_{\mathrm{qb1}} - \nu_{\mathrm{qb2}}$.

of qubit 1 constant at 14.7 GHz. This should exclude the option that the direct transition of qubit 1 passes a resonance with another system that we cannot see with our detectors. The result is shown in Fig. 6.7. When the splitting of qubit 2 is such that the difference in energies ($\nu_{\mathrm{qb1}} - \nu_{\mathrm{qb2}} = f_{\mathrm{res1}} = 5.5$ GHz), which is exactly equal to the resonator frequency, a reduction of T_1 is observed. We conclude that the relaxation of qubit 1 is not directly to the ground state, but because of the strongly enhanced relaxation at this specific frequency, the relaxation to the excited state of the other qubit is dominant.

What was pursued, but not observed, is the enhanced population of qubit 2, measured with detector 2, caused by the relaxation of qubit 1. This is likely caused by the low relaxation time of the first excited state to the ground state (relaxing qubit 2), compared to the relaxation of the second excited state to the first excited state (relaxing qubit 1 and exciting qubit 2). The first excited state is faster "de-populating" than it is filled from the second excited state.

Using a simple model of two simple parallel LRC-resonators (see Figure 6.4(e), and Section 2.3.2), the expected T_1 for both qubit 1 and qubit 2 is calculated and plotted in Fig. 6.8. For simplicity we assumed that each resonator couples only to the closest qubit, implying $\beta = 1$ for the resonance in detector 1 and $\beta = 0$ for the resonance in detector 2. The simple model reproduces the strong relaxation directly to the ground state around the resonator frequencies (5.5 GHz and 4.8 GHz), and for qubit 1 the enhanced relaxation at 12.4 GHz for the branch that represents relaxation from the second excited state. The latter is clearly dominated by the $|1\rangle$-$|2\rangle$ transition (dashed line). What is not observed, or at least not unambiguously, are the two dips in relaxation time of qubit 2, that should only occur in the branch of the second excited state. For the dip at ≈ 7 GHz, there is a slight difference between the two data set between 7 GHz and 8 GHz, but not very significant. Secondly, close to 7 GHz the signal was too low to determine the relaxation time reliably. The dip in relaxation time could in fact be the reason for the reduced signal. For the dip at ≈ 16 GHz both branches, and even both qubits, exhibit a strong reduction of the relaxation time. This is most likely caused by another, unknown, source of relaxation. The strong dependence of T_1 on the level splitting in the calculations, and very high relaxation times at high level splittings are not observed in the measurements. This indicates that away from the resonance conditions, other noise sources determine the trend of the relaxation.

There are many dips remaining in the relaxation time measurements that are not described by this simple model. The dips at 11.0 GHz and 9.6 GHz for respectively qubit 1 and 2 are most likely the 2-photon processes of the strong relaxation to the ground state induced by the oscillators. The origin(s) of the other dips in the T_1 are unknown, as is the origin of the peak in T_1 of qubit 2, at a splitting of 11.0 GHz. Note that the peak of qubit 2 is not related to the dip

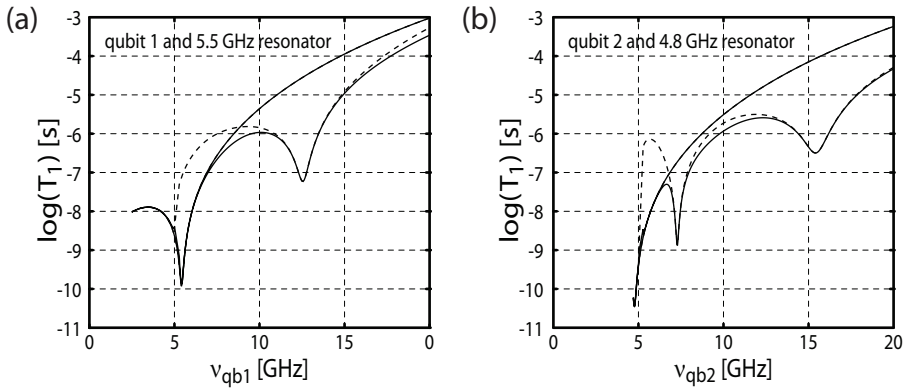

Figure 6.8: Relaxation time calculations using the system parameters from the experiment presented in Figure 6.6 and assuming only two noise sources. Both noise sources are parallel LRC-circuits as illustrated in Figure 6.4, coupled to the qubit inductively through the "L" branch. The lines represent the relaxation times of the first and second excited states of the coupled qubit system. Panel (a) shows the calculated relaxation from the states that are associated with qubit 1, and panel (b) the relaxation from the states that are associated with qubit 2. The solid lines represent the total effective relaxation time, incorporating both the relaxation to the ground state $|0\rangle$, and, when relevant, to state $|1\rangle$. The dashed line is only for relaxation from $|2\rangle$ to $|1\rangle$. For a significant range of $\nu_{\mathrm{qb1,2}}$, the relaxation from $|2\rangle$ to $|1\rangle$ is dominant. For the calculations we used $T = 0$ K, $2L_{1,2s} = 62$ pH, $2R_{1,2g} = 5\ \Omega$, $C_{1b}/2 = 15.5$ pF, $C_{2b}/2 = 20$ pF, $L_l = 0.5$ nH, a coupling between resonator and qubit of $M = 2$ pH, and no coupling of the resonator to the far qubit. The latter implies that $\beta = 1$ for the 5.5 GHz resonator coupled to qubit 1 and $\beta = 0$ for the 4.8 GHz resonator coupled to qubit 2.

in T_1 of qubit 1, because these splittings occur at a different flux bias.

In conclusion we have presented measurements of the relaxation time of a two-qubit system, and observed a typical multi-qubit phenomenon: relaxation to an intermediate state. This indicates that for designing a device for maximum coherence it is important to take all these relaxation paths into account. Additionally the measurements presented here helped us to identify a huge source of decoherence and led us to an improved device design where the symmetric design was abandoned to eliminate the extra resonance and ground loop. In this new device no strong dips in the relaxation time were observed.

Bibliography

[1] D. Vion, A. Aassime, A. Cottet, P. Joyez, H. Pothier, C. Urbina, D. Esteve, and M. H. Devoret, Manipulating the quantum state of an electrical circuit, Science **296**, 886–889 (2006).

[2] R. W. Simmonds, K. M. Lang, D. A. Hite, S. Nam, D. P. Pappas, and J. M. Martinis, Decoherence in Josephson Phase Qubits from Junction Resonators, Phys. Rev. Lett. **93**, 077003 (2004).

[3] M. Constantin and C. C. Yu, Microscopic Model of Critical Current Noise in Josephson Junctions, Phys. Rev. Lett. **99**(20), 207001 (2007).

[4] F. Yoshihara, K. Harrabi, A. O. Niskanen, Y. Nakamura, and J. S. Tsai, Decoherence of flux qubits due to 1/f flux noise, Phys. Rev. Lett. **97**, 167001 (2006).

[5] J. Eroms, L. C. van Schaarenburg, E. F. C. Driessen, J. H. Plantenberg, C. M. Huizinga, R. N. Schouten, A. H. Verbruggen, C. J. P. M. Harmans, and J. E. Mooij, Low-frequency noise in Josephson junctions for superconducting qubits, Applied Physics Letters **89**, 122516 (2006).

[6] M. Steffen, F. Brito, D. DiVincenzo, S. Kumar, and M. Ketchen, Decoherence of floating qubits due to capacitive coupling, New Journal of Physics **11**, 033030 (9pp) (2009).

[7] F. Yoshihara, Y. Nakamura, and J. S. Tsai, Correlated flux noise and decoherence in two inductively coupled flux qubits, Phys. Rev. B **81**(13), 132502 (2010).

[8] E. M. Purcell, Proceedings of the American Physical Society, Phys. Rev. **69**, 674 (1946).

Chapter 7

Qubit state detection with an AC-driven SQUID

In this chapter we discuss the AC-driven DC-SQUID as a qubit state detector. The most common detection method for superconducting qubits involves switching a DC-SQUID from its superconducting state to a voltage-state (see Section 2.4). This is however a rather destructive measurement type, as the switched state of the SQUID generally leads to dissipation and heating of the environment of the qubit. An alternative method, which we refer to as *bifurcation readout*, uses the SQUID as a flux-dependent non-linear inductor in a resonant circuit [1, 2]. This scheme is also referred to as a Josephson Bifurcation Amplifier. When driven slightly below its resonance, this resonator is bistable, with a switching rate between the two oscillatory states that depends on the resonance frequency, and thus on the flux sensed by the SQUID. This detection type can be used with different qubit types and has demonstrated high fidelity, low back-action and quantum nondemolition readout [3, 4, 5].

In Section 7.1 and 7.2 we discuss the theoretical model describing the detector circuit and the procedure for qubit state detection. Section 7.3 presents the experimental setup that was built for the readout of a single-, and a coupled-qubit system.

7.1 Non-linear dynamics of an AC-driven SQUID

The symmetric DC-SQUID with low self-inductance can be described as a single Josephson junction with flux-dependent critical current:

$$I_{c,sq}(\Phi_{\rm sq}) = 2I_{c0}\left|\cos\left(\pi\frac{\Phi_{\rm sq}}{\Phi_0}\right)\right|, \tag{7.1}$$

with I_{c0} the critical current of the junctions, and $\Phi_{\rm sq}$ the magnetic flux penetrating the SQUID loop. A Josephson junction has an effective inductance which can be derived from the Josephson relations:

$$I_J = I_c\sin(\varphi) \tag{7.2}$$

$$V_J = \frac{\Phi_0}{2\pi}\dot{\varphi}. \tag{7.3}$$

Eliminating the phase φ gives

$$V_J = \frac{\Phi_0}{2\pi}\frac{1}{\sqrt{I_c^2 - I_J^2}}\dot{I}_J, \tag{7.4}$$

which shows that the junction has an inductance described by

$$L_J = \frac{\Phi_0}{2\pi}\frac{1}{\sqrt{I_c^2 - I_J^2}}. \tag{7.5}$$

Note that L_J increases if I_J approaches I_c. For a SQUID the critical current $I_{c,\rm sq}$ is flux dependent, and consequently the Josephson inductance L_J is flux dependent. This property lies at the heart of the "inductive readout" method [1, 6], and forms an alternative for the DC-switch readout method that involves switching the SQUID to a finite-voltage state (Section 2.4). In Fig. 7.1 the flux dependence of the critical current $I_{c,\rm sq}$ and Josephson inductance L_J are shown.

To measure changes in the SQUID's inductance, the SQUID is shunted with a capacitor (C), together forming a resonant circuit. A schematic drawing of the circuit is shown in Fig. 7.2. The inductance L_s represents the linear inductance of the lines connecting the SQUID to the capacitor, and the resistance R the losses in the circuit. The latter is in practice dominated by the 50Ω impedance of the transmission lines from which the circuit is driven. For low driving amplitudes (i.e. $I_J \ll I_c$) the SQUID behaves as a linear inductor, in which case the system is a simple parallel LRC-resonator, with resonance frequency

$$\omega_0 = \frac{1}{\sqrt{(L_s + L_J)C}}, \tag{7.6}$$

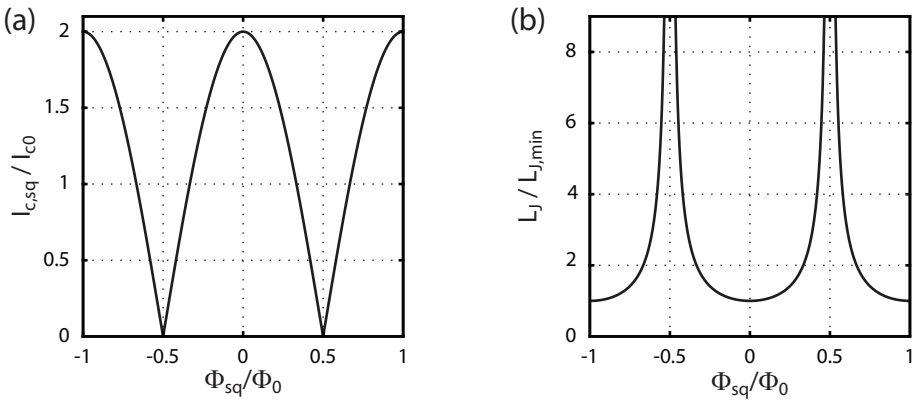

Figure 7.1: Critical current $I_{c,\mathrm{sq}}$ (a) and Josephson inductance L_J (b) of a DC-SQUID as a function of the flux Φ_{sq} penetrating the loop. The maximum critical current of the SQUID is twice the critical current I_{c0} of the junctions. The Josephson inductance has a minimum $L_{J,\mathrm{min}}$ where the critical current has a maximum, and diverges where the critical $I_{c,\mathrm{sq}} = 0$.

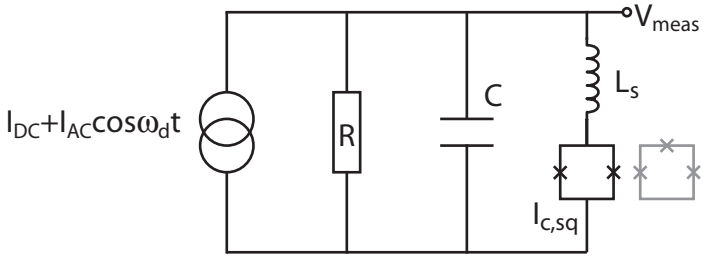

Figure 7.2: Circuit diagram of the SQUID embedded in a resonant circuit. The resonance frequency depends on the effective inductance of the SQUID, which is determined by the flux penetrating the loop and the DC offset current I_{DC}. The resistance represents the losses in the circuit, and is in practice dominated by the 50 Ω impedance of the control lines.

and damping described by the quality factor

$$Q = \omega_0 RC. \tag{7.7}$$

Probing the resonance frequency at low driving amplitudes can be used to continuously monitor a qubit state, as discussed by Lupascu *et al.* [2] and demonstrated experimentally by Palacios-Laloy *et al.* [7]. In our current work we are however mainly interested in the high driving regime.

To study the circuit behaviour at higher driving amplitudes, we apply Kirchhoff's laws to the different nodes of the circuit, and find the differential equation that describes the circuit's dynamics [8]:

$$\ddot{\varphi}_J + \frac{1}{Q}\dot{\varphi}_J + \frac{\sin\varphi_J}{1 + s\cos\varphi_J}\left(1 + s + s\dot{\varphi}_J^2\right) = \frac{1+s}{1+s\cos\varphi_J}\left(i_{AC}\cos\Omega\tau + i_{DC}\right), \tag{7.8}$$

where $i_{AC,DC} = I_{AC,DC}/Ic$, $\Omega = \omega_d/\omega_0$, and $s = L_s/L_J$. In this equation, the dimensionless time $\tau = \omega_0 t$ is normalized with the resonance frequency, and the dot denotes the derivative to the scaled time τ. The equation is exact, but can only be solved numerically. We can simplify this equation to a well known form by expanding the phase φ of the total inductance $L = L_J + L_s$. In this case the current-phase relation in the inductance branch is given by

$$I(\varphi) \approx \frac{\Phi_0}{2\pi L}\left(\varphi - \frac{1}{6(1+s)^3}\varphi^3\right), \tag{7.9}$$

which results in the differential equation for the dynamics of φ

$$\ddot{\varphi} + \frac{1}{Q}\dot{\varphi} - \frac{1}{6(1+s)^3}\varphi^3 = (1+s)(i_{DC} + i_{AC}\cos\Omega\tau). \tag{7.10}$$

This equation has the form of the Duffing oscillator, and is well known in nonlinear dynamics [9, 10].

In Figure 7.3(a) we calculated the amplitude response of this system for different driving powers, using the method described by Dykman [11]. For the lowest driving powers the response is equivalent to a linear resonator. At higher driving powers the response becomes asymmetric, bending towards lower frequencies. At the highest driving powers the system has three solutions, two of which are stable. The bistability occurs for certain combinations of driving power i_{AC} and frequency detuning $\delta\Omega = \Omega - 1$. The boundaries of this region are given by [11]

$$\delta\Omega \leq \frac{\sqrt{3}}{2Q} \tag{7.11}$$

$$i_{AC}^2 = \frac{128}{27}(1+s)\Omega^3\left(\delta\Omega^3 + \frac{9}{4Q^2}\delta\Omega \mp \left(\delta\Omega^2 - \frac{3}{4Q^2}\right)^{3/2}\right). \tag{7.12}$$

These boundaries are shown in Figure 7.3(c). In the following section we discuss how this bistability is used for qubit state detection.

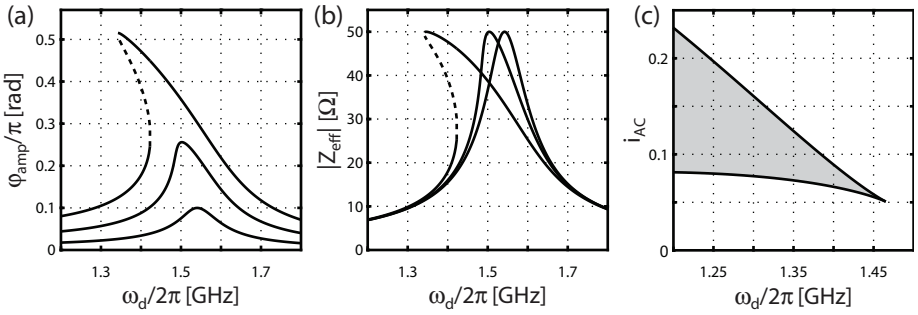

Figure 7.3: (a) Oscillation amplitude $\varphi_{\rm amp}$ as a function of the driving frequency ω_d for three different driving powers $i_{\rm AC} = 0.017, 0.042, 0.076$. For the calculations we used $I_{c,\rm sq} = 1.18$ μA, $i_{\rm DC} = 0$, $s = 0.19$, $C = 33$ pF, $R = 50$ Ω. For these parameters the linear resonance frequency is $\omega_0/(2\pi) = 1.54$ GHz. (b) Absolute value of the effective impedance $Z_{\rm eff}$ of the resonator circuit, calculated from the voltage response $V_{\rm meas} = (\Phi_0/2\pi)\dot{\varphi}$ and the corresponding driving current $I_{\rm AC}$. (c) Stability diagram of the SQUID resonator as a function of the driving amplitude $i_{\rm AC}$ and the driving frequency ω_d. The gray area indicates the driving conditions for which the circuit is bistable.

7.2 Qubit state detection scheme

The bifurcation of the oscillatory states of the SQUID circuit is a hysteretic process, which is an attractive property for qubit state detection [1]. The detection of the qubit state can be optimized reasonably separately from the detection of the detector state. Fast measurement within the relaxation of the qubit, and long integration time for sufficient signal-to-noise ratio are two central, but opposing requirements for qubit state detection. In a hysteretic detector these two properties can be conveniently separated.

The resonant circuit of Fig. 7.2 has a resonance frequency that depends on the flux penetrating the SQUID loop. In Fig. 7.4(a) the stability diagram of the circuit is shown for two different values $\Phi_{\rm sq}$, which differ by the flux corresponding to a qubit state-change, calculated for typical parameters. For a driving field with fixed frequency and increasing amplitude, the probability for switching from the low-amplitude state l to the high-amplitude state h increases dramatically close to the high boundary of the stability diagram. The switching probability is given by $P_{\rm sw} = 1 - e^{-\Gamma_{\rm sw}t}$, where $\Gamma_{\rm sw}$ is the switching rate and t is the duration of driving. The switching rate $\Gamma_{\rm sw}$ is calculated according to the model by Dykman [11]. Figure 7.4(b) depicts the switching probability $P_{\rm sw}$ for switching from l to h (solid lines) and h to l (dashed lines). The driving frequency is as indicated by

the dashed line in panel (a), and $t = 10$ ns. The significant offset between the dashed and the solid lines clearly demonstrates the hysteretic behaviour.

The pulse scheme for the operation of the detector is given in Fig. 7.4(c). The first part of the driving pulse has an amplitude A, which gives a high probability to switch from l to h if the qubit is in one state, and a low switching probability if the qubit is in the other state (see panel (b)). The second part of the pulse has a reduced amplitude B, for which the switching rates from l to h and from h to l are negligible for both qubit states, effectively freezing the state of the detector. The state can be maintained as long as necessary to discriminate the two detector states.

Previous experiments have shown that this readout scheme provides a quantum nondemolition type of measurement, and a readout fidelity of $\approx 90\%$ has been achieved [4]. In the next section we discuss the experimental setup that implements this method for a single- and two-detector experiment.

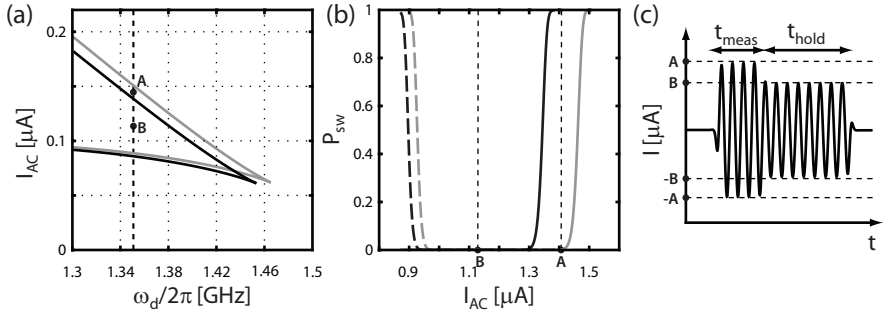

Figure 7.4: (a) Stability diagram of the SQUID resonator circuit, calculated for two values of the flux $\Phi_{\rm sq}$ that differ by the flux corresponding to a qubit state-change. The circuit parameters are as in Fig. 7.3, with $I^g_{c,\rm sq} = 1.179$ μA and $I^e_{c,\rm sq} = 1.158$ μA the critical currents of the SQUID for the qubit in the ground and excited state respectively. These values correspond to a SQUID with maximal critical current $I_{c,\rm sq,max} = 1.94$ μA, a bias point of $\Phi_{\rm sq}/\Phi_0 = 0.286$, a qubit with persistent current $I_p = 500$ nA and a mutual inductance of $M = 10$ pH. (b) Switching probabilities $P_{\rm sw}$ of the resonator from the low to the high amplitude state (solid lines) and vice versa (dashed lines). The black and grey lines are for two different qubit states, as described in (a). A pulse duration of $t = 10$ ns was used. (c) Pulse shape for the operation of the resonator circuit as a flux detector. The first part of the pulse of duration $t_{\rm meas}$ and amplitude A is such that $P_{\rm sw}$ is high for the qubit in one state, and low in the other. The second part of the pulse has a duration $t_{\rm hold}$ and a reduced amplitude B. At these settings the switching probability in either direction is negligible for both qubit states.

7.3 Experimental Setup

7.3.1 Single Detector

The experimental setup for the bifurcative SQUID detectors is drawn in Figure 7.5. An arbitrary waveform generator (Tektronix AWG520) and mixer are used to create the desired AC pulse shape from the continuous-wave signal generator (HP 8657 B) (see Fig. 7.4(c)). This signal is attenuated −20 dBm at 4 K and −30 dBm at the base temperature stage (≈ 30 mK) (not shown). To further decrease the effective noise temperature for low frequencies, a high-pass filter (880 MHz) is used to further suppress the spectral density below the frequency-band used for detector operation (1 − 2 GHz) (not shown).

The AC pulse is reflected at the resonator. In the reflection it picks up a phase that depends on the oscillatory state of the resonator (l, h). The reflected signal propagates back along the same line, where it is separated from the incoming signal with a microwave circulator. The outgoing signal is amplified at the 4K stage (Quinstar Tech. Inc. QCA-L1, Gain 40 dB, Tn=4K), and post-amplified at room-temperature (Kuhne LNA 1020A). Next the signal is split and both paths are down-mixed with the original microwave signal, one of which is 90° phase shifted. The resulting signals Q1 and Q2 contain DC and double-frequency components, of which the double-frequency components are removed using low-pass filters (30 MHz). This low-pass filter determines the response bandwidth of the system. The DC voltage levels of the down-mixes signals are measured with a 100 MHz 8-bit digitizer. The two values combined provide the phase and amplitude information of the reflected signal.

The reflection of the AC-pulse at the resonator is given by the reflection coefficient

$$\Gamma = \frac{Z - Z_0}{Z + Z_0} \tag{7.13}$$

where Z is the impedance of the circuit for a given oscillatory state, and $Z_0 = 50\,\Omega$ is the impedance of the coaxial connection lines. The effective impedance of the SQUID circuit is different for state l and h, as shown in Fig. 7.3(b). For both resonator states $|\Gamma| = 1$, as the resonator impedance is ideally fully imaginary, but the phase of the reflected signal is different for the two cases. This phase difference translates to a change of the measured DC voltages of the down-mixed signals. Using a phase-shifter (see Fig. 7.5) this voltage difference can be optimized for one of the two outputs Q1 or Q2. In this case the discrimination of the two phases can be conveniently performed on a single output channel.

Figure 7.6 shows a measurement of the phase-response of a detector circuit as a function of the driving frequency of a continuous driving signal, and for various driving powers. This measurement was performed using a network analyzer,

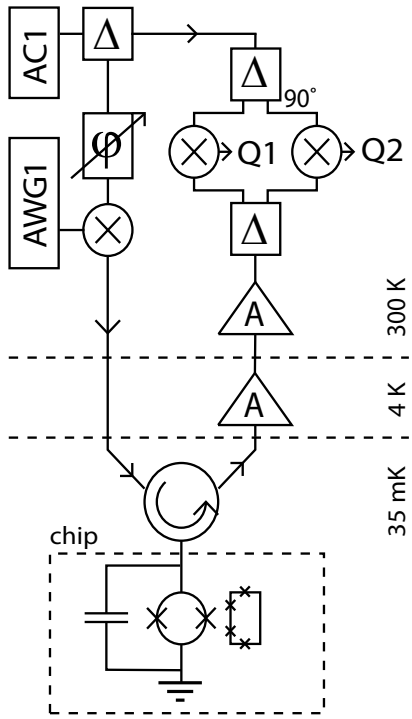

Figure 7.5: Schematic drawing of the setup for bifurcation readout. An Arbitrary Waveform Generator (AWG1) and a mixer are used to create the pulse shape of Fig. 7.4(c) from the continuous wave signal generated by generator AC1. A microwave circulator directs the input AC pulse to the SQUID resonator circuit, and the reflected signal to the output circuit. In the output line the signal is amplified with a cryogenic amplifier, and post-amplified at room temperature. The signal is split and down-mixed with two quadratures of the original continuous wave signal from AC1.

connected directly to the input and output line of the circuit. For the highest driving powers the response shows a sharp step, which is the signature of the circuit bifurcation. For this device $I_{c,\mathrm{sq,max}} \approx 2.0\ \mu$A, $C = 31$ pF, $Ls \approx 70$ pH.

In the experiments depicted in Figure 7.7 the SQUID is operated close to such a bifurcation point, with a pulse shaped as shown in Fig. 7.4(c). Figure 7.7(a) demonstrates the resulting statistics of 32768 individual measurements. This result demonstrates that the two different oscillatory states of the circuits can be very well separated for relevant operation parameters ($t_{\mathrm{meas}} = 20$ ns, $t_{\mathrm{hold}} = 300$ ns). The frequency and amplitude are calibrated such that the probability for the circuit to switch to the high amplitude state is $P_{\mathrm{sw}} \approx 50\%$. Figure 7.7(b) depicts the switching probability P_{sw} as a function of an external applied magnetic flux Φ_{sq}. The sensitivity of the switching probability is equivalent to $\approx 85\%$ qubit state separation for a qubit with $I_p = 500$ nA and mutual inductance $M = 10$ pH.

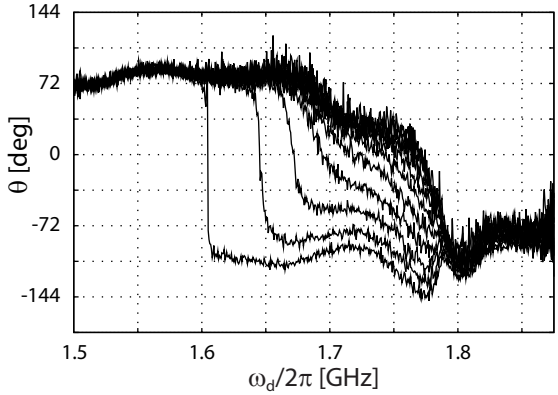

Figure 7.6: Measured phase θ of the reflected signal, as a function of the driving frequency ω_d. The driving power for the individual curves differ by 1 dB. For the lowest driving powers, at the top side of the graph, the phase response does not depend on the power, and drops $\approx 180^\circ$ at 1.75 GHz. At the highest power the phase makes a sharp step, indication the jump from one oscillatory state to the other.

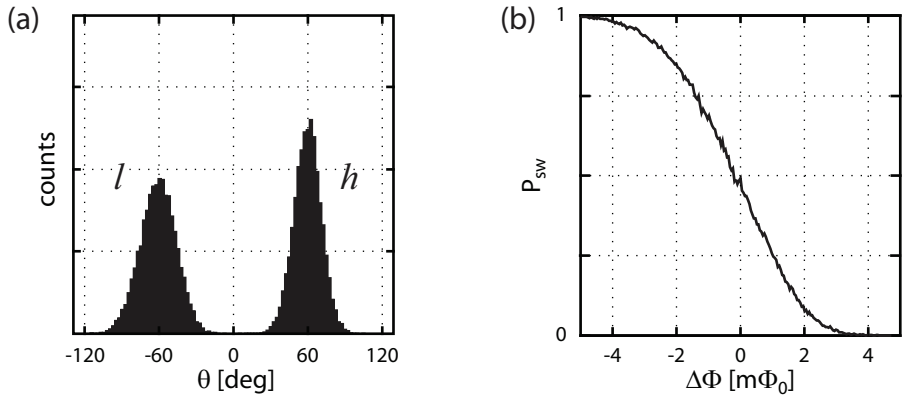

Figure 7.7: (a) Switching histogram showing the statistics of the phase θ for 32768 individual reflection measurements. The measurement pulse is calibrated for a probability of $P_{\rm sw} \approx 50\%$ for switching from the low to the high amplitude state. (b) Sensitivity of $P_{\rm sw}$ on an externally applied magnetic flux Φ. This sensitivity corresponds to $\approx 85\%$ qubit state separation for a qubit with $I_p = 500$ nA and $M = 10$ pH ($\Delta\Phi = 5$ mΦ_0).

7.3.2 Two Detectors

For the independent readout of two coupled flux qubits we equipped each qubit with a separate SQUID resonator circuit, and off-chip circuitry as drawn in Fig. 7.8. The resonators are designed to differ at least 100 MHz in resonance frequency. This is to minimize on-chip cross-talk between the two detectors, and to enable frequency multiplexing of the detection signals.

The simplest implementation of a two-detector experiment is to copy the single detector setup as depicted in Fig. 7.5, and have two fully independent detector circuits. Because of the limited space in a dilution-refrigerator, and to reduce the heat load on the system, it is attractive to implement multiplexing of the detection signals.

In our setup we combine the outgoing signals, so a single cryogenic amplifier can be used. As we use frequency to multiplex the two signals, both detectors can be operated simultaneously. This approach has two main consequences. First, the required combiner before the cryogenic amplifier gives an extra ≈ 3.5 dB reduction of the signal, which translates directly to longer integration times for the same signal-to-noise ratio. This extra integration time makes this multiplexing scheme less favorable for fast repeated measurements with the same detector, which is for instance used to analyze the post-measurement state of a qubit. Second, the frequencies of the two detectors need to be separated at room temperature. This separation requires no extra elements in the circuit, as the detection scheme has already two mechanisms that provide the signal separation. Before the signal is mixed down, it contains both frequencies f_1 and f_2. Focussing on the signal of detector 1, the signal is down-mixed with frequency f_1. This down-mixed signal contains 4 frequency components: $f = (f_1 - f_1) = 0$, $f = (f_1 + f_1) = 2f_1$, $f = |f_1 - f_2|$ and $f = f_1 + f_2$. All the non-zero frequency components are filtered out by the low-pass filters of $f_{LP} = 30$ MHz $> |f_1 - f_2| \geq 100$ MHz. Additionally, for integration times $> 1/(f_1 - f_2) \approx 10$ ns, and the frequency difference not an exact multiple of the sampling frequency, the DC contribution of the remaining oscillating components is mostly averaged out.

The input signals could also be multiplexed. In this case the demultiplexing needs to be done at the lowest temperatures, which requires sharp filters. This is only convenient if there is sufficient space at the lower temperatures for the required filters and splitters, and the number of transmission lines to room temperature is limited. This was not the case in the experiments presented here.

The intrinsic separation of the two detector signals makes the operation of the multiplexed setup exactly the same as a setup without multiplexing, which is simply twice the procedure for a single-detector device. The measurements depicted in Fig. 7.6 and 7.7 are both performed on a two-detector device, and both detectors showed similar performance over a number of devices. The maximum flux sensitivity corresponded to $\approx 90\%$ qubit state separation, however actual

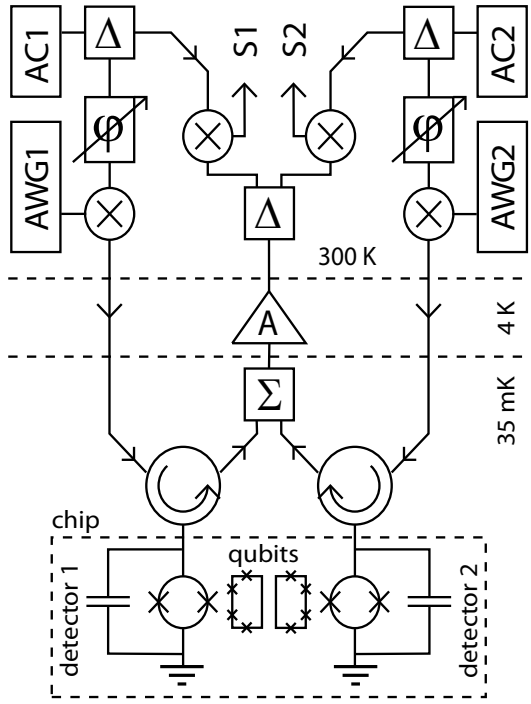

Figure 7.8: Schematic drawing of the experimental setup for double bifurcation readout. The input lines for both detectors are copies of the single-detector setup of Fig. 7.5. The output of both detectors is combined using a microwave combiner, so a single cryogenic amplifier can be used for both signals. At room temperature the signal is split, and each branch is down-mixed with one of the driving signals. The signals S1 and S2 are filtered with a low-pass filter to remove all the non-zero frequency components, which also removes the signal of the other detector. Note that S1 and S2 each represent only one of the two quadratures Q1 and Q2 of Figure 7.5, because one quadrature is sufficient for the detection scheme. In practice, however, both quadratures were present.

qubit measurements have never yielded fidelities higher then 50%. The reduced contrast is expected to be mainly caused by relaxation of the qubit. This reduced decoherence could be partially caused by the detection process, but could also be caused by other decoherence processes. Measurements in this direction have not yet yielded conclusive results.

The most interesting part of the double-detection scheme is the possible cross-talk of the measurements. Qubit related cross-talk is relatively easy to predict. The mutual inductance of one qubit to the detector of the other qubit can be easily calculated, and is not hard to design well below 1 %. Mixing of the eigenstates of the qubits due to the coupling leads to finite contributions of $\langle I_{p,1} \rangle$ or $\langle I_{p,2} \rangle$ in states that are usually labeled by the closest non-coupled eigenstate (see Chapter 3). This contribution is however suppressed when the levels are not close to any anti-crossing. The qubits can also contribute to cross-talk if the qubits exchange population, which can result from the large modulation of the detuning of the two qubit states caused by the detector driving signals. This problem can be avoided if the readout position of the qubits ensures that the difference in qubit splittings is larger than the modulation of the qubit states.

The hardest to predict is the direct detector-detector crosstalk. The switching between the high- and low-amplitude states comprises involved non-linear dynamical processes. In the next chapter we analyze this crosstalk experimentally.

Bibliography

[1] I. Siddiqi, R. Vijay, F. Pierre, C. M. Wilson, M. Metcalfe, C. Rigetti, L. Frunzio, and M. H. Devoret, RF-Driven Josephson Bifurcation Amplifier for Quantum Measurement, Phys. Rev. Lett. **93**, 207002 (2004).

[2] A. Lupasşcu, *Inductive readout for a superconducting flux qubit*, Ph.d. thesis, Delft University of Technology, 2005.

[3] I. Siddiqi, R. Vijay, M. Metcalfe, E. Boaknin, L. Frunzio, R. J. Schoelkopf, and M. H. Devoret, Dispersive measurements of superconducting qubit coherence with a fast latching readout, Phys. Rev. B **73**, 054510 (2006).

[4] A. Lupaşcu, S. Saito, T. Picot, P. C. de Groot, C. J. P. M. Harmans, and J. E. Mooij, Quantum non-demolition measurement of a superconducting two-level system, Nature Physics **3**, 119–125 (2007).

[5] F. Mallet, F. Ong, A. Palacios-Laloy, F. Nguyen, P. Bertet, D. Vion, and D. Esteve, Single-shot qubit readout in circuit quantum electrodynamics, Nature Physics **5**, 791–795 (2009).

[6] A. Lupaşcu, C. J. M. Verwijs, R. N. Schouten, C. J. P. M. Harmans, and J. E. Mooij, Nondestructive Readout for a Superconducting Flux Qubit, Phys. Rev. Lett. **93**(17), 177006 (2004).

[7] A. Palacios-Laloy, F. Mallet, F. Nguyen, P. Bertet, D. Vion, D. Esteve, and A. N. Korotkov, Experimental violation of a Bell's inequality in time with weak measurement, Nat. Phys. **Published online: 18 April 2010** (2010).

[8] E. Driessen, Nonlinear dynamics of the inductive SQUID: propspects for qubit measurement, Master thesis, Delft University of Technology, 2005.

[9] L. D. Landau and E. M. Lifshitz, *Mechanics*, volume 1 of *Course of Theoretical Physics*, Pergamon Press, 1960.

[10] A. Blaquière, *Nonlinear system analysis*, Academic Press, 1966.

[11] M. I. Dykman and M. A. Krivoglaz, Fluctuations in Nonlinear Systems Near Bifurcations Corresponding to the Appearance of New Stable States, Physica A **104**, 480 (1980).

Chapter 8

Low-crosstalk bifurcation detectors for coupled flux qubits

We present experimental results on the crosstalk between two AC-operated dispersive bifurcation detectors, implemented in a circuit for high-fidelity readout of two strongly coupled flux qubits. Both phase-dependent and phase-independent contributions to the crosstalk are analyzed. For proper tuning of the phase the measured crosstalk is 0.1 % and the correlation between the measurement outcomes is less than 0.05 %. These results show that bifurcative readout provides a reliable and generic approach for multi-partite correlation experiments.

8.1 Introduction

Dispersive bifurcation detectors [1] have proven to be well suited for single-qubit state detection in superconducting devices [2]. High fidelity, low back-action, and quantum nondemolition readout have been reported [3, 4, 5]. An expansion to multiple qubits and detectors is the obvious next step. This introduces additional requirements, such as sufficiently low direct detector-detector interaction to avoid measurement crosstalk [6]. Low crosstalk is important for all experiments that rely on measurement correlations, such as detecting entanglement.

We quantitatively analyze the crosstalk between two simultaneously operated bifurcative flux detectors, each attached to a flux qubit [7]. Qubits 1 and 2 are characterized by their persistent current $I_{p,1} = 540$ nA and $I_{p,2} = 470$ nA and energy gap $\Delta_1/h = 2.1$ GHz and $\Delta_2/h = 4.8$ GHz. As we concentrate on the detectors only, the qubits are biased at level splittings of $\nu_1 = 7.3$ GHz and $\nu_2 = 11.1$ GHz respectively, such that their role can be disregarded. The detectors are designed for high fidelity single-shot readout, with similar design parameters as in Ref. [4]. We measure a very small crosstalk of less than 0.4 %, in spite of the close proximity of all components as required for strong inductive coupling between the two qubits (250 MHz) and between the qubits and their detectors (90 % qubit-state separability).

When a detector is driven, it can assume two classical states. The detector starts in one state and will or will not switch to the other state, depending on the sensed magnetic flux. We distinguish two types of crosstalk. If the *driving* signal for one detector directly couples to the second one, the switching probability of that detector may be affected. We call this input driving crosstalk (IDC). In addition, the switching of one detector may be influenced by the *state* of the other, leading to undesired correlation of the output states. We call this detector state crosstalk (DSC).

8.2 Experimental Setup

Each detector comprises a superconducting quantum interference device (SQUID) as the flux-sensor and a shunting capacitor (Fig. 8.1(a-c)). The flux sensed by the SQUID controls its inductance, which, combined with the capacitor, results in a resonant circuit with a flux-dependent resonance frequency. In addition, the inductance depends on the current in the SQUID, making the resonator non-linear. When it is subjected to a strong AC driving slightly below its resonance frequency, the response shows two stable states (l and h) differing by their amplitude and phase. This type of detector is often referred to as a Josephson bifurcation amplifier [1] (see also Chapter 7). The capacitors of the

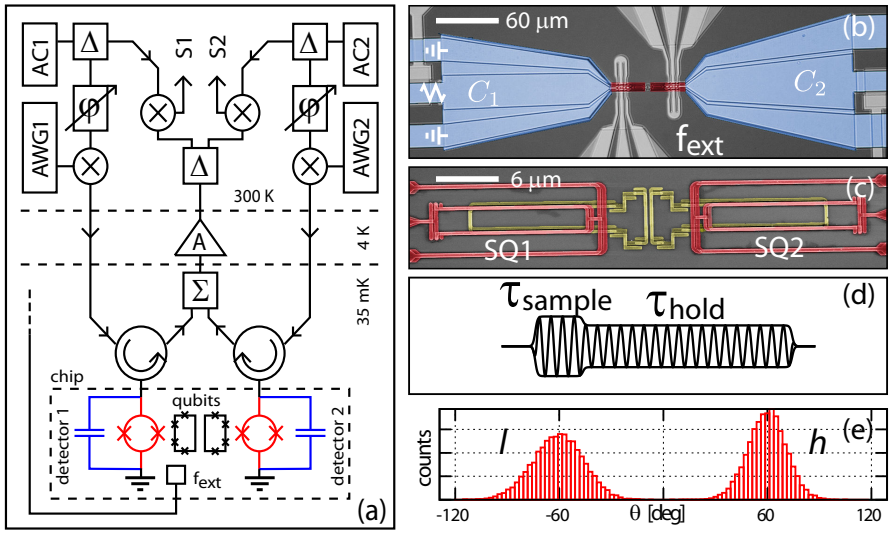

Figure 8.1: (a) Schematic representation of the readout circuit. (b) Optical microscope picture showing the on-chip capacitors (C_1 = 31 pF, C_2 = 40 pF) and two antennas for external driving. (c) Scanning electron micrograph showing the two SQUID loops. These loops are 10.7×2.0 μm^2 with a mutual inductance of $M_{sq-sq} = 5$ fH. Each SQUID covers partially one of the two coupled qubits, with $M_{sq-qb} = 10$ pH and $M_{qb-qb} = 0.76$ pH. The resonator loops have a mutual inductance of $M_{res,1-res,2} = 1$ fH. The couplings of the resonator loops to the SQUID and qubit loops are minimized by the symmetry of the design. The maximum critical current of each SQUID is $I_{c,max} \approx 2.0$ μA. The experiment is performed at the flux operating point $\Phi/\Phi_0 = 2.67$. (d) Shape of the AC readout burst. (e) The histogram shows the statistics of the phase θ picked up at the reflection of 32768 individual measurements. The two oscillator states can clearly be distinguished.

two detectors are chosen such that their resonance frequencies differ by ~ 10 %.

Each detector is operated in the same way as in a single qubit experiment. The driving signals are generated using AC-sources AC1 and AC2 and shaped into two-level bursts using mixers and arbitrary waveform generators AWG1 and AWG2 (see Fig. 8.1(a,d)). The first part of the burst of duration τ_{sample} is where the actual qubit state measurement would take place. The driving amplitude is such that the resonator has a significant probability to switch from its initial low amplitude state l to the high amplitude state h. The switching probability from l to h strongly depends on the resonance frequency, and therefore on the flux sensed by the SQUID loop. The second part of the burst has a reduced amplitude and a duration τ_{hold}. At this driving amplitude the probabilities for switching from l to h and from h to l are negligible. The resonator state is effectively frozen, which provides the required time to integrate the signal for the desired signal-to-noise ratio. A pulse shape was used with $\tau_{sample} = 20$ ns and $\tau_{hold} = 300$ ns.

The applied AC burst is fully reflected at the resonator. In the reflection, a phase is picked up that depends on the state of the resonator; this phase is measured to distinguish the resonator states. Before arriving at the resonator, the burst has passed several stages of attenuation for thermalization (not shown), a band-pass filter (not shown), and a circulator. The reflected signals of both detectors pass again through the circulators, are combined, amplified (Quinstar Tech. Inc. QCA-L1, Gain = 40 dB, Tn = 4 K, f = 1.25-1.75 GHz), split up again at room temperature, and down-mixed with the original AC-signals. The multiplexing of the output signal significantly reduces the heat load and space required in the cryogenic setup. Since the down-mixed signals S1 and S2 contain multiple frequencies of both detectors, 30 MHz low-pass filters are used to extract the desired DC components. The level of this signal, which is a measure of the phase picked up in the reflection, is recorded with a 100 MHz, 8-bit digitizer. The phase shifters (Fig. 8.1(a)) are adjusted to obtain the maximum discrimination of the two oscillator states in the down-mixed signal. Fig. 8.1(e) shows the result of 32768 measurements of the state of one of the oscillators for 50 % switching probability; it clearly demonstrates the good separation of the two associated phases.

8.3 Experiment 1: The effect of an oscillating field on the detectors

Before we proceed to quantify the crosstalk between the detectors, we discuss an experiment that qualitatively shows the effect of an external oscillating field on the detectors. The resonators are continuously driven by a nearby antenna (f_{ext} in Fig. 8.1(a,b)) that generates a field in the detectors that has at least 100x higher

amplitude than is expected from the detector-detector crosstalk. The frequency f_{ext} is varied; for each frequency the probability $P(h)$ of switching to state h is determined from 4096 measurements. The result is shown in Fig. 8.2. From this graph two types of response can be distinguished. The first shows up as a broad peak at the resonance frequencies $f_{\mathrm{res},1} = 1.47$ GHz and $f_{\mathrm{res},2} = 1.32$ GHz of the resonators. We attribute this effect to excitation of the resonator, which is consistent with the increased probability for switching to state h. The second effect can be seen in the regions around the detector driving frequencies $f_1 = 1.36$ GHz and $f_2 = 1.26$ GHz. In a region of approximately 100 MHz wide, and when f_{ext} is an exact multiple of the measurement repetition frequency $f_{rep} = 1/\tau_{rep} = 1/22.2\ \mu\mathrm{s}^{-1}$, the probability of switching varies drastically, ranging almost from 0 to 1. This effect is attributed to interference of the detector driving current with the externally applied field from the antenna. If the frequency difference $|f_i - f_{ext}|$ is small compared to $1/\tau_{sample} = 50$ MHz they remain effectively phase correlated during each single measurement and the contributions add up, enhancing or reducing $P(h)$ depending on their phase difference. Note that qubit operation pulses would not induce this interference, as they are well separated in time and frequency from the readout pulses. These results clearly demonstrate effects of an AC-field, including the role of the phase. With this in mind we proceed to quantify the detector-detector crosstalk.

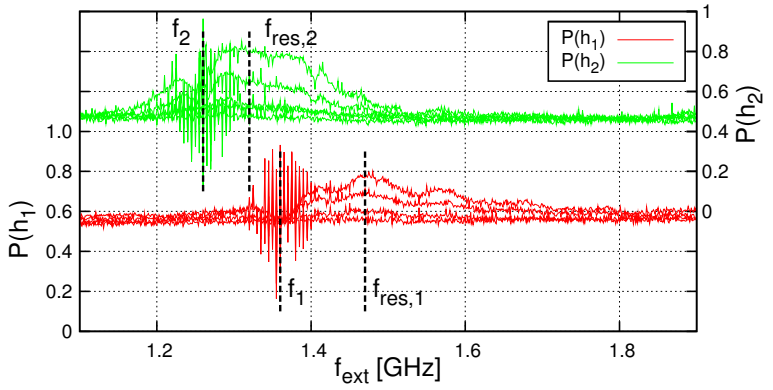

Figure 8.2: Switching probability for detector 1 and 2 as a function of the driving frequency of the externally applied field. Individual curves differ 4 dB in driving power. The dashed lines indicate the driving frequency f_i and resonance frequency $f_{\mathrm{res},i}$ for each detector.

8.4 Experiment 2: Phase-independent crosstalk

We first investigate the phase-independent components of the crosstalk. The probability $P(h_i)$ that detector i switches to state h is determined two times, each from 32768 individual measurements. The first time detector j is not driven (OFF_j) and the second time it is driven and read out with a regular readout pulse (ON_j), providing also $P(h_j)$. This sequence is repeated 10000 times. Since the detectors are operated at different frequencies, we define the relevant phase $\Delta\phi$ as the phase-difference between the two AC-signals at the start of each measurement. We choose the driving frequencies $f_1 = 1.37009999$ GHz and $f_2 = 1.26$ GHz and the repetition time $\tau_{rep} = 22.2$ μs. This leads to a uniform distribution of $\Delta\phi$ over the 32768 measurements. In a separate experiment, it was verified that for a single detector the phase of the driving-signal does not influence the measurement outcome. We determine the IDC, quantified as:

$$\Delta P_{\mathrm{IDC},1}(i,j) = P(h_i;\mathrm{ON}_j) - P(h_i;\mathrm{OFF}_j) \tag{8.1}$$

where $P(h_i;\mathrm{ON}_j)$ and $P(h_i;\mathrm{OFF}_j)$ are the switching probabilities of detector i for the cases that detector j is ON and OFF respectively. The results are shown in Fig. 8.3(a). We find very small crosstalk, $\langle \Delta P_{\mathrm{IDC},1}(1,2)\rangle = 0.10$ % and $\langle \Delta P_{\mathrm{IDC},1}(2,1)\rangle = 0.13$ %; $\langle\rangle$ denotes the average over the 10000 repetitions. The IDC from detector one to two is slightly higher then vice-versa; this is consistent with the picture that the crosstalk causes an additional excitation and $|f_1 - f_{\mathrm{res},2}| < |f_2 - f_{\mathrm{res},1}|$. A separate analysis of the data showed no significant increase of the width of the distribution for detector i if detector j is ON.

The DSC is quantified as:

$$\Delta P_{\mathrm{DSC}}(i,j) = P(h_i|l_j) - P(h_i|h_j) \tag{8.2}$$

where $P(h_i|l_j)$ and $P(h_i|h_j)$ are the conditional probabilities for finding detector i in the high state given that detector j was in the low or high state respectively. For this we only use the data where both detectors were ON. The results are shown in Fig. 8.3(b). We find $\langle \Delta P_{\mathrm{DSC}}(1,2)\rangle = 0.07$ % and $\langle \Delta P_{\mathrm{DSC}}(2,1)\rangle = 0.08$ %. Again the crosstalk is very small. In both cases the DSC is positive, implying that the switching probability is decreased if the other detector switches.

8.5 Experiment 3: Phase-dependent crosstalk

In the last experiment we measure the average switching probability as a function of $\Delta\phi$. Now we choose the driving frequencies $f_1 = 1.37$ GHz and $f_2 = 1.26$ GHz to be multiples of the repetition frequency $f_{rep} = 1/\tau_{rep} = 1/22.2$ $\mu\mathrm{s}^{-1}$, so that $\Delta\phi$ is constant within a sequence of measurements. We change $\Delta\phi$ from

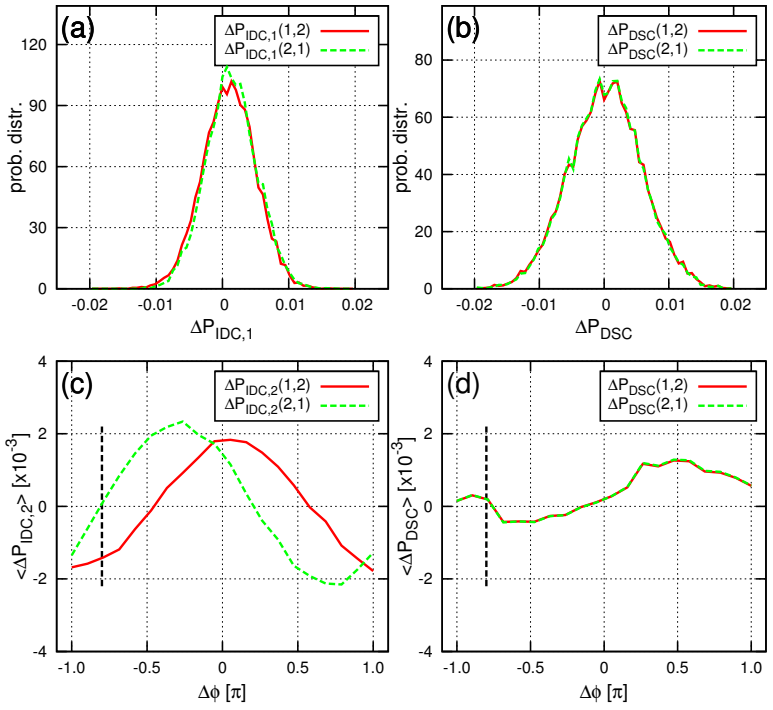

Figure 8.3: (a) The probability distribution for the measured Input Driving Crosstalk. The crosstalk shows as a shift of the center of the histograms: the average switching probability is changed by 0.10 % and 0.13 % for detector 1 and 2, respectively, if the other detector is operated. (b) The probability distribution for the Detector State Crosstalk. The average switching probability differs by 0.07 % and 0.08 % for detector 1 and 2, respectively, for the two different outcomes of the other detector. (c) The IDC as a function of the phase difference $\Delta\phi$ between the two AC-driving-signals. (d) The DSC as a function of $\Delta\phi$. The dashed vertical lines indicate the phase setting with favorable crosstalk for the total IDC and the DSC combined.

$-\pi$ to π in 20 steps by changing the phase of AC2; this is repeated 5000 times. The switching probability is determined from 16384 individual measurements. To ensure phase stability of the phase-locked AC-sources during the time of the experiment ($\sim$ 48 hours), the phases are monitored by sampling the driving signals. The phases are checked after each phase-change giving a maximum phase-error of ± 5 degrees. The trigger-jitter of the AWG that generates the envelope is 50 ps (RMS). Because in this experiment both detectors are always ON, we now redefine the IDC relative to its average value:

$$\Delta P_{\mathrm{IDC},2}(i,j,\Delta\phi) = P(h_i;\Delta\phi) - \langle P(h_i;\Delta\phi)\rangle_{\Delta\phi} \tag{8.3}$$

where $\langle\rangle_{\Delta\phi}$ denotes the average over all phase-differences.

The result for the IDC (Fig. 8.3(c)) shows a clear phase dependence for both detectors with an amplitude of 0.18 % for detector 1 and 0.22 % for detector 2. A prominent feature is the shift in $\Delta\phi$ of $\sim 0.3\pi$ between the two curves. This is attributed to the phase difference between the applied driving field and the internal current response of each resonator, which depends on the detuning in the employed off-resonant driving. The total IDC is obtained by adding $\langle\Delta P_{\mathrm{IDC},1}\rangle$ and $\langle\Delta P_{\mathrm{IDC},2}\rangle$; it remains below 0.4 % for both detectors and has an optimum $< 0.1\%$ indicated by the dashed line in figure Fig. 8.3(c) The DSC (Fig. 8.3(d)) also shows a phase dependence, although less distinct, with an amplitude of 0.08 % for both detectors. Here the phase dependence can be understood from the fact that a change of the resonator state changes its internal current, and thereby the field it induces in the other resonator. Depending on the phases, the change will enhance or reduce the switching of the other detector. For the DSC we do not find a shift in $\Delta\phi$ between the two detectors, which is in agreement with direct resonator-resonator interaction and no contribution of the driving signal. We observe a slight positive offset of 0.04 %, which is consistent in sign, but slightly smaller than found in the phase-independent experiment of Fig. 8.3(b).

8.6 Conclusions

In conclusion, we have demonstrated that two bifurcative flux detectors strongly coupled to two interacting qubits can be implemented with very small crosstalk. The crosstalk depends on the phase relation between the AC-driving signals, with a maximum of 0.4 % and an optimum of less than 0.1 %. The results indicate that this approach likely can be extended to five detectors per octave amplifier bandwidth. Furthermore, the smaller size of lumped-element resonators compared to transmission-line resonators allows a compact single-chip multiple-device design. Adding moderate-Q resonators at the input side could provide multiplexing of the detector driving as well, allowing the use of one single coaxial feed line for all detectors.

Bibliography

[1] I. Siddiqi, R. Vijay, F. Pierre, C. M. Wilson, M. Metcalfe, C. Rigetti, L. Frunzio, and M. H. Devoret, RF-Driven Josephson Bifurcation Amplifier for Quantum Measurement, Phys. Rev. Lett. **93**, 207002 (2004).

[2] J. Clarke and F. K. Wilhelm, Superconducting qubits, Nature **453**, 1031 (2008).

[3] I. Siddiqi, R. Vijay, M. Metcalfe, E. Boaknin, L. Frunzio, R. J. Schoelkopf, and M. H. Devoret, Dispersive measurements of superconducting qubit coherence with a fast latching readout, Phys. Rev. B **73**, 054510 (2006).

[4] A. Lupaşcu, S. Saito, T. Picot, P. C. de Groot, C. J. P. M. Harmans, and J. E. Mooij, Quantum non-demolition measurement of a superconducting two-level system, Nature Physics **3**, 119–125 (2007).

[5] F. Mallet, F. Ong, A. Palacios-Laloy, F. Nguyen, P. Bertet, D. Vion, and D. Esteve, Single-shot qubit readout in circuit quantum electrodynamics, Nature Physics **5**, 791–795 (2009).

[6] R. McDermott, R. W. Simmonds, M. Steffen, K. B. Cooper, K. Cicak, K. D. Osborn, S. Oh, D. P. Pappas, and J. M. Martinis, Simultaneous State Measurement of Coupled Josephson Phase Qubits, Science **307**, 1299–1302 (2005).

[7] J. E. Mooij, T. P. Orlando, L. Levitov, L. Tian, C. H. van der Wal, and S. Lloyd, Josephson Persistent-Current Qubit, Science **285**, 1036–1039 (1999).

Chapter 9

Discussion of current status and future directions

9.1 Current status

The work presented in this thesis started when the field of superconducting qubits was in an interesting transition. This transition can be considered a natural step in the evolution of a qubit. The first phase consists of proof-of-principle experiments, and aims to show that a number of requirements can be fulfilled, albeit at different conditions. For superconducting qubits there existed already a number of successful qubit implementations that could coherently be operated and read out, and the first results of experiments on coupled qubits were emerging.

Moving towards the second phase, the focus shifts towards fulfilling these basic requirements *simultaneously*, and to the integration of qubits as building blocks into more complex systems. The previous proof-of-principle demonstrations are often performed in optimised conditions for one specific goal, and are not always easily combined with other requirements. Even when fundamental properties are not conflicting, many of the "tricks" that boost the performance in a particular experiment are impossible in the combined experiments. For example, in single-qubit structures, the electrical circuits are often designed with certain symmetries, such that the circuit noise is partially suppressed. For structures of more than one qubit this is often not possible, due to the different topology of the system.

In this thesis I focus on the operation and readout of systems of two coupled qubits. The major experimental results are summarised by:

- Two flux qubits are coupled inductively, and the energy levels of the coupled

system are measured spectroscopically. Coherent oscillations are successfully induced between the states of the coupled system (Chapters 3, 4 and 5).

- Controlled-NOT quantum gates are demonstrated on two coupled flux qubits. The qubits are operated away from their degeneracy points, such that a spectroscopic splitting can be used to frequency-selectively access the individual transitions in the coupled system (Chapter 4).

- A new method is introduced and demonstrated that enables the selective excitation of degenerate transitions in systems of two coupled qubits. This method provides controlled-NOT quantum gates for transversely coupled qubits, allowing inductively coupled flux qubits to be operated at their degeneracy points where the dephasing time is optimal, and removes the necessity of elaborate refocussing techniques (Chapter 5).

- The AC bifurcative readout is extended to enable independent and simultaneous readout of two coupled flux qubits. The crosstalk between the detectors is analysed experimentally and shows a maximum of 0.4 % and an optimum of less than 0.1 % (Chapter 8).

The aim of this project was two-fold: Acquisition of full control of the state of a two-qubit system, and the simultaneous implementation of independent, low back-action and high fidelity readout of these qubits. Such a system provides the means to demonstrate well-established quantum mechanical concepts, such as a two-qubit algorithm, state- and process-tomography, and measurement of entanglement by a Bell-type experiment. It also enables more explorative experiments, such as analysing the process of measurement itself. In addition, this research forms an important step towards the implementation of systems of more than two qubits.

Although a few crucial advancements have been made, there are some obstacles that still need to be addressed. The maximum decoherence times achieved do not allow for experiments with complex pulse sequences. This is at least partly caused by the higher number of restrictions in the design of two-qubit devices in comparison to one-qubit devices. Furthermore, the best readout fidelity observed for the bifurcative detectors was 50% in the two-qubit devices, which is less than the measured detector sensitivity of 90%, and also less than the previously achieved fidelity of 87% in a single-qubit experiment. Both issues will be discussed further below, together with suggestions for improvement.

In other research groups there has also been significant progress over the last several years. Increased understanding of the decoherence processes has led to improvements in existing superconducting qubit types, as well as to the development of a number of new superconducting qubit types [1, 2]. Tunable

coupling has been realised [3] and two qubits have been coupled using a coplanar waveguide resonator acting as a bus [4, 5]. Milestone experiments such as a two-qubit quantum algorithm [6] and a Bell-type experiment have been performed [7], and the first three-qubit experiments are underway. All these experiments were performed under different conditions. In the next section I compare some of their characteristic properties and discuss if these would be attractive for adoption in a system of flux qubits.

9.2 Discussion and suggestions for improvement

For experiments that aim to combine several conflicting requirements, all design parameters tend to intertwine, such as relatively strong qubit-qubit coupling and low detector-detector crosstalk, or high-fidelity single-shot readout and long qubit coherence times. Nevertheless, I distinguish for the discussion three categories: (i) coupling and operation, (ii) decoherence and (iii) readout, and explain where these categories interact. The issue of scalability can hardly be considered a separate category, as it is fully determined by the implementation of the three categories mentioned before. Scalability will be addressed in each of the three categories.

9.2.1 Coupling and operation

In this thesis I focus on inductively coupled flux qubits. The strength of this coupling depends only on two quantities: the persistent currents of the qubits, and the mutual inductance between the loops. To achieve high coupling strength and thus fast two-qubit gates, it is usually considered attractive to employ the kinetic inductance of a shared line, or even a shared junction. The same holds for the detector circuits that require a large mutual inductance with the qubits for high-fidelity single-shot readout.

To limit the possible low-frequency current paths in the circuit, and to avoid detector-detector crosstalk, it is considered best to avoid galvanic contact between the separate circuits, thereby relying solely on geometric mutual inductance. Especially for scaling up to more than two qubits, this seems the only feasible route using SQUID based detection. The consequence is that both the qubit and detector circuits need to be relatively large compared to the alternatives based on kinetic inductance. This has implications for the qubit design, due to the non-negligible self-inductances of the qubit loop (see Chapter 2), and on the decoherence, which I will discuss shortly.

The employed geometric inductive coupling is a fixed type of coupling, and only works for qubits that are placed close together. A tunable coupling adds complexity to the circuit, and possibly to the operation, but also has several

advantages. When the coupling is tunable to zero, it can reduce the complexity of the energy spectrum and eigenstates, which in practice could help to relax constraints on frequency multiplexing and individual driving. Furthermore, if a coupling type is used that is not purely transverse, it can reduce or remove the necessity of elaborate refocussing schemes to correct for the continuously evolving phases. Any scheme that requires refocussing is unlikely to be successful in systems containing a large number of qubits.

Refocussing can also be avoided by using only transverse coupling types. A number of operation methods are available for transversely coupled qubits. Parametric coupling could be used to implement two-qubit gates, however, this would require that the coupling is tunable. Alternatively, the qubits could be pulsed into resonance. If this is done non-adiabatically, it will provide a swap-gate. This is however less convenient if more than two qubits are coupled together, and the qubits that need to interact are not nearest-neighbour in frequency, meaning that one has to pass resonance with another qubit. A potential solution for this is given by the usage of tunable coupling, so that even if two qubits pass resonance, there will not be any interaction. The method based on selective darkening (Chapter 5) is based on resonant driving of each qubit and does not require shifting of the qubit level splittings. In that case, there would be no necessity for tunable coupling. However, independent driving channels for the individual qubits are required.

An individual control channel for each qubit is presumably unavoidable in any scalable qubit system, either for tuning the qubit properties, such as the level splitting, adiabatically, or for inducing transitions. The commonly used frequency-selectivity cannot be scaled to large systems. In practice, the usable bandwidth for qubit frequencies is always limited. Many qubits of different splitting in a fixed bandwidth will obviously result in small frequency differences between the qubits. This limits the minimum allowed gate-time for resonant driving if spurious excitation of other qubits is to be avoided. This directly translates to longer required coherence times or increased gate errors.

A final consideration is the use of direct coupling, which generally implies that only nearest-neighbour qubits can be coupled. Alternatively an additional coupling element can be used, or a collective mode, in order to achieve interaction between remote qubits by acting as a bus. A large range of the coupling is not strictly necessary for performing universal quantum computation, as all possible gates can be implemented by performing a sequence of one- and local two-qubit gates. However, the range of the coupling is relevant for the error threshold of the gates. A commonly used number for the gate-error-threshold is 10^{-4} for a system in which two-qubit gates can be employed between any two qubits in the system. For systems that use only nearest-neighbour coupling, the error threshold can be orders of magnitude smaller. This difference is explained by the large number of

gates that need to be performed on a nearest-neighbour coupled system to obtain a certain gate on remote qubits, compared to the smaller number of gates if the remote qubits would be coupled directly. The exact number will depend on the error-correction scheme used. Note that a system with all qubits connected to a single bus does not necessarily require less time steps for a certain algorithm than a system of nearest-neighbour coupled qubits. If the bus does not support multiplexing for parallel operations, then all two-qubit operations will have to be done sequentially. A chain of nearest-neighbour coupled qubits most likely facilitates parallel two-qubit operations. For this reason, as well as for the reason of reduced complexity, fixed direct coupling should not lightly be disregarded.

Although it is still too early to predict which approach will be the best for scalable coupling, I anticipate a few important ingredients. It will not be possible to rely solely on frequency-selectivity for addressing the individual qubits. There are two main alternatives: using a global driving field and tunable qubits, or using individual excitation lines. In both cases, individual control lines are expected to be necessary. A combination of these two solutions would be given by the usage of clusters of qubits with one excitation line per cluster. Another reason for choosing tunable qubits is to avoid needing large numbers of high frequency signal generators; making qubits sufficiently equal by fabrication is unlikely to be achieved with any foreseeable fabrication techniques. Even if the number of required signal frequencies scales only linear with the number of qubits, it is still too much for a practical solution. In the most extreme case, all qubits are operated with a global excitation pulse, and the effect of the pulse is turned on and off by the bias parameters of an individual qubit. This might also cause a come-back for gates based on non-adiabatic shifts if these are easier implemented than resonant driving gates.

If we limit the dimension to two-dimensional devices, which is most natural for standard lithography, then the multiple-qubit arrays will most likely be limited to (semi-) one-dimensional structures. The second dimension will accommodate all the control lines for the qubits and the detectors. This has a large impact on the error threshold and makes the use of a bus likely unavoidable. The bus could be formed by a large qubit, which is more compact than the currently popular coplanar waveguide harmonic oscillator, and is possibly more simple for coupling different buses together, for example when using qubit clusters. If all qubits are coupled to a single bus, tunable coupling to the bus can be used to avoid crosstalk between the qubits, thereby enhancing the maximum achievable gate speed.

9.2.2 Decoherence

In previous research, the best decoherence times of flux qubits were obtained using relatively small qubit structures. The reason for this is not entirely clear. A

larger loop potentially picks up more magnetic flux, but the coupling strength to the control circuitry was reduced accordingly, and there was no indication that the global magnetic field limited the coherence times. The widely encountered 1/f-flux noise, the origin of which is not yet fully established, might explain reduced dephasing times, but not low relaxation times, for which higher frequencies are relevant.

The most likely explanation is that larger qubits also have a larger *capacitive* coupling to other structures in the environment. This contribution has often been disregarded because of the usually extremely small capacitances of less than (1 fF), that have a large impedance even at typical qubit frequencies. However, if these capacitances provide a current path that runs through one or more junctions, even small levels of current noise can be sufficient to dominate the relaxation [8].

As mentioned in the previous section, I rely on large qubits to provide the desired coupling strengths. One of the motivations for avoiding the usage of kinetic inductance is to disrupt the high-frequency current path that runs from one detector, through the qubits, to the other detector. Unfortunately, the residual capacitive coupling was likely still too high. For inductive coupling, this unwanted capacitance cannot be avoided, or even reduced much further. However, there is a relatively simple solution. In the device design, the detectors cover the outer parts of the qubits, and the qubit junctions are situated in between the two detectors. This geometry places the qubit junctions in the path of the noisy current, which runs only through the part of the qubits that is in between the two detectors. Secondly, the junctions are placed relatively far apart, allowing for larger capacitances to the islands than strictly necessary. In an improved design the junctions need to be moved to the opposite side of the qubit, on the other side of the detector, so they are not in the path of the current noise. They should also be placed much closer together to reduce the capacitive coupling to islands in between the junctions.

A rather successful approach for increasing coherence used in other qubit types is to put the qubits into a coplanar waveguide resonator, which effectively shields a large part of the noise spectrum of the environment [1]. This is especially interesting for suppressing 1/f-type of noise from the circuitry, and has led to relaxation-limited dephasing times. The resonator can be used for driving, coupling and readout. Although this is very elegant and useful for small numbers of qubits, this approach is not scalable to large numbers of qubits. The advantage for the coherence that is obtained by the coplanar waveguide can also be obtained with the bifurcative readout method used in this thesis. This method is discussed further in the next section.

9.2.3 Readout

In this thesis I describe the implementation of two independent AC bifurcation detectors for coupled qubits (Chapters 7 and 8). The attractive properties of this type of readout are the high fidelity, the quantum non-demolition nature of the measurement, and the relatively high maximum repetition rate (> 100 kHz). A quantum non-demolition measurement type is not strictly necessary for quantum computation, but can prove a powerful tool for state-initialisation, error-correction, or other schemes that require intermediate measurements. Additionally, the non-demolition property makes it an excellent tool for studying the process of measurement itself. The main drawback of the bifurcative detection scheme is the high complexity of both the circuitry and the operation. The alternative DC-switching readout is much simpler to implement and is, therefore, more attractive from a scalability point of view.

Previous experiments on a single-qubit device have achieved a measurement fidelity of 87%. In the two-qubit experiments, the maximum fidelity achieved was 50%, which is lower than the 90% that was estimated from detector sensitivity measurements. From the very low crosstalk it is concluded that the reduced performance of the two-qubit device was caused by relaxation of the qubits, and not related to the double readout. A possibly related issue of the bifurcative readout is the enhanced relaxation rate when the resonator switches to the high amplitude oscillatory state. This issue can be resolved by choosing the qubit bias such that the high-amplitude measurement outcome corresponds to the ground state of the qubit. A better understanding of the processes that cause the relaxation could help to improve the relaxation time during readout.

As the detectors are operated with AC pulses, the detectors themselves can be coupled capacitively to the external circuitry. This DC-decoupling can significantly improve the coherence of the qubits because of the suppression of the low frequency noise from the external circuit. This alternative has not been tested yet, but is highly recommended for future research.

An interesting alternative for low back-action readout is the conventional DC-switching with ultra fast switching pulses, combined with the usage of a maximum voltage bias below the pair-breaking voltage, such that no quasiparticles can be generated. In the optimal case, only a few revolutions of the superconducting phase are made before the detector returns to the zero-voltage state. This method is currently investigated. If it proves successful, it could decrease the complexity of the readout significantly.

9.3 Future directions

Future research on superconducting quantum circuits is expected to split in at least three main directions: (i) quantum information processing and communication, (ii) quantum physics, and (iii) ultra sensitive detection. Obviously these directions are not completely separable. The research on quantum computation will focus on scalability and improved gates and detection schemes. Even without new fundamental insights, it is possible that a quantum computer will be built. However, new theoretical and experimental insights can significantly increase the chances of success. The suggested directions for scalable quantum computation have already been discussed in the previous section. Typical experiments that will be on the roadmap are implementing the Shor-algorithm and error-correction schemes.

The possible applications of superconducting quantum circuits in physics research are much broader. Experiments have already been performed that were not possible in equivalent, yet more established quantum systems. Prominent examples are the circuit quantum electrodynamics experiments, which have accessed regimes of coupling strengths not yet achieved by equivalent atom-cavity systems.

The strong coupling to external parameters can also be used for sensitive detection. In this context, the superconducting qubits would just be used as supporting tools in other experiments. This is very similar to the history of the SQUID, which at first was mostly a study object by itself, but is now widely used as a detector or signal amplifier.

The most advantageous property of superconducting qubits is the flexibility to design the coupling strength from very weak to ultra strong. There already exist many proposals for coupling superconducting circuits to other systems, such as trapped atoms, nitrogen vacancies in diamond, Bose-Einstein condensates, or mechanical resonators, and it is likely that more will follow. One interesting application for such a hybrid system is the transfer of the quantum state of a superconducting qubit to the state of an optical photon.

The process of measurement is one of the most intriguing parts of quantum mechanics. The flexibility in designing the coupling strength between qubit and detector in superconducting circuits is very advantageous for studying the measurement process. For this type of research, the AC bifurcative readout is very attractive, as it provides high fidelity, low back-action, low crosstalk, and the possibility of varying the interaction strength in-situ. In the non-bifurcated regime, this detector can also be used for continuous measurement. These properties make superconducting circuits a suitable system for studying the measurement process, and implement quantum error-correction and quantum feedback, which I consider promising research directions for the near future.

9.4 Conclusion

Over the last few years, the field of superconducting qubits has evolved into a new phase, in which the experimental efforts focus on the integration of qubits into larger circuits. Many exciting experiments have been performed, and it is clear that there are many more to come.

The improved understanding of decoherence processes has led to longer coherence times of the qubits. However, for the realisation of a universal quantum computer, there is still a long way to go. The gap between the error threshold of the most advanced error correction schemes and the gate fidelities due to the limited coherence times is still a few orders of magnitude. Given enough time and effort, this gap can someday be closed, but will likely require advancements on both the coherence times as well as the error correction schemes.

Nevertheless, a useful quantum computer does not need to be universal. For example, the use of quantum circuits for the simulation of other quantum systems can provide new fundamental physical insights. However, no matter what we plan to measure or which results we expect, it's the anticipation of potential surprises that makes the journey exciting.

Bibliography

[1] J. Koch, T. M. Yu, J. Gambetta, A. A. Houck, D. I. Schuster, J. Majer, A. Blais, M. H. Devoret, S. M. Girvin, and R. J. Schoelkopf, Charge-insensitive qubit design derived from the Cooper pair box, Phys. Rev. A **76**, 042319 (2007).

[2] V. E. Manucharyan, J. Koch, L. I. Glazman, and M. H. Devoret, Fluxonium: Single Cooper-Pair Circuit Free of Charge Offsets, Science **326**, 113–116 (2009).

[3] A. O. Niskanen, Y. Nakamura, and J.-S. Tsai, Tunable coupling scheme for flux qubits at the optimal point, Phys. Rev. B **73**, 094506 (2006).

[4] J. Majer, J. M. Chow, J. M. Gambetta, J. Koch, B. R. Johnson, J. A. Schreier, L. Frunzio, D. I. Schuster, A. A. Houck, A. Wallraff, A. Blais, M. H. Devoret, S. M. Girvin, and R. J. Schoelkopf, Coupling superconducting qubits via a cavity bus, Nature **449**, 443–447 (2007).

[5] M. A. Sillanpää, J. I. Park, and W. Simmonds, Coherent quantum state storage and transfer between two phase qubits via a resonant cavity, Nature **449**, 438–442 (2007).

[6] L. DiCarlo, J. M. Chow, J. M. Gambetta, L. S. Bishop, B. R. Johnson, D. I. Schuster, J. Majer, A. Blais, L. Frunzio, S. M. Girvin, and R. J. Schoelkopf, Demonstration of two-qubit algorithms with a superconducting quantum processor, Nature **460**, 240–244 (2009).

[7] M. Ansmann, H. Wang, R. C. Bialczak, M. Hofheinz, E. Lucero, M. Neeley, A. D. O'Connell, D. Sank, M. Weides, J. Wenner, A. N. Cleland, and J. M. Martinis, Violation of Bell's inequality in Josephson phase qubits, Nature **461**, 504–506 (2009).

[8] M. Steffen, F. Brito, D. DiVincenzo, S. Kumar, and M. Ketchen, Decoherence of floating qubits due to capacitive coupling, New Journal of Physics **11**, 033030 (9pp) (2009).

Summary

This thesis presents experiments and theoretical work on coupled superconducting quantum bits, and a detection method for simultaneous readout of two coupled qubits with low crosstalk. The focus is on flux qubits with a direct inductive coupling. Experiments are performed on a system of two coupled qubits, showing its energy spectrum in high detail. Two types of entangling gates are experimentally demonstrated, one that can be operated outside the flux degeneracy point, and a new method that allows operation at the degeneracy point, where coherence is optimal. Additionally, the decoherence properties of a two-qubit system are investigated. The employed detection method is based on the measurement of the non-linear Josephson inductance of a DC-SQUID, operated in the bifurcation regime. The detection method is extended to a system of two detectors, with partial multiplexing of the signals. Experiments are performed to analyse the crosstalk between the detectors, and very low crosstalk is demonstrated.

Following the general introduction in Chapter 1, Chapters 2 and 3 provide the introduction to single and coupled qubit systems. The basic properties are mathematically derived, control methods are discussed, as well as a framework for analysing the loss of quantum information, i.e. decoherence. The energy level structure of a system of two coupled qubits is probed by spectroscopy measurements. Inducing thermal population by heating the sample yields additional transitions between higher levels, and all transitions are accurately modeled with a simple coupled-qubit Hamiltonian. Finally the requirements for performing a sequence of coherent quantum operations in a two-qubit system are discussed.

Chapter 4 presents an experimental demonstration of controlled-NOT quantum gates on a system of two coupled qubits. The method provides 4 complementary controlled-NOT gates: both qubits can act as target or control qubit, and both the 0- and 1-state can be used as the gate condition. The fidelity of the gate is determined to be $F = 0.4$. By employing a quantum interference protocol, also the induced phase of the gate is acquired, and demonstrates the anticipated 4π periodicity.

In Chapter 5 a new method is presented for implementing entangling gates, allowing selective driving of one individual transitions from a pair of frequency degenerate transitions. This method can be used with flux qubits biased in the degeneracy point, where the coupling is transverse, and any other qubit type with transverse coupling. The method is based on selectively suppressing, or darkening one transition out of a degenerate pair. It requires driving both qubits simultaneously with the same frequency, and specified relative amplitude and phase. The method is experimentally demonstrated on a pair of coupled flux qubits.

Chapter 6 describes the aspects of decoherence in a multi-qubit system that do not exist in a single-qubit system. When a single source of decoherence couples to multiple qubits, the noise in these qubits is correlated. Two experiments are proposed that exploit the characteristic features in the decoherence to obtain information of the source of decoherence. Additionally, experiments are presented that show relaxation of a two-qubit system through one of its intermediate states.

Chapters 7 and 8 present the results on implementing two ac-operated bifurcation flux detectors for the readout of two coupled qubits. The circuit design and readout method are discussed for a single detector, as well as the scheme for operating two detectors simultaneously. The direct detector-detector crosstalk, which is governed by an involved non-linear dynamical process, is analysed experimentally, and is shown to be less than 0.4 %.

Finally, in Chapter 9, the current status of the experiments is discussed, and suggestions for improvements and future research are made.

The results in this thesis show that flux qubits have very good prospects for performing multi-qubit experiments and can be used in simple quantum registers. The new method for creating entangling gates significantly enhances the operation coherence conditions, and thus the prospects for performing simple quantum algorithms with flux qubits. The low crosstalk of the bifurcation readout method, together with the previously demonstrated low back-action and quantum non-demolition properties, make this system an excellent candidate to further study the process of quantum measurement.

Pieter de Groot
Delft, July 2010

Samenvatting

Dit proefschrift presenteert experimenten en theoretisch werk op het gebied van gekoppelde supergeleidende quantum bits en een methode om twee gekoppelde qubits gelijktijdig uit te lezen met weinig overspraak. In dit onderzoek staan flux qubits met een directe inductieve koppeling centraal. De experimenten zijn uitgevoerd met een systeem van twee gekoppelde qubits waarbij het energiespectrum zeer gedetailleerd is waargenomen. Twee typen verstrengelende poorten zijn experimenteel gedemonstreerd; de een kan worden gebruikt buiten het flux degeneratie punt, en een nieuwe methode die gebruikt kan worden in het flux degeneratiepunt, waar de coherentie optimaal is. Tevens zijn de decoherentie eigenschappen van een twee-qubit systeem onderzocht. De gebruikte detectiemethode is gebaseerd op de meting van de niet-lineaire Josephson inductie van een DC-SQUID, gebruikt in het bifurcatie regime. De detectiemethode is uitgebreid tot een systeem van twee detectoren met gedeeltelijk multiplexen van de signalen. Experimenten zijn uitgevoerd om de overspraak tussen de detectoren te analyseren, en er is vastgesteld dat de waarde van de overspraak zeer laag is.

Na een algemene inleiding in hoofdstuk 1, worden in hoofdstuk 2 en 3 enkele- en gekoppelde qubit systemen geïntroduceerd. De basiseigenschappen worden wiskundig afgeleid en de operatiemethoden worden besproken samen met een methode om het verlies van quantuminformatie, oftewel decoherentie, te analyseren. De structuur van de energieniveaus van twee gekoppelde qubits is bepaald middels spectroscopische metingen. Het genereren van thermische bezetting door middel van het verwarmen van het sample levert aanvullende overgangen tussen hoger gelegen energieniveaus op, en alle transities zijn nauwkeurig gemodelleerd met een eenvoudige gekoppelde qubit Hamiltoniaan. Tenslotte worden de voorwaarden voor het uitvoeren van een reeks van coherente quantumoperaties in een twee-qubit systeem besproken.

Hoofdstuk 4 presenteert een experimentele demonstratie van controlled-NOT quantumpoorten in een systeem van twee gekoppelde qubits. De methode levert vier aanvullende controlled-NOT poorten: beide qubits kunnen dienen als doel of als controle qubit, en zowel de 0- als de 1-status kan worden gebruikt als de

poortconditie. De zuiverheid van de poort is vastgesteld op $F = 0.4$. Door gebruik van een quantum interferentie protocol is ook de geïnduceerde fase van de poort verkregen, die de geanticipeerde 4π periodiciteit vertoond.

In hoofdstuk 5 is een nieuwe methode geïntroduceerd voor het implementeren van verstrengelende poorten, die selectieve aandrijving mogelijk maakt van een enkele transitie in een ontaard paar. Deze methode kan gebruikt worden bij flux qubits die zijn ingesteld in het degeneratiepunt, waar de koppeling transversaal is, en ieder ander type qubit met transversale koppeling. De methode is gebaseerd op selectieve suppressie of verdonkering van één transitie van een ontaard paar. Het vereist gelijktijdige aandrijving van beide qubits met dezelfde frequentie met een gespecificeerde relatieve amplitude en fase. De methode wordt experimenteel gedemonstreerd in een paar gekoppelde flux qubits.

Hoofdstuk 6 beschrijft de aspecten van decoherentie in een multi-qubit systeem die niet bestaan in een enkel-qubit systeem. Wanneer een enkele bron van decoherentie gekoppeld wordt aan meerdere qubits dan is de ruis in deze qubits gecorreleerd. Twee experimenten zijn voorgesteld om de karakterestieke decoherentiekenmerken te benutten om informatie te verschaffen over de decoherentiebron. Tevens worden experimenten gepresenteerd die relaxatie van een twee-qubit systeem laten zien via een van de tussengelegen energietoestanden.

Hoofdstuk 7 en 8 presenteren de resultaten van het implementeren van twee ac-geopereerde bifurcatie fluxdetectoren voor het uitlezen van twee gekoppelde qubits. Het ontwerp van de elektronische circuits en de uitleesmethode worden besproken voor zowel een enkele detector, als het schema voor het gelijktijdig gebruik van twee detectoren. De directe detector-detector overspraak, hetgeen bepaald wordt door een complex niet lineair dynamisch proces, is experimenteel geanalyseerd, en er is aangetoond dat de overspraak minder is dan 0.4 %.

Tot slot, in hoofdstuk 9, wordt de huidige status van de experimenten bediscussieerd, en worden suggesties voor verbeteringen en toekomstig onderzoek gegeven.

De resultaten in dit proefschrift laten zien dat flux qubits zeer goede vooruitzichten hebben met betrekking tot het uitvoeren van multi-qubit experimenten en gebruikt kunnen worden in eenvoudige quantum registers. De nieuwe methode voor het creëren van verstrengelende poorten verhoogt de coherentieconditie significant, en hiermee de vooruitzichten voor het uitvoeren van eenvoudige quantum algoritmes met flux qubits. De lage overspraak van de bifurcatie uitleesmethode, samen met de eerder aangetoonde lage terugslag en quantum niet-distructieve eigenschappen, maken dit systeem een uitstekende kandidaat voor verder onderzoek naar het proces van quantum metingen.

Pieter de Groot
Delft, juli 2010

Curriculum Vitae

Pieter Cristiaan de Groot

Feb. 11, 1981	Born in Marken, The Netherlands.
1994 - 1999	Secondary school, Damstede, Amsterdam.
1999 - 2005	M. Sc. Applied Physics (*cum laude*), Delft University of Technology, Graduation research in the Quantum Transport group under supervision of prof. dr. ir. J.E. Mooij and dr. C.J.P.M. Harmans.
2005	Internship at the Eidgenössische Technische Hochschule Zürich (ETH), research in the Quantum Photonics group of prof. dr. A. Imamoglu.
2005 - 2010	Ph. D. research at Delft University of Technology, in the Quantum Transport group under supervision of prof. dr. ir. J.E. Mooij and dr. C.J.P.M. Harmans. Subject: Coupled flux qubits and double bifurcation readout.

List of publications

1. *Demonstration of controlled-NOT quantum gates on a pair of superconducting quantum bits*
   J.H. Plantenberg, P.C. de Groot, C.J.P.M. Harmans & J.E. Mooij,
   Nature **447**, 836-839 (2007).
2. *Quantum non-demolition measurement of a superconducting two-level system*
   A. Lupaşcu, S. Saito, T. Picot, P.C. de Groot, C.J.P.M. Harmans & J.E. Mooij,
   Nature Physics **3**, 119-125 (2007)
3. *Quantum non-demolition measurement of a superconducting qubit*
   A. Lupaşcu, S. Saito, T. Picot, P.C. de Groot, C.J.P.M. Harmans & J.E. Mooij,
   AIP Conference Proceedings, **1074**, 26-31 (2008)
4. *Interqubit coupling mediated by a high-excitation-energy quantum object*
   S. Ashhab, A.O. Niskanen, K. Harrabi, Y. Nakamura, T. Picot, P.C. de Groot, C.J.P.M. Harmans, J.E. Mooij & F. Nori,
   Physical Review B **77**, 014510 (2008)
5. *Low-crosstalk bifurcation detectors for coupled flux qubits*
   P.C. de Groot, A.F. van Loo, J. Lisenfeld, R.N. Schouten, A. Lupaşcu, C.J.P.M. Harmans & J.E. Mooij,
   Applied Physics Letters **96**, 123508 (2010)
6. *Selective darkening of degenerate transitions demonstrated with two superconducting quantum bits*
   P.C. de Groot, J. Lisenfeld, R.N. Schouten, S. Ashhab, A. Lupaşcu, C.J.P.M. Harmans & J.E. Mooij,
   Accepted for publication in Nature Physics